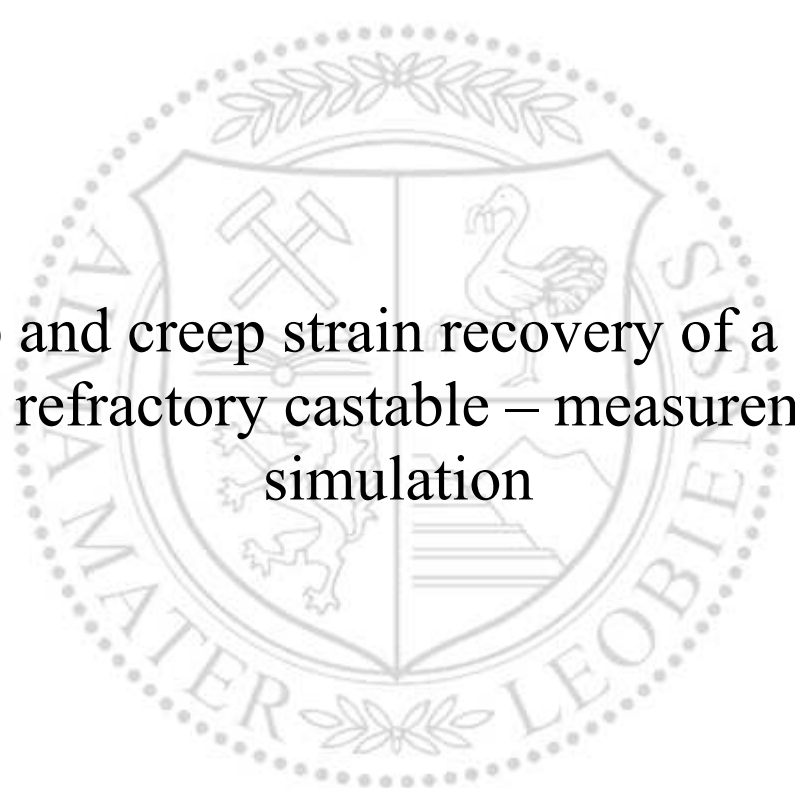Chair of Ceramics

Doctoral Thesis

Creep and creep strain recovery of a spinel forming refractory castable – measurement and simulation

Dipl.-Ing. Behnam Akbari

December 2023

AFFIDAVIT

I declare on oath that I wrote this thesis independently, did not use other than the specified sources and aids, and did not otherwise use any unauthorized aids.

I declare that I have read, understood, and complied with the guidelines of the senate of the Montanuniversität Leoben for "Good Scientific Practice".

Furthermore, I declare that the electronic and printed version of the submitted thesis are identical, both, formally and with regard to content.

Date 20.12.2023

Signature Author
Behnam Akbari

To my beloved Father and Mother

ACKNOWLEDGEMENT

I would like to begin by expressing my deep appreciation to my supervisor, **Priv.-Doz. Dr. Dietmar Gruber**, for his professional guidance and all of his valuable insights, constructive suggestions, useful critiques, and constant support during this research. His unwavering dedication and commitment to teaching and research have been truly inspiring, and I feel privileged to have had the opportunity to work with him.

Further thanks to **Prof. Dr. Harald Harmuth** and **Priv.-Doz. Dr. Shengli Jin** for their assistance during this research with their useful recommendations on this project.

Special thanks to Voestalpine-Linz and RHI-Magnesita as the company partners of this project for preparing the experimental materials. Besides, I would also like to thank my colleagues Dr. Christina Atzenhofer, Dr. Stefan Schachner, and Mr. Alexander Halacek at the Chair of Ceramics for their help in the experimental parts of this project.

Any attempt at any level can't be satisfactorily completed without the support and guidance of my family: Mom, Dad, and my sister. I would like to give my grateful thanks to them for supporting me in this journey and every step of my life.

ABSTRACT

Spinel forming (SF) and Pre-formed spinel (PS) castables are common materials in refractory linings of steel ladles in secondary steel metallurgy. In service, these materials are affected by thermo-mechanical stresses. At elevated temperatures, this leads to creep of the castables. For the optimum design of the lining, consideration of the creep behaviour is important. In the current study, the castables were characterized in dried and sintered state and compared in bulk and true density, apparent and true porosity, Young's modulus up to 1500 °C and uniaxial compressive creep behaviour. The microstructure of both castables was investigated using SEM, additionally, mineralogical phases were analysed with XRD. For further investigation, only the SF castable was selected. During the sintering process, the SF castable showed volume expansion and formation of liquid phases. The liquid phase partially counterbalanced the volume expansion caused by the in-situ spinel formation. However, it was observed that the liquid phase formation decreases the castables Young's modulus at high temperatures and reduces the creep resistance. Uniaxial compressive creep tests were performed at 1300, 1400, and 1500 °C for three loads per temperature. The separation of creep stages was performed with an in-house developed MATLAB code and the three-stage creep parameters were inversely evaluated using the Norton-Baily creep equation. Additionally, a statistical study was carried out to evaluate the creep parameters by different combinations of measurements. Furthermore, the material's creep behaviour was investigated under loading/unloading (l/u) conditions. For this purpose, the experiments have been performed at 1300 °C under different loads. After defined periods, the load was reduced. In this way, several cycles were performed. It was observed that creep strain recovery occurs after load reduction. The recovery increases with holding time and the degree of unloading. It was identified that the internal stress (back-stress) was the driving force for the creep strain recovery. Finally, a non-linear kinematic hardening model (Chaboche) was applied to simulate the creep strain recovery behaviour. The model fits the experimentally observed creep strain for different creep periods and unloading degrees with one parameter series. However, further work is necessary to automatize the parameter determination.

CONTENT

1 PROBLEM DEFINITION

In service, refractory ceramics are experiencing thermomechanical stresses due to thermal expansion and temperature gradients. The stresses cause creep and fracture; this is well known and was investigated for many materials with fracture tests and creep tests at constant loads. However, the loads are not constant in service because of the batch-wise operations. What is missing is the knowledge of how changing loads influence the creep behaviour and if a significant amount of creep strain recovery can be observed for refractories. Therefore, the current work focuses on a) creep characterization under changing loads, b) quantification of creep recovery after load reduction and c) identification of parameters for a material model capable of FE-simulation of the creep and recovery behaviour in service.

2   STATE OF THE ART

2.1   Refractory materials, castables

Refractories are ceramic materials characterized by their high melting points, surpassing 1200 °C, and their inherent properties enabling them to serve as effective heat-resistant barriers, segregating high-temperature regions from low-temperature areas in industrial linings. Typically, refractories are composed of thermally stable mineral aggregates, a binder phase, as well as porous, and heterogeneous additives. The essential prerequisites for refractories entail: (i) the capacity to endure elevated temperatures; (ii) resilience against erosive and corrosive actions of liquid metal, hot gases, and liquid slag; (iii) the ability to withstand operational loads; (iv) resistance to material contamination from external sources; (v) preservation of dimensional stability under high-temperature conditions and during repeated thermal cycling; and (vi) proficiency in heat retention [1]. Refractories may be divided into categories based on their shaping: unshaped refractory products and shaped refractories. Castables, mortars, ramming mixes and other unshaped refractories are a mixture of different aggregates, matrix components, binders and additives and in most cases, they are shaped at the service location. Shaped refractories, such as bricks, shrouds and nozzles, are shaped by casting or moulding, and heat treated afterwards [2].

2.2   Preformed spinel (PS) and spinel forming (SF) castables

The composition of castables varies to achieve favourable physical and chemical properties for the application. Since the 1990s, preformed spinel (PS) and spinel forming (SF) high alumina castables have become very common for the lining of steel ladles [3,4]. Spinels form a large mineral group with the general formula AB_2X_4, where A stands for divalent and B for trivalent cations. Spinels crystallize in the cubic crystal system. The most common spinels in refractories contain aluminium, magnesium, iron and chromium ($MgAl_2O_4$, $MgCr_2O_4$, $FeAl_2O_4$, $MgFe_2O_4$) [5]. For the current research, the term spinel represents $MgAl_2O_4$. PS and SF castables contain spinel in their structure to raise the corrosion and slag penetration resistance [5]. For the PS castable, spinel aggregates are added to the mix of the castable and in the SF type, spinel is formed due to the reaction of Al_2O_3 with MgO at temperatures above 1100 °C. For refractory castables, calcium aluminate cement is mostly used as a binder [5,6]. Preformed spinel with a minimum grain size of 45 μm, was added to the high alumina containing mix [6]. As a result, there is a significant enhancement in the slag corrosion resistance and the thermo-mechanical properties like hot modulus of rupture (HMoR) and refractoriness under load (RUL) of the castable at service temperature [6,7]. The amount of the spinel added to the castables typically varies between 20-25 wt% [6]. According to the results by Nagi and co-workers, this amount of added spinel leads to the lowest corrosion and slag penetration rate [7]. Many investigations on the microstructure, the effect of PS and SF as well as the effect of impurities on the physical properties of both types of castables have been carried out. Braulio et al. [6] mentioned that pre-formed spinel is added to high alumina castable to improve mechanical properties at elevated temperatures. Kriechbaum et al. [8] observed that HMoR at 1500 °C increased from 8 to 17 MPa when fine spinel was induced to the tabular high alumina low cement castable. PS castables are known for volumetric stability compared to SF castables. Generally, during the heating process, CaO reacts with

available alumina to form CA_2 and, later, CA_6 at temperatures above 1000 °C and 1400 °C, respectively [5,6]. Formation of both phases may lead to volume expansion in the castables. However, the volume expansion related to the CA_2 formation for PS castable was not detected from the results determined by Sako et al. [9], due to the type of alumina (tabular alumina) used in the microstructure. Tabular alumina shows lower thermal reactivity than reactive alumina. Therefore, as tabular alumina was the only source for forming the CA_2, no residual expansion was observed associated with the CA_2 phase. The expansion rate test indicated that only one peak was detected above 1400 °C because of CA_6 formation in the PS castable containing tabular alumina [9]. Besides, the sintering profile could impact the expansion caused by the CA_6 formation. In another study [10], they noted that during the sintering of a PS castable, no calcium dialuminate (CA_2) remained and CA_6 was found beside corundum and spinel. Several authors indicated that the formation of the CA_6 and especially its location in the matrix of PS castable enhances its hot strength [6,8-11].

Spinel powders are synthesised using different techniques. The most straightforward way is conventional oxide mixing. Fine MgO reacts with Al_2O_3 fines in the matrix of the castable at service temperatures in the steel ladle [12]. Dead-burnt magnesia and calcined or reactive alumina are common constituents in the structure of the SF castable [4,5]. SF castables are bonded by calcium aluminate cement (CAC), which causes fast curing and high green mechanical strength [13]. Several publications [14,15] indicated that the temperature for the formation of the spinel in the matrix of the SF castable is above ~1100 °C and by increasing the temperature (1200-1400 °C) the rate of spinel formation increases as well. The spinel formation improves the corrosion and thermal-shock resistance of such castables [5, 6]. However, there is a significant disadvantage of spinel formation. During the sintering process, this newly formed phase will cause volume expansion. Theoretically, the volume expansion could be 13% however, 5-7% expansion was recorded for different chemical compositions [3]. Braulio et al. [6,16,17] mentioned that SF castables represent a volume expansion (8%) attributed to the density differences between the aggregates (MgO: 3.58 g/cm^3, Al_2O_3: 3.98 g/cm^3, and $MgAl_2O_4$: 3.60 g/cm^3) and it is mainly associated by the formation of spinel at a temperature close to 1200 °C. Taking into account that these kinds of castables are bonded by CAC then two other expansive reactions such as the formation of calcium dialuminate (CA_2) and calcium hexaluminate (CA_6) must be considered. The first one ($CA+A=CA_2$) is formed at a temperature of 1000 °C with a theoretical volume expansion of +13.6%, and the second one will be formed based on the reaction $CA_2+4A=CA_6$ at 1450 °C with +3.01% of volumetric change if the amount of the alumina is sufficient. Therefore, the overall volume expansion of SF castables is caused not only by spinel formation but also by the CA_2 and CA_6 formation. However, the major volume expansion of the SF castable is attributed to the in-situ spinel formation. The expansion during the spinel formation depends on the alumina precursor phase and is attributed to the density differences between MgO and Al_2O_3 and spinel. Nevertheless, in other investigations [18-20] this expansion was analysed by the derivative of the expansion, it was found that for microsilica free compositions, the CA_2 formation occurs at 1000 °C however, it is proved that adding fumed silica in the range of 0.5-1 wt% can significantly decrease the amount of this phase and increase the workability of the SF castable [6]. Besides, microsilica reduces the MgO hydration rate and enhances the followability of SF castables [6]. On the other hand, microsilica forms liquid phases below the sintering temperature and helps to counterbalance the volume expansion caused by mentioned phases [18]. Different authors [9,10,

21,22] proved that the main role of the microsilica for the SF castable is to reduce the material expansion during the sintering process by softening. This can happen by the generation of low temperature melting phases such as gehlenite ($Ca_2Al_2SiO_7$) and anorthite ($CaAl_2SiO_8$). Therefore, the expansion depends on the content of the liquid phase, which is directly associated with the amount of microsilica added to the mix. Tawara et al. [23] mentioned that a high MgO/SiO_2 ratio (>12%) in the mix of an SF castable is resulting in a significant permanent linear expansion (>2%) and leading to intensive cracking of the material. It was observed that a low MgO/SiO_2 ratio (<3%) is not preferable due to high shrinkage and cracking generation. A 4 to 8% MgO/SiO_2 ratio was suggested to reduce the expansion and the crack formation. The formed liquid phases affect the shrinkage of the SF castable and speed up the formation of the spinel [24,25]. However, the formed liquid can deteriorate the material properties such as hot modulus of rupture (HMoR), corrosion resistance and creep resistance [26,27]. Investigations proved that for 0.75 wt% microsilica content, a higher decrease of HMoR was detected in comparison to microsilica free castable for temperatures from 1000 to 1400 °C. However, this behaviour might be a positive aspect for some applications [26,27].

2.3 Creep

Per definition, creep is a deformation over time due to a constant load below the yield strength and is more significant with increasing temperatures [28]. Creep is usually investigated at homologous temperatures above 0.3 ($T/T_m > 0.3$, T_m: melting temperature) [29]. A typical creep curve is schematically represented in Fig. 1.
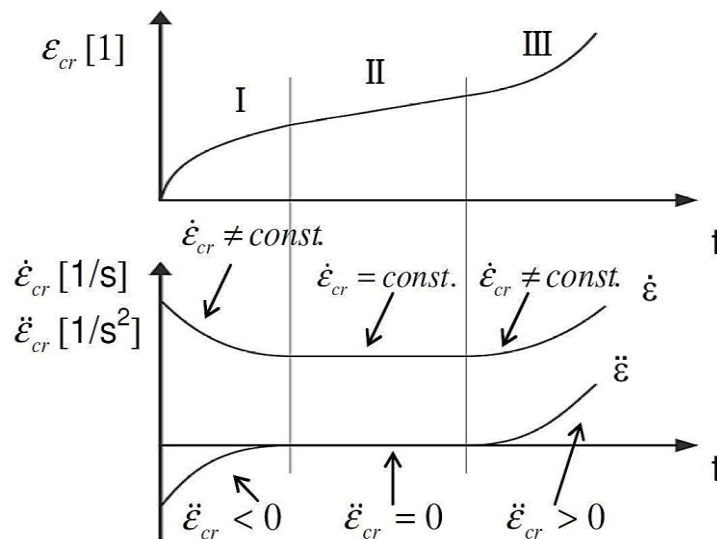

Fig. 1: Theoretical creep strain curve with first and second derivatives.

A complete creep curve can be separated into three stages. The slope of this curve gives the creep strain rate and varies over time into three stages (primary, secondary, and tertiary) [30]. The primary stage shows a decrease in creep rate with an increase in the creep strain over time. Hardening is taking place and due to this reason, the creep rate decreases [30]. The secondary stage is known as steady-state creep and shows a constant creep rate with increasing creep

strain. In the last region, creep strain increases with increasing creep rate until the final fracture occurs [30].

2.3.1 Mechanism of creep in ceramics

The creep of refractory ceramics is affected by chemical composition, mineralogical composition, firing, temperature, and stress [31]. Several basic mechanisms can contribute to creep in ceramics. Creep mechanisms may be determined from the exponents in creep equations for steady-state creep (Eq.1) [32]:

$$\dot{\varepsilon}_{cr} = \frac{ADGb}{kT} \left(\frac{b}{a}\right)^p \left(\frac{\sigma}{G}\right)^n \tag{1}$$

Where D is the appropriate diffusion coefficient, A is a constant, G is the shear modulus, b is Burger's vector, k is Boltzmann's constant, T is the absolute temperature, d is the grain size, p is the exponent of the inverse grain size, n is the stress exponent. The diffusion coefficient is given by (Eq. 2):

$$D = D_0 \exp\left(-\frac{Q}{RT}\right) \tag{2}$$

Where D_0 is a constant, Q is the activation energy for the diffusion process and R is the gas constant (8.31 J mol^{-1}K^{-1}). To identify the creep mechanisms of ceramics, n and p together with the activation energy are used. Vacancy diffusion in the lattice and along the border causes creep and is proportional to the applied stress [33,34]. The grain size exponent p for the former process is 2, whereas it is 3 for the latter. A grain boundary sliding due to dislocation movement shows an exponent n of 2 and an exponent p of 1 [35,36]. The creep strain rate is independent of grain size and the exponent n is no less than 3 in creep dominated by dislocation glide and climb. The creep strain rate can be simplified as seen in Eq. 3, in which A is a constant [37]:

$$\dot{\varepsilon} = \frac{A}{RT} \sigma^n exp\left(-\frac{Q}{RT}\right) \tag{3}$$

Refractories usually contain one or more crystalline phases, microcracks, and perhaps a vitreous phase. For polydisperse multicomponent refractories, many mechanisms are acting concurrently. Out of this reason, it is difficult to determine the creep mechanisms acting. Nonetheless, the strain rate will be dominated by the acting mechanisms with the highest strain rates.

Typical creep mechanisms for refractories are as follows:

A) Dislocation creep:

Dislocation creep occurs because of the movements of dislocations in crystals. Dislocations move along the lattice plane denominated as the slip plane. The orientation of slip planes depends on the crystal structure. The occurrence of dislocation motions depends on the breakage of bonds between the atoms during the deformation [28]. As dislocations move and interact, they can generate new dislocations, form dislocation networks and contribute to the overall deformation.

Obstacles can reduce dislocation motion and creep deformation when a dislocation slip is impeded. These obstacles can be screw dislocations, the crystal structure itself, and grain boundaries. The rate of deformation and the diffusion of lattice vacancies are the primary factors influencing the slip process [37-39].

B) Diffusion creep:

Diffusion creep is associated with lattice mechanisms and due to the diffusion of atoms, the deformation occurs. Diffusional creep dominates over deformation mechanisms such as dislocation creep at high temperatures and low stresses. Grains elongate along the stress axis through the diffusion of atoms through a lattice. During the creep deformation, atoms exchange at the grain boundaries. It is confirmed that under tensile stress atoms tend to diffuse longitudinal from one side of the specimen to the other; this changes the dimensions of the specimen. Coble and Nabarro-Hering creep denominate diffusional creep mechanisms. Coble creep is driven by differences in grain boundary energy, rather than differences in chemical potential or concentration, as in Nabarro-Herring creep [28].

C) Grain boundary sliding (GBS):

In the GBS process, grains slide during the deformation along the common boundary [40]. GBS can be facilitated by diffusion and dislocation motion. Liquid or glassy phases can significantly affect the GBS. Liquid phases can reduce the resistance to GBS and facilitate the relative motion of adjacent grains. When the amount of the glassy phase and other low-melting-point phases is large, direct connections between grains are destroyed at high temperatures and under load [38-40]. In contrast, crystallisation of the liquid phase will increase the resistance to GBS [28,39].

2.3.2 Creep of high alumina refractories

Refractory materials are usually composed of one or more crystalline phases, possibly a glassy phase, and pores. The glassy phase is frequently a bonding phase, and its composition and properties influence the creep behaviour significantly [38,39]. Bakunov et al. [41] found out that in the creep of high alumina refractories the chemical composition and microstructure, as well as the manufacturing parameters, impact the creep resistance of these refractories. Many studies have shown that the amount of formed mullite in the matrix affects the creep of high alumina refractories [38,39,41]. Clements and Vyse [42], for example, tested the compressive creep of several commercial high alumina refractories at temperatures up to 1600 °C. They discovered that the formed continuous mullite network contributes to decrease refractory creep rates. Fused mullite, calcined kyanite, or sillimanite were found to have high creep resistance, however, bauxite and sintered aluminas were found to be less resistant. The firing temperature, sodium oxide impurity, and alumina grain reactivity play a role in mullite formation which, improves creep resistance [43,44].

Refractory castable creep is usually more complex than that of shaped refractories after the burning process. Phenomena like crystallization, phase development, sintering, and stress-aided sintering are observed during the first heat. Bray et al. [45,46] published research on alumina refractory castable with calcium aluminate (CA) cement (7.5 to 25 wt%) as a binder. It was

discovered that the creep of this refractory is primarily attributed to the deformation of the cement matrix and that increasing the cement quantity has no effect on the creep mechanism. In another investigation, the impact of thermal/strain history on refractory castable creep was studied [47]. It was shown that creep is highly dependent on thermal/strain history. During the initial application of stress or temperature and due to the combination of stress and temperature, the structure of refractory castable changes. For the initial heating up, the activation energy for creep is between 130-170 kJ/mole. However, after temperature treatment, the stress exponent increased to more than 2.5 and the activation energy was between 620 and 720 kJ/mole. Diaz and Torrecillas [48,49] conducted creep experiments on high alumina refractory castables with additions of dolomite, spinel, and periclase, to understand the effects of the route of spinel formation and content on high-temperature mechanical properties. It was observed that at 1100-1200 °C, the formation of CA_2 from the interaction of CA with alumina in the presence of an amorphous phase controls the creep of castables. At 1300 °C, as all CA phases were completely dissolved in the glassy phase, the castable exhibited the worst creep resistance in comparison to the castables with other additives such as dolomite and MgO [48].

2.4 Creep models

For a mathematical description of the creep behaviour, many models were developed. When a material is exposed to a uniaxial continuous load, its creep deformation is determined by stress (σ), time (t), and temperature (T) (Eq. 4). As a result, the general creep strain (ε_{cr}) equation may be written as follows [50]:

$$\varepsilon_{cr} = f\ (\sigma, t, T) \tag{4}$$

Functions of stress (σ), time (t), and temperature (T) are applied to approximate the creep strain [50-53] (Eq. 5):

$$\varepsilon_{cr} = f_1(\sigma)\ f_2(t)\ f_3(T) \tag{5}$$

To characterize the creep dependency on stress, time and temperature, a variety of functions were developed. Among them Norton equation is frequently utilized to determine the stress function during the secondary creep phase [54], and Bailey equation for the time function when the stress is constant [55], and Arrhenius's law to quantify the temperature dependence (Eq. 6-8) [56].

$$f_1(\sigma) = B_1 \sigma^n \tag{6}$$

$$f_2(t) = B_2\ t^m \tag{7}$$

$$f_3(T) = C\ exp(-\frac{Q}{RT}) \tag{8}$$

B_1, B_2, and C are material constants, Q is the activation energy for the diffusion process and R is the gas constant. Under isothermal circumstances, the above three equations combine to form Eq. 9, which is commonly referred as the Norton-Bailey creep equation [53]:

$$\varepsilon_{cr} = A \, \sigma^n \, t^m \tag{9}$$

In the case of a constant load, the creep strain rate can be determined by differentiating creep strain to time, which is referred as time hardening/softening representation [50,53].

$$\dot{\varepsilon}_{cr} = m \, A \, \sigma^n \, t^{m-1} \tag{10}$$

Strain hardening/softening representations may be generated by removing the time variable from Eq. 10, as shown by [50,53]:

$$\dot{\varepsilon}_{cr} = m \, A^{1/m} \, \sigma^{n/m} \, \varepsilon_{cr}^{m-1/m} \tag{11}$$

The creep strain rate equation for uniaxial stress states may still be applied in the case of multiaxial loading if the following conditions are met: the rate of volumetric creep strain is zero, therefore the material volume under creep is constant, and multiaxial creep is a shear-dominated process [52]. As a result, Eq. 11 is changed to Eq. 12:

$$\dot{\bar{\varepsilon}} = m \, A^{1/m} \, q^{n/m} \, \bar{\varepsilon}_{cr}^{m-1/m} \tag{12}$$

where $\dot{\bar{\varepsilon}}$ is the equivalent creep strain rate, $\bar{\varepsilon}_{cr}$ is equivalent creep strain, σ_1, σ_2, σ_3 are the minimum, middle and maximum principal stresses and q is the von Mises equivalent stress, as defined in Eq. 13:

$$q = \sqrt{\frac{1}{2} \left[(\sigma_1 - \sigma_2)^2 + (\sigma_2 - \sigma_3)^2 + (\sigma_1 - \sigma_3)^2 \right]} \tag{13}$$

2.5 Creep testing

Two standardized testing methodologies are applied to assess the creep behaviour of refractories. One method is known as creep-in-compression (CIC), which uses the same equipment as the refractoriness under load (RUL) testing approach, here, the heating rate is 5 °C/min and the maximum applied load is 0.2 MPa. Apart from specimen diameter, testing load, and heating rate, CIC standards in Europe, the United States, Japan, and China are similar [57]. During the heating-up and dwell phases, the present compressive stress of 0.2 MPa is applied to the specimen according to European standards EN 993/ISO 1893 [58]. The differential displacement of two corundum tubes is measured using linear variable differential transducers to determine the change in length of the specimen (LVDTs). CIC applies the load after the heating phase under constant temperature, unlike the RUL technique first loads the sample, then increases the temperature, and then measures the deformation during the entire heating process [59,60]. The primary purpose of the CIC and RUL techniques is to qualitatively compare the creep resistance of various materials and to assist users in selecting the most appropriate material for a particular application. Furthermore, since the CIC technique only investigates one load, it cannot be used to determine load-dependent creep [61,62]. Therefore, identifying creep parameters using the CIC measurement has many drawbacks. A further drawback is that the commencement of creep is unknown. Because the specimen is heated under load, creep will begin during the

heating-up phase before the start of the dwell time. Furthermore, the 0.2 MPa maximum load limit prevents the research of load values that are relevant to the actual application of refractories in many circumstances [63]. To solve the disadvantages of the RUL and CIC approaches, Jin et al. [64] developed an improved compressive creep testing equipment. Fig. 2 shows the schematic of this device for compressive creep testing. The machine is equipped with a tabular furnace and MoSi$_2$ heating elements inside the chamber. On cylindrical refractory specimens with a diameter of 35 mm and a height of 70 mm, loads of up to 20 KN can be applied. To measure the vertical displacement precisely on the specimen surface at the front and rear sides, two mechanical extensometers (the initial distance between two extensometer rods is 50 mm) are applied. To avoid a chemical reaction between the piston and specimen, corundum plates are placed on the top and bottom of the sample (Fig. 3). After inserting the sample into the respective creep device, it is exposed to a preload (0.05 MPa) for stabilization during the heating step. Next, the sample is heated with 10 °C/min to the testing temperature. After a 1 h dwell time in order to have a thermal steady state, the load is applied, and the creep test and displacement measurement starts. The test result is calculated from the mean values of the front and the rear extensometers. In the current research, the developed advanced spindle-driven compressive creep testing device was used for creep tests at elevated temperatures.
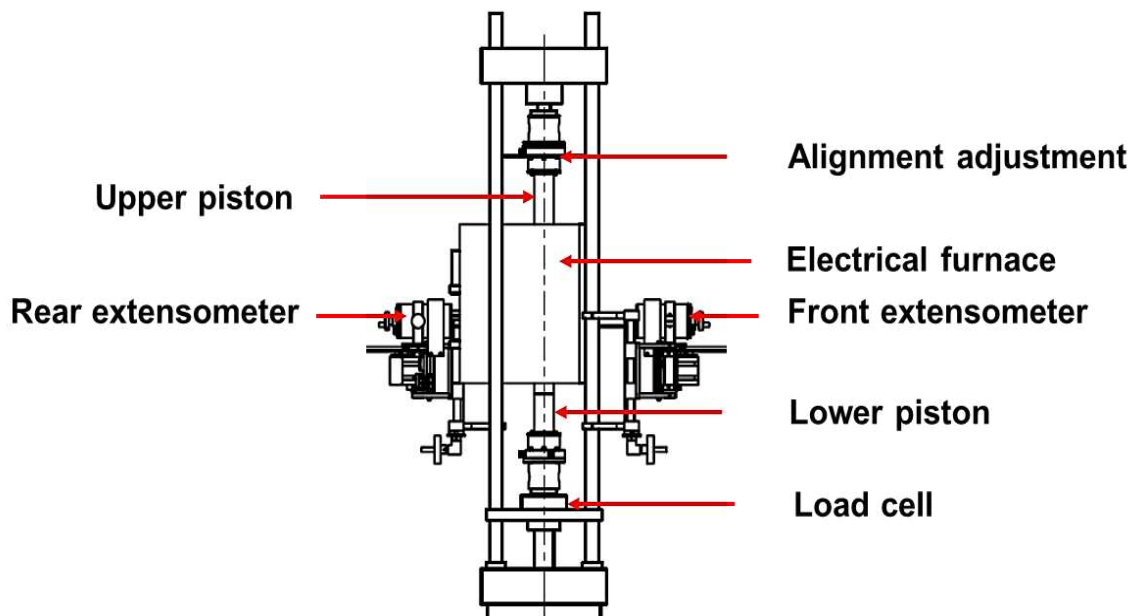
Fig. 2: Schematic design of the compressive creep testing machine [64].
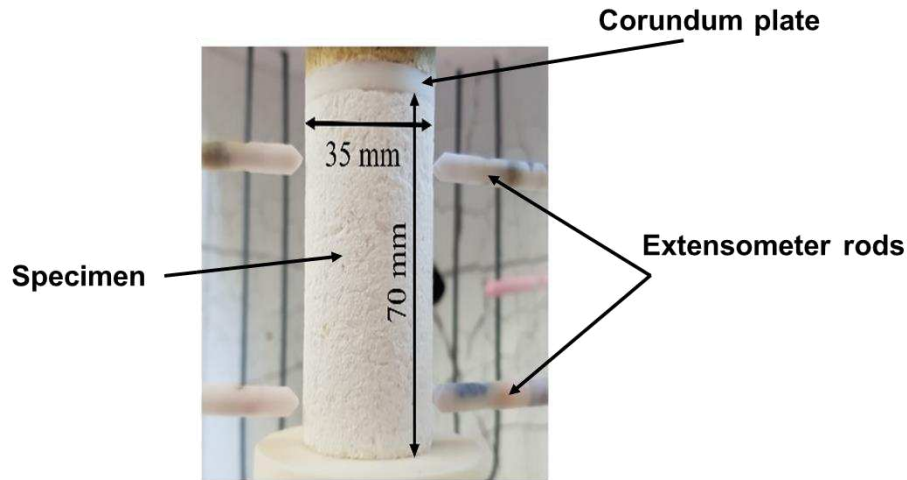
Fig. 3: Specimen inside the compressive creep testing furnace.

2.6 Methodology to determine the creep parameters

The Norton-Bailey creep equation is often applied for modelling the creep of refractories [63,65]. The model is used in time-hardening/softening and strain hardening/softening representations. Both representations predict the same outcomes when the stress is constant. On the other hand, the strain hardening representation has shown a good agreement with experimental creep curves with changing stresses [50,66]. According to the Norton-Bailey strain hardening/softening representations, the creep strain rate is a function of temperature, stress, and creep strain (Eq. 14):

$$\dot{\varepsilon}_{cr} = K(T) \; \sigma^n \; \varepsilon_{cr}^a \tag{14}$$

Here, K represents the temperature dependent constant, n is the stress exponent, and a is the strain exponent. Under the strain hardening condition (primary creep), the value of a is negative, while in the case of strain-softening, it is positive (tertiary creep). For secondary creep a=0.

Both elastic and creep deformation are included in the measured deformation. The total strain ε_{tot} is calculated from the laboratory compressive creep test results, considering the initial extensometer legs distance (50 mm), and the elastic strain σ/E is subtracted for the creep strain ε_{cr} (Eq. 15):

$$\varepsilon_{cr} = \varepsilon_{tot} - \frac{\sigma}{E} \tag{15}$$

The applied stress is denoted by σ, and Young's modulus is E, which may be determined using the IET (Impulse excitation method) measurement [67]. For inverse identification of Norton-Bailey creep law parameters, Eq. 14 was rearranged by separating ε_{cr} and t and then integrated. Numerical integration is used for non-predefined stress/time curves. The trapezoidal rule is then used for suitably short intervals between subsequent time steps t_{i+1} and t_i, yielding Eq. 16:

$$\varepsilon_{cr,i+1} \left[\varepsilon_{cr,i}^{1-a} + \frac{(1-a).K.(\sigma_{i+1}^{n}+ \sigma_{i}^{n}).(t_{i+1}-t_i)}{2} \right]^{\frac{1}{1-a}} \tag{16}$$

Using the Levenberg-Marquardt optimization algorithm in MATLAB [68], the creep parameters a, n, K in Eq. 16 are inversely determined for each creep stage. The sum of the squared difference between the experimental and calculated curves for the respective creep stage was minimized. Basically, for the inverse estimation procedure, at least two tests with different loads at the same temperature can be used to determine a parameter set. However, in this research, a statistical study has been carried out to determine the creep parameters [63-65,69]. The flow chart in Fig. 4 shows the creep parameters evaluation procedure.
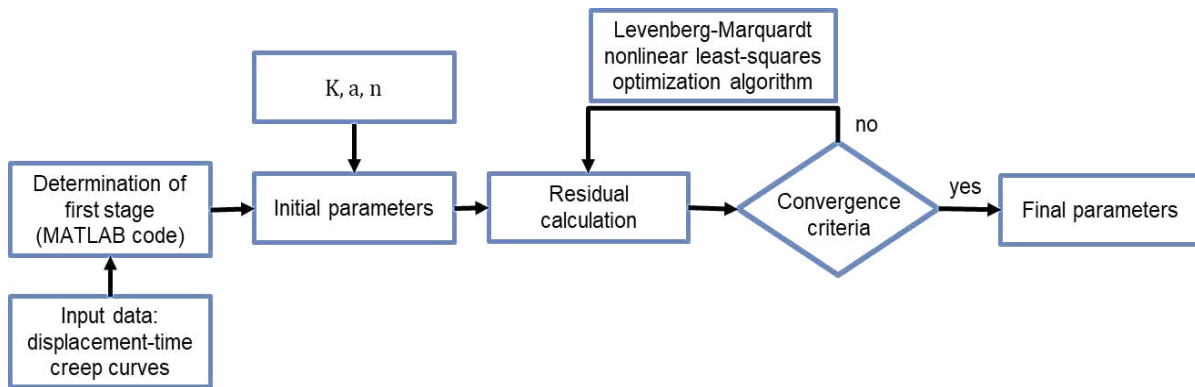
Fig. 4: Evaluation procedure to determine the Norton-Bailey creep parameters for each creep stage.

2.7 Separation of creep stages

The transition of the three creep stages must be determined in order to identify the Norton-Bailey creep parameters. The creep-strain rate in the second stage is theoretically constant, thus this stage may be determined appropriately. Nonetheless, the noise in the experimental data causes the creep-strain rate/time curve to fluctuate [70,71], making it difficult to use creep-strain rates for automated transition detection. Schachner et al. [70] presented a method for fully automated detection of creep-stage transitions for measured creep curves, which was implemented using a MATLAB code. The first step is to estimate the secondary creep stage's start and finish values. A fifth-order polynomial fit of the experimental creep curve is applied. When the third derivative is zero, two roots are obtained, which serve as preliminary start and end values for the secondary stage. More details can be seen in [71]. Using the Norton-Bailey method explained above, experimental creep curves are divided into three stages, and creep parameters for each stage are identified.

2.8 Creep strain recovery in ceramics

In most cases, creep testing of refractories is done under constant loads. In service, e.g., in the steel ladle in iron and steel making, the materials are exposed to loading/unloading (l/u) conditions due to preheating, charging and discharging the molten steel periodically. In such conditions, materials are initially subjected to a load and the creep deformation occurs and develops until the

stress partly or totally disappears. In the moment of stress reduction, elastic strain decreases instantly proportional to the stress reduction, and a portion of the creep strain is recovered over time. This is known as creep strain recovery and was observed for different materials [72-78].

Xin and John [72,73] performed tensile creep and tensile creep strain recovery tests on silicon carbide fiber/calcium aluminosilicate reinforced-ceramic composites. The composites used in this study contained 40 vol% Nicalon SiC fibers. The creep strain recovery ratio (R_{cr}) and the total creep strain recovery ratio (R_t) were defined to quantify the recovered strain. R_{cr} is the recovered creep strain ($\varepsilon_{cr,R}$) divided by the creep strain (ε_{cr}) for one cycle. R_t is defined as the total recovered strain ($\varepsilon_{t,R}$), divided by the total strain (ε_t) of a cycle. The total strain refers to the sum of elastic strain and creep strain (Fig. 5).
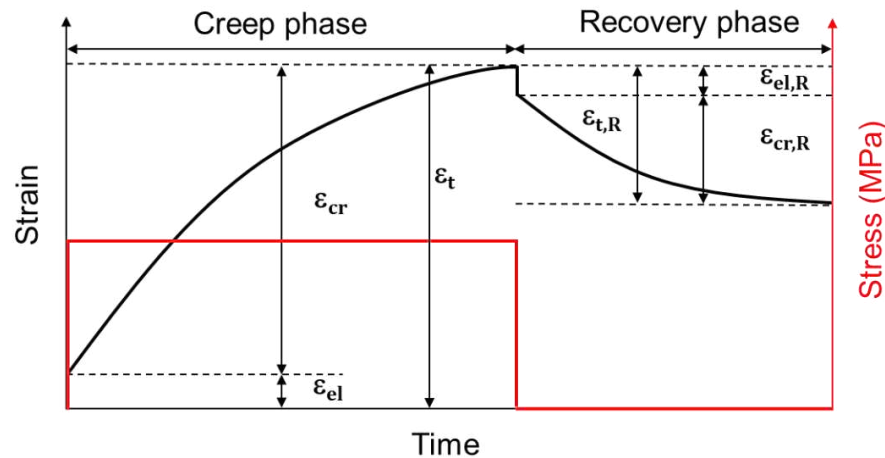
Fig. 5: Schematic of strain and stress in creep and recovery phases under loading/unloading conditions [72].

Two different creep tests under 60 and 120 MPa were carried out and after 100h the stress was reduced to 2 MPa and kept for further 100h. Results indicated that the sample tested with an initial load of 60 MPa had a 4% higher creep strain recovery ratio. In another test, two creep-recovery cycles with 40 minutes holding time with 60 MPa load were performed and reduced to 2 MPa afterwards. Observations showed that the recovery ratios were higher (17% for R_t and 8% for R_{cr}) for shorter l/u holding time. Moreover, in the following experiment, it was noted that the recovery ratios (R_{cr} and R_t) were increased in the second cycle by approximately 8% for both ratios. The reason was a notable decline in the duration of the first creep stage in the second cycle [72,73].

2.9 Mechanisms of creep recovery

Several publications [79-82] deal with creep recovery of metals and alloys, stating that under sufficient loads dislocations are piled up behind obstacles such as other dislocations, grain boundaries, and precipitates. Dislocations piling up generate internal stress usually called back-stress. In the case of dislocation movement, internal stress is defined as the net effect of spatially fluctuating stress fields on the velocity of dislocations necessary to maintain the currently applied stress [83]. When the original load is released, the internal stress leads to strain recovery generated by the dislocations moving backwards. However, in ceramic composites, the situation

is different, and creep is typically generated by various mechanisms simultaneously [84]. Because of often contributing liquid phases, creep deformation happens near grain boundaries that cause the formation of elastic and capillary stress along the grain boundaries that prevent further deformation under loading conditions. Internal stresses produce a driving force for creep strain recovery when the load is removed [85].

Internal stresses are not acting only after load decrease but are a reason for strain hardening of the materials and out of this reason the back stress is required for the definition of several constitutive models [85,86]. However, it is not feasible to measure internal stress directly. In order to determine it, the strain transient dip test [87] and the rapid loading/unloading (l/u) test [88,89] were used as indirect experimental approaches. The first one is carried out by suddenly unloading the stress on the specimen during the deformation and later holding the load constant while a strain is measured. This process may be performed several times to determine the stress that leads to a zero strain rate after unloading. In the second approach, rapid unloading and reloading are done at the strain for which the internal stress should be measured. In this method, the strain limits are raised cycle by cycle. Neu et al. [89] concluded that the stress dip test is not as accurate as the l/u test to measure internal stress at higher strain rates. Yang et al. [85] calculated the internal stress for metals using the l/u stress-strain hysteresis loop. As no reference was found for the l/u creep behaviour of refractories, this research will focus on experiments and calculations to investigate the creep strain recovery of a refractory castable under different conditions.

2.10 Models for simulation of the creep strain recovery behaviour

Creep of refractories can be simulated with a Von Mises stress based Norton Bailey creep model [63,65,71]. However, creep strain recovery of refractories has not been modelled so far. For different metals, the phenomenon was modelled with viscoelastic (viscoelastic 4-parameter Burger's model) and viscoplastic models (non-linear kinematic hardening model known as the Chaboche model) [86,90,91]. For this research, these two models were selected according to the similarity of the creep strain recovery behaviour of refractory materials investigated in this work with other materials modelled by the mentioned methods in various references [86,90-93].

2.10.1 Burger's model

Viscoelastic material behaviour is usually modelled with a combination of springs and dashpots [94]. The elastic (linear, spring) and viscous (non-linear, dashpot) parts act according to Newton's and Hook's laws, respectively [94,95]. In general, the diffusion inside an amorphous material can cause viscoelastic behaviour [96]. The governing equations for the spring and dashpots are (Eq. 17,18):
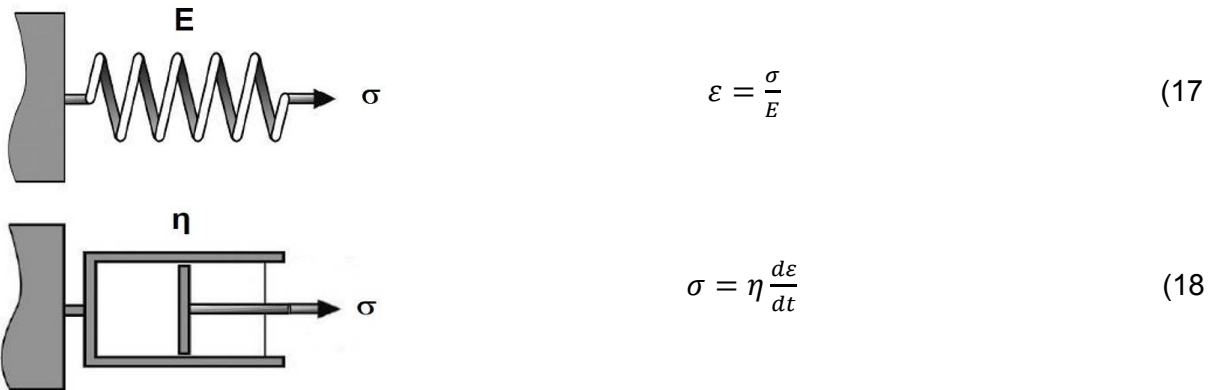
$$\varepsilon = \frac{\sigma}{E} \qquad (17$$

$$\sigma = \eta \frac{d\varepsilon}{dt} \qquad (18$$

Fig. 6: Spring (up) and dashpot (down) model [94].

Where σ is the applied stress, ε is the strain and η is the dynamic viscosity. The combination of a spring and a dashpot in a series and parallel is called Maxwell and Kelvin/Voigt model, respectively (Fig. 7). Before loading, both elements are undeformed. When a constant load is applied in the Maxwell model, the spring deforms immediately, and the dashpot piston begins to move continuously and moves as long as the load is applied. When removing the load, the spring immediately returns to its original state. The dashpot represents irreversible behaviour and does not return to its original configuration and remains deformed. In the Kelvin/Voigt model, when the loading starts the two parallel elements deform simultaneously to the same extent. Due to the connection, the spring cannot deform immediately, and its motion is slowed in comparison to the Maxwell model. By removing the load, the spring elastically moves back and causes a driving force for the dashpot to return and reach its initial position after a certain period [94].
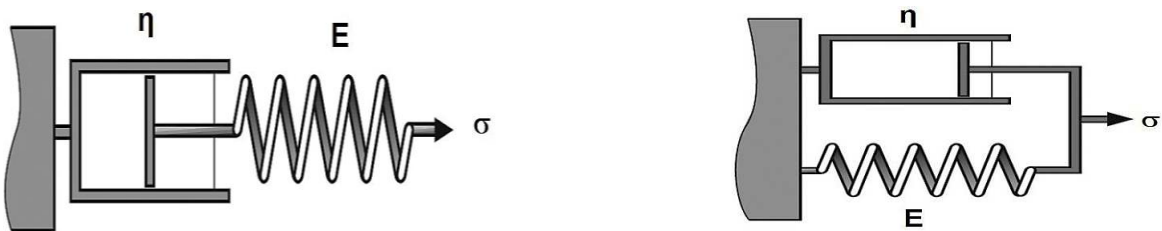
Fig. 7: Representation of Maxwell model (spring and dashpot in series-left) and Kelvin/Voigt model (spring and dashpot in parallel-right) [94].

Several references [96-102] stated that a combination of viscoelastic constitutive models can model the creep and recovery response of various materials. For example, it has been shown that Burger's model assembled by a Maxwell and Kelvin in series configuration is capable of fitting the creep and recovery behaviour for different materials such as metals, alloys and polymers. However, most of these models were applied for a single creep recovery curve (only one cycle of loading/unloading) [94,98,99]. Burger's model includes four mechanical elements (Maxwell model part: E_M and η_M and Kelvin/Voigt model part: E_K and η_K) to describe the creep and recovery behaviour (Fig. 8). The spring E_M deforms proportionally to the load, spring E_K and dashpot η_K as a couple deform viscoelastically and dashpot η_M covers the plastic deformation. Recovery is modelled with the elastic and viscoelastic elements; the element η_M is not affected by the recovery [97-103].
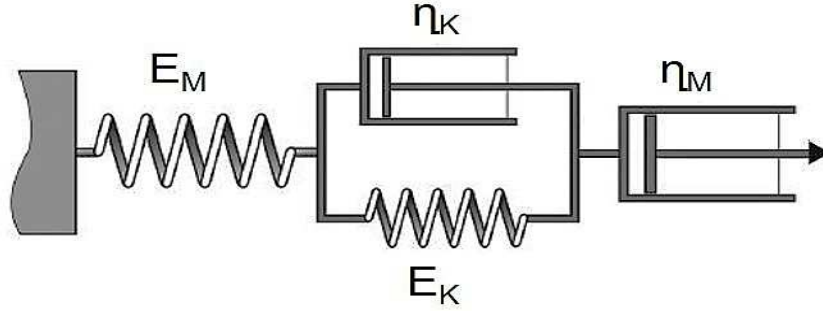
Fig. 8: Four elements of Burger's model [94].

Burger's model constitutive equation can be expressed as [97]:

$$\varepsilon(t) = \varepsilon_e + \varepsilon_p + \varepsilon_v = \frac{\sigma}{E_M} + \frac{\int \sigma dt + C_1}{\eta_M} + \left(\frac{1}{\eta_K} \int \sigma e^{\frac{E_K}{\eta_K}t} dt + C_2\right) e^{-\frac{E_K}{\eta_K}t} \tag{19}$$

Where σ is a constant load, ε_e is the instantaneous elastic strain, ε_p is the plastic strain, ε_v is the viscoelastic strain, C_1 and C_2 are constants. According to the Newtonian principle both, ε_p and ε_v are initially zero:

$$\frac{\int \sigma dt + C_1}{\eta_M} = 0 \implies C_1 = -(\int \sigma dt)|_{t=0} \tag{20}$$

$$\frac{1}{\eta_K} \int \sigma e^{\frac{E_K}{\eta_K}t} dt + C_2 = 0 \implies C_2 = -\frac{\int \sigma e^{\frac{E_K}{\eta_K}t} dt \Big|_{t=0}}{\eta_K} \tag{21}$$

Assuming creep is occurring under a constant load ($\sigma = \sigma_0$) when $t<t_1$ (t_1 is the moment of unloading) and the recovery is happening after the load is removed at $t>t_1$. For the creep section, two constants (C_1, C_2) are solved by substituting $\sigma = \sigma_0$ therefore, the strain response is:

$$\varepsilon(t) = \frac{\sigma_0}{E_M} + \frac{\sigma_0 t}{\eta_M} + \frac{\sigma_0}{E_K}\left(1 - e^{-\frac{E_K}{\eta_K}t}\right) \tag{22}$$

At the moment of removing the load, ($t = t_1$) the elastic strain is recovered instantaneously and so:

$$\varepsilon(t_1) = \varepsilon_v(t_1) + \varepsilon_d(t_1) = \frac{\sigma_0 t_1}{\eta_M} + \frac{\sigma_0}{E_K}\left(1 - e^{-\frac{E_K}{\eta_K}t_1}\right) \tag{23}$$

At $t>t_1$ during unloading, viscous strain cannot be recovered however, viscoelastic strain is recovered, and it is time-dependent:

$$E_K \varepsilon_d + \eta_k \dot{\varepsilon}_d = 0 \tag{24}$$

By solving Eq. 24, the viscoelastic strain is:

$$\varepsilon_d(t) = C\, e^{-\frac{E_K}{\eta_K}t} \tag{25}$$

Therefore, the strain in the recovery phase is:

$$\varepsilon(t_1) = \varepsilon_v(t_1) + \varepsilon_d(t_1) = \frac{\sigma_0 t_1}{\eta_M} + C\, e^{-\frac{E_K}{\eta_K}t} \tag{26}$$

The constant C can be determined from Eq. 26 if $t = t_1$.

Finally, for creep recovery, the constitutive equation is (Eq. 27):

$$\varepsilon(t) = \begin{cases} \dfrac{\sigma_0}{E_M} + \dfrac{\sigma_0 t}{\eta_M} + \dfrac{\sigma_0}{E_K}\left(1 - e^{-\frac{E_K}{\eta_K}t}\right) & (t < t_1) \\[2ex] \dfrac{\sigma_0 t_1}{\eta_M} + \dfrac{\sigma_0}{E_K}\left(1 - e^{-\frac{E_K}{\eta_K}t_1}\right)e^{-\frac{E_K}{\eta_K}(t-t_1)} & (t \geq t_1) \end{cases} \tag{27}$$

2.10.2 Non-linear kinematic hardening model (Chaboche)

Isotropic and kinematic hardening models are widely employed to describe how the materials behave under cyclic loading conditions. Hardening models are applied to describe the gradual increase in material stiffness and strength that occurs as a material undergoes repeated loading and unloading cycles [86,104-108]. Isotropic hardening models assume that the hardening behaviour of the material is the same in all directions, regardless of the applied stress. This means that the material's yield stress and stiffness increase uniformly in all directions with each loading cycle. Isotropic hardening models are commonly used to model metals and alloys that exhibit a uniform response to cyclic loading (Fig. 9) [86]. On the other hand, in kinematic hardening models, it is assumed that the direction of the applied stress affects the hardening behaviour of the material. This means that the material's yield stress and stiffness increase differently in different directions with each loading cycle. Kinematic hardening models are commonly used to model materials such as soils, polymers, and composites that exhibit a non-uniform response to cyclic loading (Fig. 10) [85,86]. In recent years, there has been a growing interest in developing more advanced hardening models that can capture both isotropic and kinematic hardening behaviour. These models, known as combined hardening models, can accurately capture the behaviour of materials that exhibit both isotropic and kinematic hardening behaviour [86].
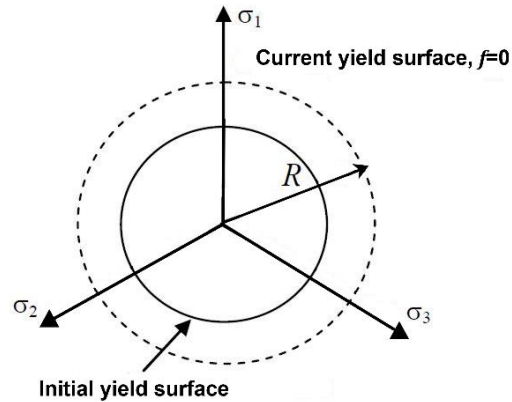
Fig. 9: Development of the yield surface in an isotropic hardening model [86].
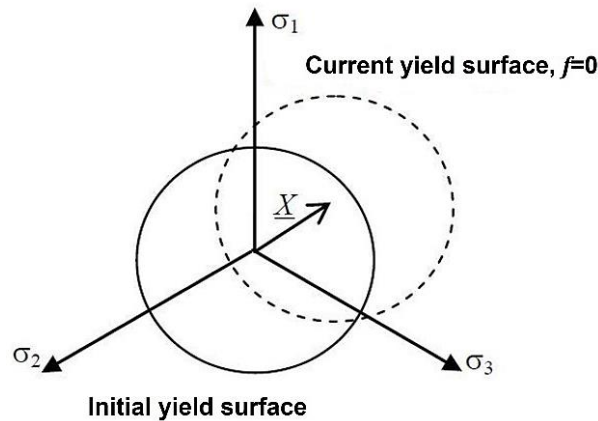
Fig. 10: Yield surface translation in a kinematic hardening model [86].

Nonlinear kinematic hardening is a modelling approach to simulate the behaviour of metals and other materials that undergo plastic deformation. The material's response to applied stresses depends on the current strain level and its previous deformation history [86]. It is assumed that the material undergoes a sequence of plastic strain increments, with each increment causing a corresponding increase in yield strength. As the material continues to deform, its yield strength increases further due to kinematic hardening, which results from the permanent reorientation of dislocations within the material [86,105]. Linear kinematic hardening models assume a linear relationship between the yield strength and the accumulated plastic strain however, the nonlinear kinematic hardening model allows for a more accurate representation of the material's response to loading conditions [86]. This is particularly useful when simulating cyclic loading, where the material undergoes repeated loading and unloading cycles. Armstrong & Frederick proposed a non-linear kinematic rule to model the viscoplastic behaviour of a material under repeated loading conditions [105]. Based on this model, many further constitutive models were developed to simulate the uniaxial and multiaxial loading such as the Chaboche model for non-linear kinematic hardening. The Chaboche model accounts for the material's nonlinear behaviour under cyclic loading, including the effects of plastic deformation, isotropic and kinematic hardening, and

damage accumulation. It is assumed that the material has both elastic and plastic components and that the plastic strain amplitude is a function of the accumulated plastic strain, the strain rate, and the stress amplitude. The behaviour of the material is described by a set of parameters in the multi-parameter Chaboche model, which must be calibrated using experimental data. The model includes a series of internal variables that describe the state of the material, such as the accumulated plastic strain, the isotropic hardening parameter, and the kinematic hardening parameter. Chaboche and other authors [86,104-108] proposed a modified model for Non-linear kinematic hardening. It is an extension of the original kinematic hardening equation, which describes the evolution of the kinematic hardening parameter changes in the material under cyclical loading (Eq. 28):

$$\underline{\dot{X}}_i = \frac{2}{3} \cdot C_i \cdot \underline{\dot{\varepsilon}}^{\,p} - \gamma_i \cdot \underline{X}_i \dot{p} \tag{28}$$

Here i is the number of parameter sets to calculate the back stress, C_i and γ_i determine the kinematic hardening characteristics, $\underline{\dot{\varepsilon}}^{\,p}$ is the viscoplastic strain rate, $\underline{X}_i$ is back stress tensor, $\dot{p}$ is the norm of the viscoplastic strain rate.

The kinematic hardening models in ABAQUS [109] aim to simulate materials under cyclic loading conditions. These models are based on the idea that by straining in one direction, the yield surface moves in the stress space, reducing the yield stress in the opposite direction [110,111]. A more advanced user material subroutine (UMAT) for the Non-linear kinematic hardening model based on Chaboche was developed by MCL (Material Center Leoben) and implemented in ABAQUS [112]. The main equations for the Chaboche model are the following [106,112]:

The flow function F in the Chaboche model is defined using Hill's criterion as follows (Eq. 29):

$$F = \left\| \underline{\sigma} - \underline{X} \right\|_H - R_0 \tag{29}$$

Where $\underline{\sigma}$ is the stress tensor, $\underline{X}$ is the back stress and the kinematic variable for kinematic hardening, and R_0 is the initial yield surface size.

The viscoplastic potential Ω plays a central role in determining the material's yielding behaviour and its ability to simulate complex time-dependent responses (Eq. 30):

$$\Omega = \frac{K}{n+1} \cdot \left(\frac{F}{K} \right)^{n+1} \tag{30}$$

Here K and n are parameters to describe the equivalent viscoplastic strain rate $\underline{\dot{\varepsilon}}^{\,p}$ as a key parameter that describes the rate of plastic deformation under time-dependent loading conditions (Eq. 31):

$$\underline{\dot{\varepsilon}}^{\,p} = \frac{\partial \Omega}{\partial \underline{\sigma}} = \frac{3}{2} \cdot \dot{p} \cdot \frac{\sigma' - X'}{\left\| \underline{\sigma} - \underline{X} \right\|_H} \quad , \quad \dot{p} = \left(\frac{F}{K} \right)^n \tag{31}$$

Where $\underline{\sigma}'$ and $\underline{X}'$ are the deviators of σ and X. Kinematic hardening in the Chaboche model is defined as follows (Eq. 32,33):

$$\underline{X} = \sum_{i=1}^{2} \underline{X}_i \tag{32}$$

$$\dot{\underline{X}}_i = \frac{2}{3} \cdot C_i \cdot \dot{\underline{\varepsilon}}^p - \gamma_i \cdot \underline{X}_i \cdot \dot{p} - \frac{C_i}{M_i} \cdot \left(\frac{\|\underline{X}\|_H}{M_i} \right)^{m_i-1} \cdot \underline{X}_i \tag{33}$$

M_i and m_i describe the static recovery effects.

3 MATERIALS CHARACTERISATION AND RESULTS

Commercially available preformed spinel (PS) and spinel forming (SF) castables were prepared by adding 6 and 8% water to the mixture of grains and fines, respectively. Table 1 shows the oxide composition of the mixtures [113].

Table 1: Oxide composition (wt%) of PS and SF castables.

	PS	SF
Al_2O_3	95	90
SiO_2	0.1	0.5
Fe_2O_3	0.3	0.2
CaO	2.5	1.2
MgO	2	8

Before sintering, the mixture was cast into prismatic moulds ($230 \cdot 110 \cdot 110$ mm³) at ambient temperature and then dried at 110 °C for 24 h. In an electrically heated furnace, a specific heating program (Fig. 11) was used for the sintering process, and the samples were cooled down to room temperature inside the furnace at a rate of 5 K/min. After sintering, specimens with different geometries were cut out of the blocks for the tests [113].
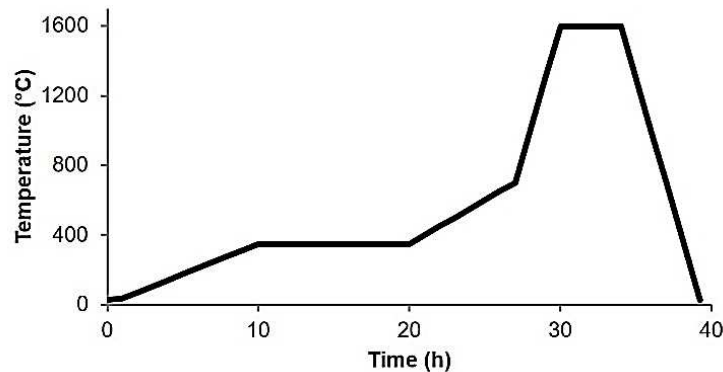
Fig. 11: Temperature program for sintering of the PS and SF castable.

3.1 Density, Porosity and Dilatometry

Before and after the sintering process, the dimensions of both castable blocks were measured with a calliper gauge. After the sintering, the PS castable showed no measurable volume expansion. It is assumed that during the sintering process between 1200 and 1300 °C a sintering shrinkage of the PS castable occurs. As there was no volume expansion in the PS castable, most probably volume expansion due to CA_6 formation was balanced by means of sintering shrinkage at a higher temperature. Usually, PS castables are formulated without microsilica content. Nevertheless, a small amount of microsilica is added frequently to the PS to support the sintering process and to place CA_6 in the matrix to enhance its hot mechanical properties [6].

Contrary to the PS castable, the SF castable showed 5.3% volume expansion during the sintering process. As these castables are bonded with calcium aluminate cement, the volume expansion was associated by the formation of the spinel and CA_6. Theoretical expansion due to the formation of spinel and hibonite was lowered to 5.3% because of adding 0.5 wt% microsilica in the mixture of the SF castable [113].

The bulk density and apparent porosity of both castables were measured according to (EN 1402-6) [114]. The true density of the castables was determined with a Micromeritics helium pycnometer (Accupyc 1330) on a ground material (to avoid closed pores) from castables after sintering. The sample volume in sample cups is determined. Based on the ideal gas equation and measuring the pressure the volume of a sample is determined. True porosity is calculated by Eq. 34:

$$\text{True Porosity} = \frac{true\ density - bulk\ density}{true\ density} \cdot 100 \tag{34}$$

Table 2 compares PS and SF castables in terms of density, porosity and volume expansion after the sintering process [113].

Table 2: Volume expansion, density, and porosity of the burnt PS and SF castables.

	Volume expansion (%)	Apparent density (gr/cm³)	True density (gr/cm³)	Apparent porosity (%)	True porosity (%)
PS	0	3.06	3.86	17.01	20.72
SF	5.3	2.81	3.77	23.37	25.46

Buhr [115] described that the addition of microsilica to the castable matrix leads to significant growth of the pores at a temperature above 1000 °C. Additionally, Ko et al. [116] stated that castables containing a higher amount of microsilica in their microstructure, generate larger pores with lower specific surface area compared to castables with no or very low microsilica addition. SF castable showed more microsilica in its matrix than PS. Results indicated that after sintering the apparent and true porosity of the SF castable is more than 5 vol% higher compared to the PS castable.

After the sintering process, thermal expansion was determined with the Netsch dilatometer DIL 420E. The results gave information about the irreversible expansion of the castables during sintering. Prismatic specimens (Fig. 12) with 50 mm in length, 5 mm in width and height were cut from the sintered castables. For each castable, three measurements were carried out at temperatures up to 1500 °C with 2h holding time.

Fig. 12: Specimen used for dilatometer test.

The tests were performed with a heating rate of 10 K/min. The evaluation showed 1.28% and 1.23% maximum linear thermal expansion at 1500 °C for the PS and the SF castable, respectively. A shrinkage of 0.02% was recorded for the PS castable during holding time. Compared to before the dilatation test, the PS castable shrank by 0.02% and the SF castable expanded by 0.02% (Fig. 13) [113].
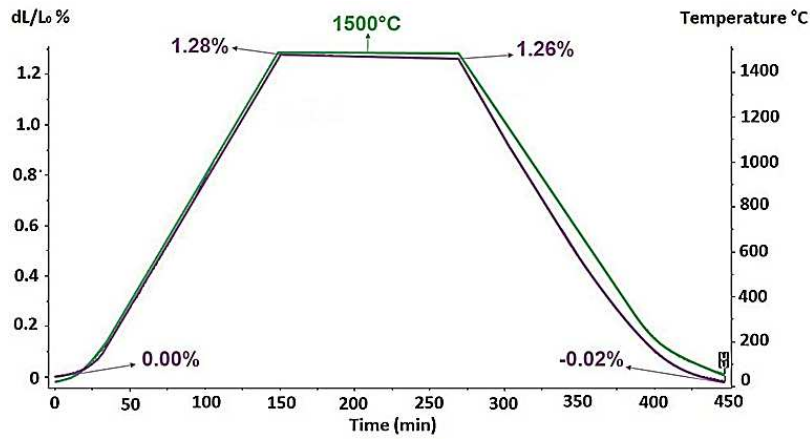
(a)
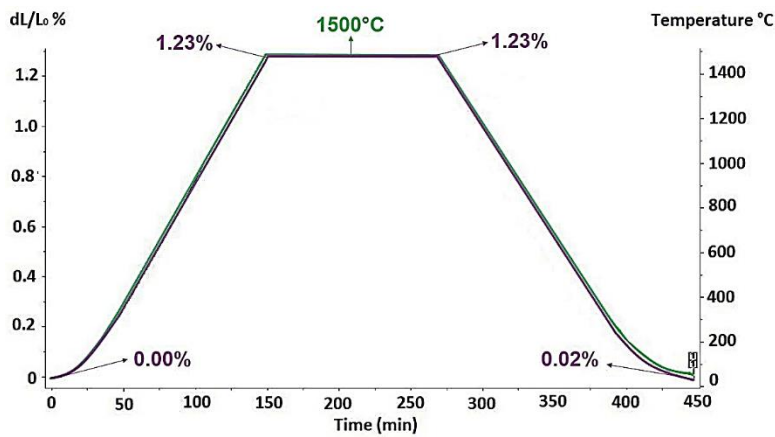
(b)

Fig. 13: Results for thermal expansion of PS (a) and SF (b) castables up to 1500 °C with 2h holding time.

3.2 SEM, XRD, thermochemical simulation and phase analysis

To evaluate the microstructure of the castable, scanning electron microscopy (SEM Carl Zeiss EVO MA15) was performed on polished sections of both castables after sintering at 1600 °C with a 4h holding time. Moreover, the phases were determined by X-ray powder diffraction quantitative analysis (Bruker D8-Advance diffractometer) for ground powders. To predict the formation of the possible phase with respect to the temperature, a thermodynamic simulation was conducted using factsage 7.2, thermfact and GTT-Technologies, Montanuniversität Leoben, GHK [113].

Fig. 14 presents an SEM picture of a polished section of the PS castable after the sintering process. By increasing the temperature during sintering, the formed CA_2 is entirely consumed by the CA_6 formation based on the reaction $CA_2+4A= CA_6$. Sako et al. [10] observed that CA_6 is located at the edge of the tabular alumina when no microsilica is available in the matrix of the PS castable while, for the case containing microsilica, the CA_6 was formed in the matrix of the castable. Moreover, the spinel added to the high alumina castable could affect the location of CA_6 in the matrix. The PS castable contains a higher amount of CaO, forming a higher amount of CA_6 in the matrix than the SF castable. It is assumed that CaO by means of diffusion at higher temperatures reacts with corundum in the Al_2O_3-rich PS castable to form CA_6 [10]. Due to 0.1 wt% of microsilica in the matrix, the needle-like CA_6 structures were generated in the matrix. Sako et al. [9,10], stated that the location of the CA_6 is related to the MgO grains as well. MgO-free castables lead to the formation of the CA_6 phase in the matrix instead of a formation at the edge of the alumina. Several researchers declared that the CA_6 crystals lead to bridging between the castable grains and effect toughening the material by acting as inner whiskers. Therefore, the bond linkage between CA_6 and spinel grains in the matrix enhances the overall thermo-mechanical behaviour, such as hot mechanical strength, creep resistance, and HMoR [117-119]. The investigated PS castable in this research with no MgO in its matrix and the location of the CA_6 confirmed this statement [113].

The crystalline phases in the PS castable were investigated by means of XRD as well. The XRD pattern indicated the formation of corundum, spinel, and CA_6 as the main phases after the sintering process in the structure of the PS castable. No other phases were detected. Additionally, the amounts of the liquid phase and its chemical composition were calculated. The chemical compositions of the castables were applied for these calculations (Table 1); the results are shown in Table 3 [113].

Table 3: Liquid phase amounts calculated by FactSage 7.2 in the matrix of the PS castable at different temperatures.

Temperature (°C)	1558	1600
Liquid phase (wt%)	0.77	0.85
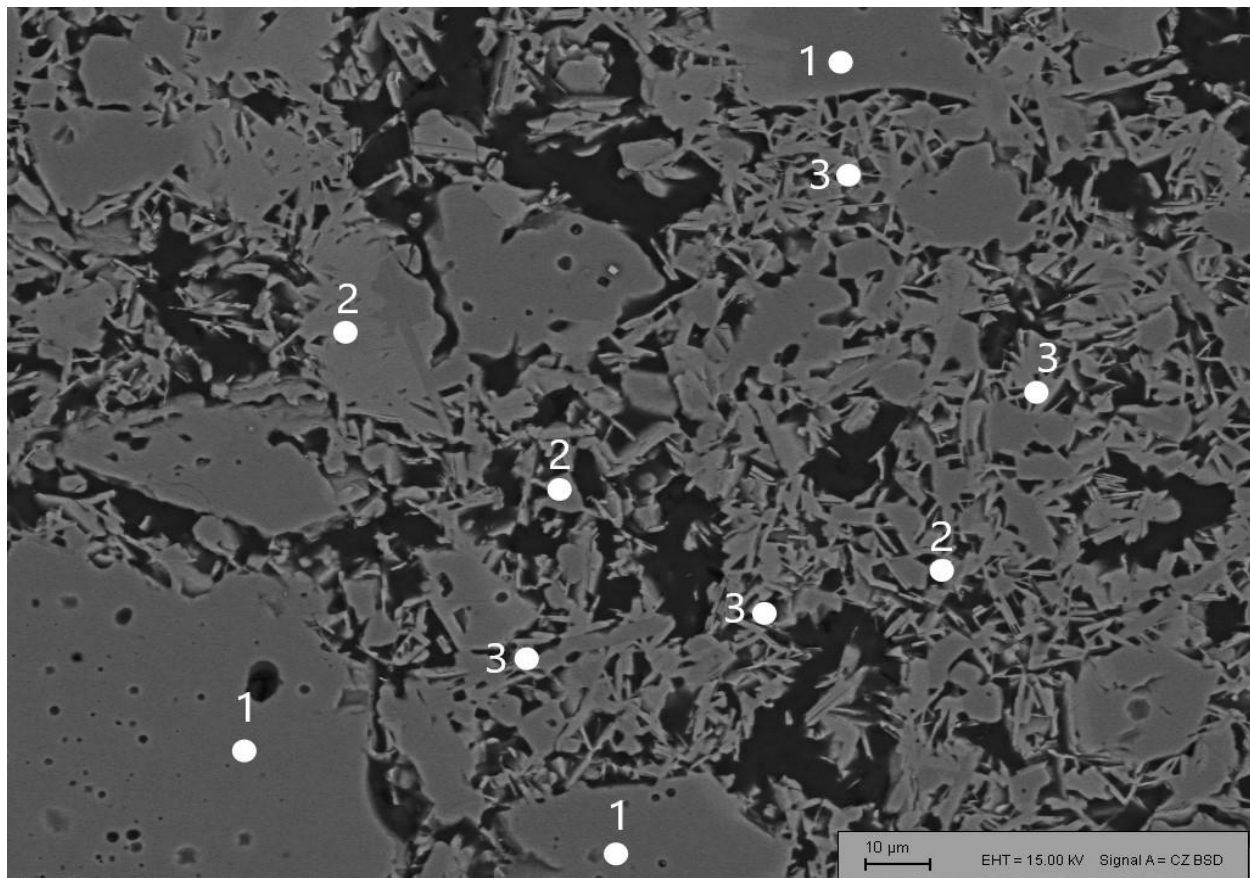
Fig. 14: SEM picture after sintering at 1600 °C (1: corundum, 2: spinel, 3: hibonite).

For the SF castable, XRD investigations showed the presence of corundum, spinel, and small amounts of CA_6 and NA_{11} after the sintering. However, the SEM analysis (Fig. 15) indicated anorthite (CAS_2) and glassy phase composed of different phases next to corundum, spinel, and CA_6. CA_2 was not found, and it is assumed that microsilica did react with CaO, leading to low melting point phases such as anorthite. Except spinel, hibonite, and alumina SEM/EDX investigations cannot detect single stoichiometric compositions of the further phases as their size is below the resolution limit of the EDX analysis [113]. The results support the expectation that analysed spots consist of an intergrowth of the further secondary phases identified by XRD together with glass phase and possibly anorthite crystallized in an amount still not detectable by XRD. Moreover, the amount of the liquid phase was calculated (Table 4) [113].
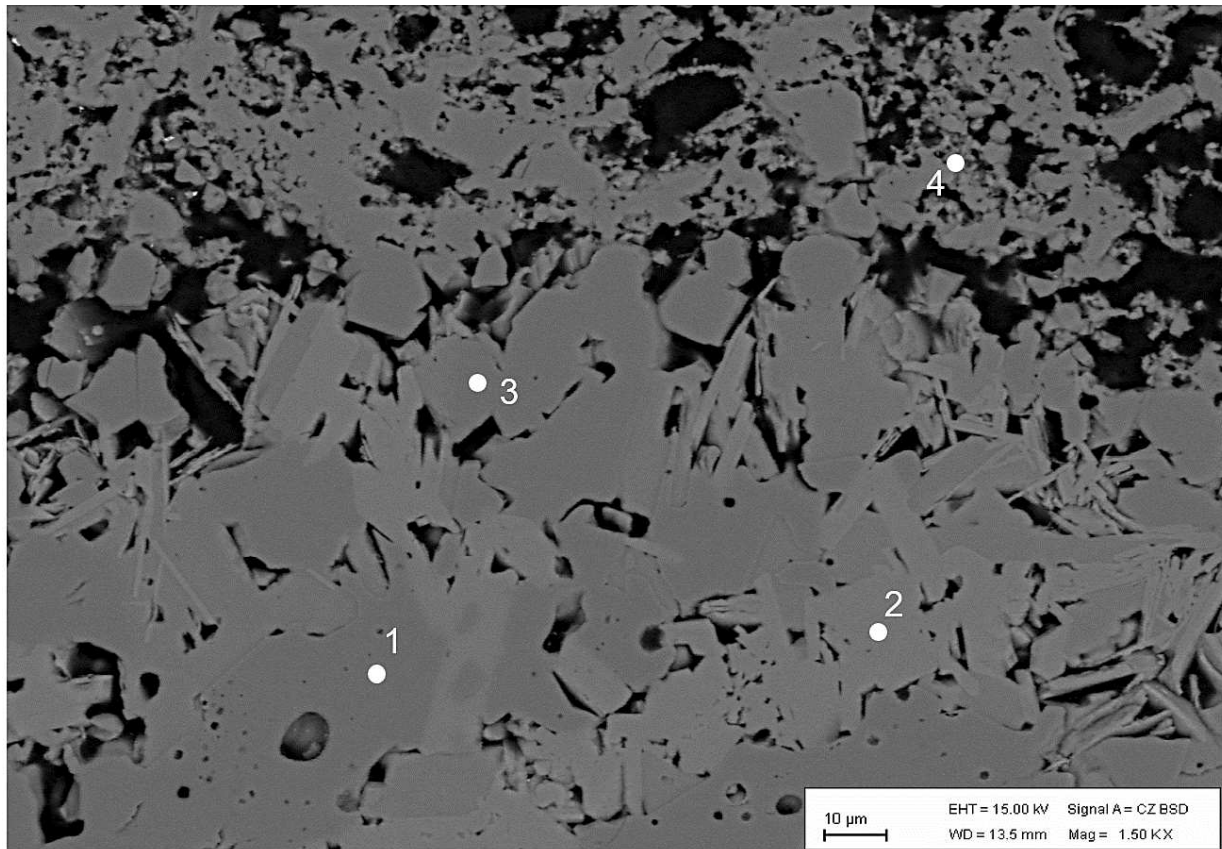
Fig. 15: SEM picture after sintering at 1600 °C (1: corundum, 2: spinel, 3: hibonite, 4: not resolved secondary phases including silicates, see text) [113].

Table 4: Liquid phase amounts calculated by FactSage 7.2 in the matrix of the castable containing 0.5 wt% microsilica at different temperatures.

Temperature (°C)	1389	1400	1500	1600
Liquid phase (wt%)	0.82	1.08	1.36	1.61

3.3 Young's Modulus

Young's modulus of the burnt castables was determined using non-destructive Resonant Frequency Damping Analysis (RFDA) from room temperature up to 1500 °C with 1 h holding time and heating and cooling rates of 5 K/min [113]. Specimens utilized for this kind of test were rectangular with a dimension of 140·25·25 mm³ (Fig. 16). In the experimental procedure (Fig. 17), the specimen is subjected to a mechanical impulse to induce flexural vibrations, leading to the generation of an acoustic signal. This acoustic signal is subsequently captured by a microphone and processed through a Fast Fourier Transformation (FFT) algorithm. By employing the FFT analysis, Young's modulus of the material can be computed from the frequency data obtained from the measurements. This method has the advantage of enabling measurements in a variety of atmospheres and at high temperatures. [120,121]. The frequencies are applied to calculate Young's modulus according to the equation Eq. 35 [67,121].

$$E = 0.9465 \cdot \left(\frac{m \cdot f_f^2}{b} \right) \cdot \left(\frac{L^3}{h^3} \right) \cdot T_1 \qquad (35$$

Where m stands for the mass of the specimen (g), f_f is the flexural resonant frequency (Hz), b is the specimen width (mm), L is the length of the specimen (mm), h is the height of the specimen (mm) and T_1 is correction factor depending on the ratio of the length of the specimen to the Poisson's ratio and thickness.
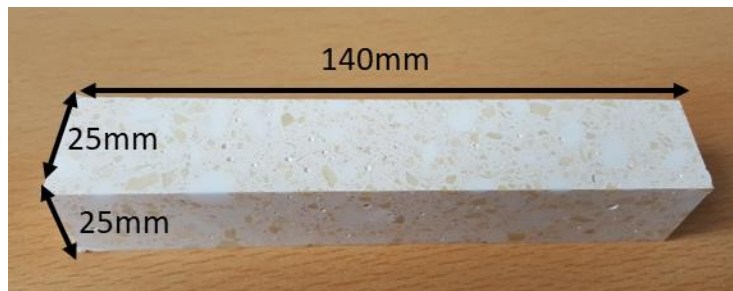
Fig. 16: SF castable specimen after sintering and testing.
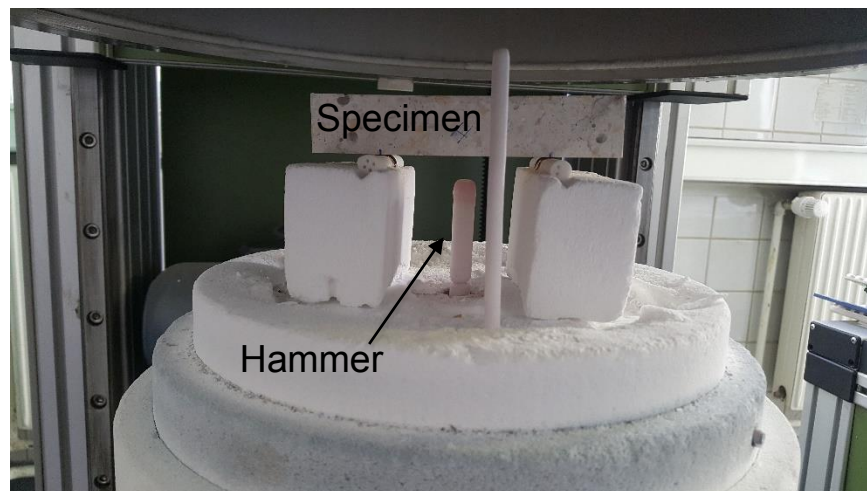
Fig. 17: The specimen in the RFDA furnace.

Fig. 18 represents the results of Young's modulus for the PS and the SF castables (performing 3 tests for each castable). Up to 1500 °C Young's modulus of the PS castable decreased very slightly, and during cooling an increase was observed as expected (Fig. 18-a). For the SF castable the decrease during heating to 1100 °C, was smaller. Above 1100 °C, a more significant decrease was observed (Fig. 18-b).
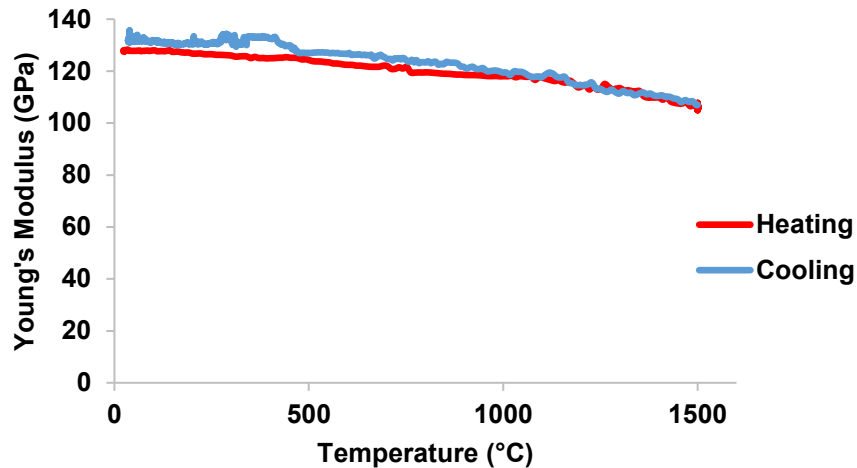
(a)
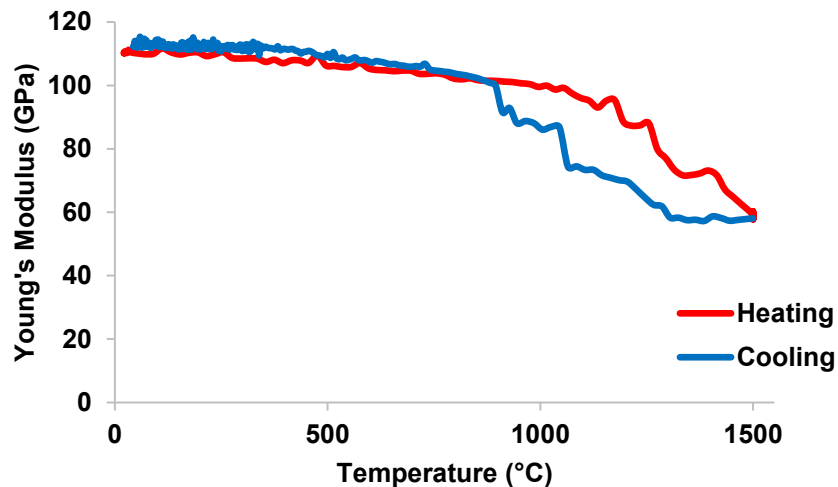
(b)

Fig. 18: Young's modulus as a function of the temperature for PS (a) and SF (b).

In multi-phase polycrystalline materials, Young's modulus is affected by phase changes and the evolution of the microstructure during the heating [122]. The decrease in Young's modulus of the SF castable above 1000 °C is governed mainly by forming liquid phases in the castable matrix. Young's modulus of 60 GPa was observed at 1500 °C. During the cooling, Young's modulus showed a hysteresis and reached the heating-up curve at approximately 900 °C [113].

3.4 Uniaxial compressive creep of the PS and the SF castables

Cylindrical specimens with a diameter of 35 mm and a length of 70 mm were drilled from the sintered blocks. The drilling step was carried out with a low feed rate to avoid cracking and ensure as flat as possible surfaces. The cylindrical specimens were cut for plane-parallel bottom and top surfaces to ensure an even load distribution [62,66]. Afterwards, the specimens were dried at a temperature of 120 °C in a furnace. To stabilise it during heating, a 100 N compressive load was applied to the specimen. The rear and front extensometers were attached to the surface of the specimen after one hour of holding time at the testing temperature. Afterwards, the load was applied. Compressive creep tests were carried out at 1500 °C. For each castable, 3 tests were performed. A constant load of 7 MPa (PS) and 1.75 MPa (SF) was applied. Figs. 19 and 20 show the total strain over time.
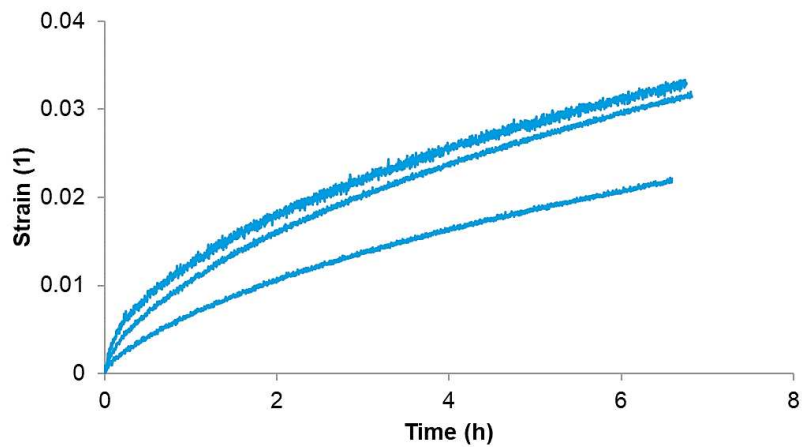
Fig. 19: Compressive creep curves of PS castable measured at 1500 °C under 7 MPa.
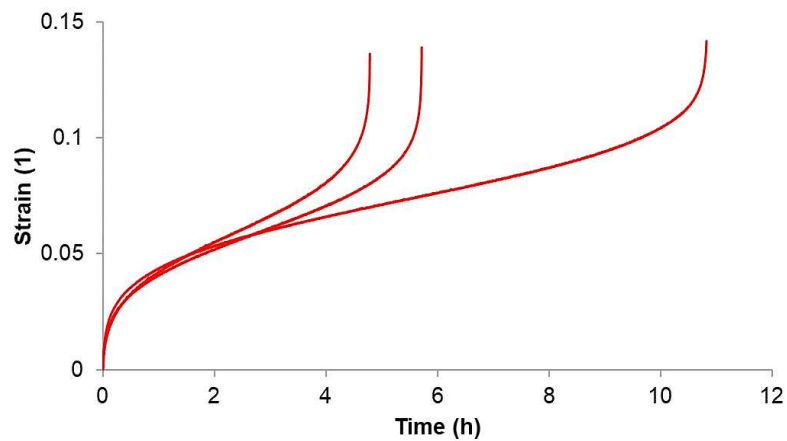
Fig. 20: Compressive creep curves of SF castable measured at 1500 °C under 1.75 MPa.

At 1500 °C and 7 MPa, the PS castable showed much lower creep strain in comparison to SF and after 7 h the creep stages were not completed while at the same temperature, but at a smaller load (1.75 MPa), the SF castable showed three complete creep stages. The in-situ spinel formation and variations in microstructure, porosity, and density account for the higher creep strain rate noted for the SF castable. Compared to the SF castable, the PS castable has a higher density and a lower porosity (Table 2). Furthermore, adding the preformed spinel to the castable as well as the formation of CA_6 in the matrix of PS castable improves the hot strength in the matrix. Besides, no liquid phases were formed in the PS castable due to the low amount of silica (Table 3). According to the results of thermochemical simulations, liquid phases appear in the SF castable at a temperature of 1389 °C (Table 4). Moreover, the viscosity of the liquid phases decreases as temperature rises. It is assumed that at 1500 °C 1.36 wt% liquid phases are located between the grain boundaries. Under compressive pressure, these grains slide over each other and enhance the creep rate of the SF castable. Because of the more pronounced creep behaviour, the SF castable was selected for further investigations.

The compressive creep tests were carried out under different loadings and temperatures (Table 5). In order to achieve the three creep stages for each temperature, three loads were defined and three tests were conducted for each load (nine tests per temperature).

Table 5: Temperatures and applied loads for the uniaxial compressive creep tests.

Temperature (°C)	Stress (MPa)
1300	7-7.5-8
1400	4.5-5-5.5
1500	3-3.5-3.75

The results (Fig. 21) demonstrated that, in contrast to the secondary and tertiary stages, there were small differences between test repetitions conducted under the same circumstances for the primary creep stage. The impact of the material inhomogeneities was greater in the second and third stages. that for the primary creep stage, the deviations between repetitions of the tests under the same conditions were small compared to those for the secondary and tertiary stages. The material inhomogeneities exhibited a higher impact on the second and third stages. This heterogeneity is due to differences in density, porosity and mechanical properties between the specimens used for this part of the testing. For all three temperatures, a lower load represented a longer testing period. At 1300 and 1400 °C, the lower load (7 MPa and 4.5 MPa) achieved higher creep strain, however at 1500 °C the middle load (3.5 MPa) showed maximum creep strain. The longest creep time (6.5 h) was observed under 1400 °C with the lowest load (7 MPa) [113].
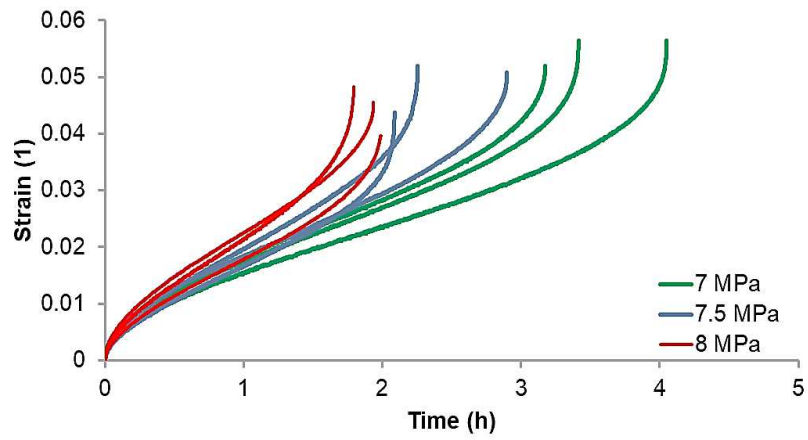
(a)
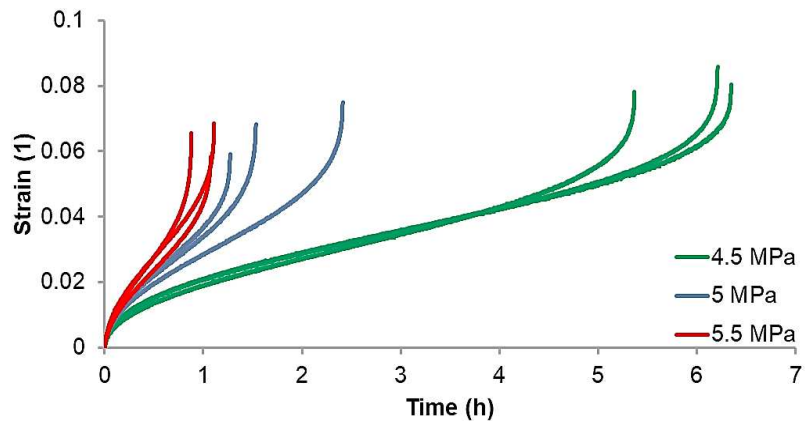
(b)
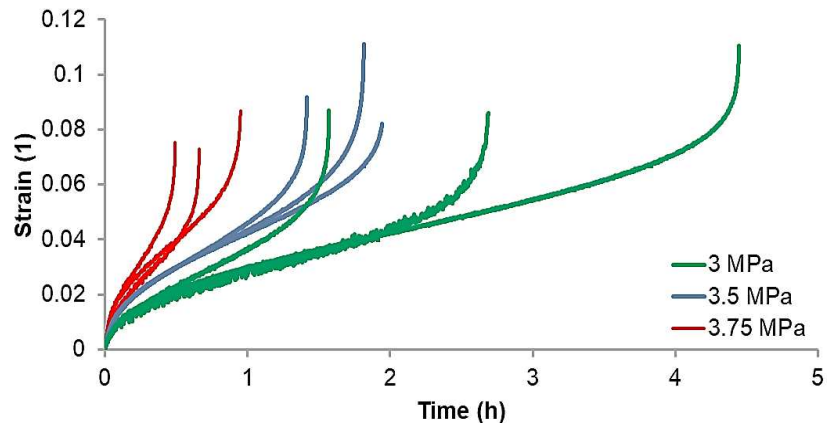
(c)

Fig. 21: Compressive creep test curves (three stages) measured at 1300 °C (a), 1400 °C (b), 1500 °C (c).

3.5 Determination, evaluation, and statistical study of the compressive creep parameters

For the creep parameters evaluation, the measurement's mean values over time were used. Norton-Bailey creep equation was applied to describe the material creep behaviour in all three stages [63,71]. In order to identify the Norton-Bailey creep parameters (a, n, k) of the three creep stages, it was required to determine the start and end of the creep stages. Therefore, a developed automatic MATLAB identification procedure to detect the creep stage transition was applied [70,71]. Fig. 22 presents the transition of the creep stages as determined by the procedure for one specific case.
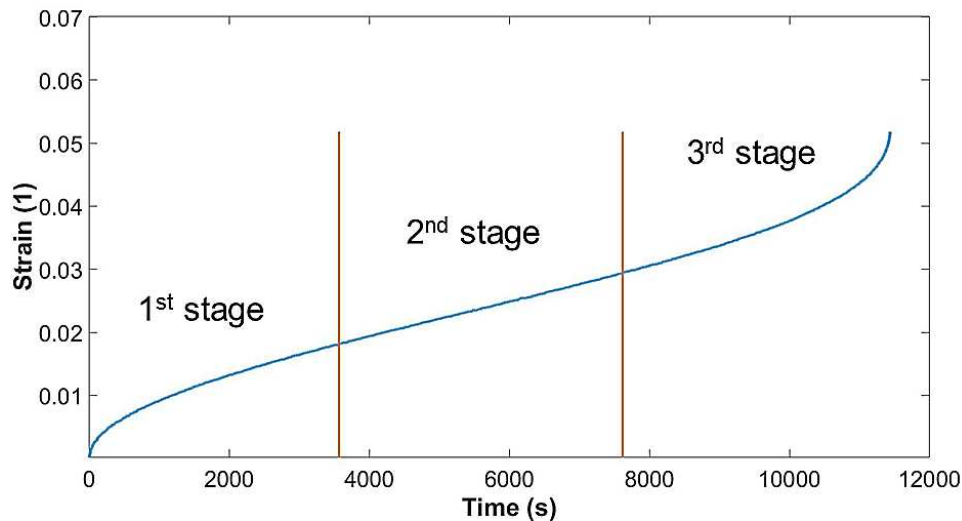
Fig. 22: Creep curve with the transition of the creep stages (1300 °C under 7 MPa).

From the separated creep curves, the Norton-Bailey creep parameters are determined for each stage separately using the strain hardening/softening form of the creep rate equation (Eq.14) [66]. Using the Levenberg-Marquardt reduced gradient method and an inverse evaluation procedure, the creep parameters for each stage were determined [63,68]. Theoretically, for the inverse evaluation of the creep parameters for each temperature, a minimum of two measurements with different loads is sufficient to determine the parameters as input data. The input data for the inverse evaluation can be chosen in a variety of ways. Statistical analysis of the creep behaviour of the SF castable was conducted to analyse the influence of different input data on the final creep parameters and to select the most representative input data. For this purpose, as there are nine measurements, for each stage, all possible combinations of 2 out of 9, to 9 out of 9 were selected as input data and the creep parameters of each stage were inversely evaluated for the different number of measurements in combination. For each dataset, at least two measurements were selected from two different loads. In Table 6, the number of datasets for the different number of measurements in the combination are listed.

Table 6: Numbers of datasets determined for different numbers of measurements in the combinations [113].

Number of measurements in combination	2	3	4	5	6	7	8	9
Number of datasets	27	81	126	126	84	36	9	1

A detailed description of the method is given in [123]. Different input datasets were compared by calculating the mean value ($\bar{y}$) and the standard deviation (S) for a, n, and $\log K$ with respect to the different load combinations. For the case of all nine measurements in one combination, the calculation of a standard deviation is not possible. In Figs. 23,24 and 25, the results for the standard deviations for three stages under three temperatures are presented.
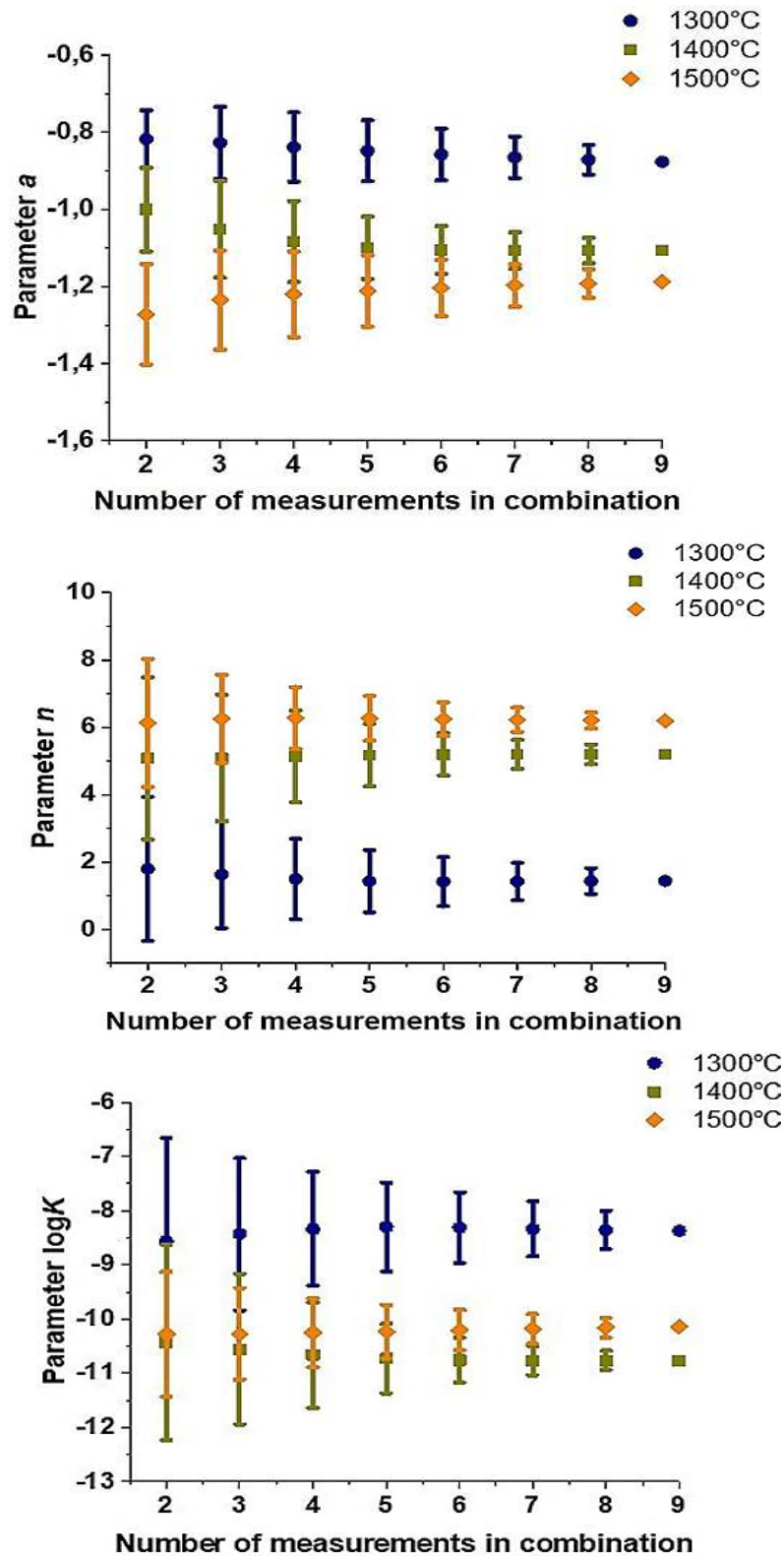
Fig. 23: Mean values and standard deviations for the parameters a, n, and $\log K$ (K [MPa^{-n} s^{-1}]) (first stage) for different numbers of measurements in the combinations for three temperatures (1300, 1400, 1500 °C).
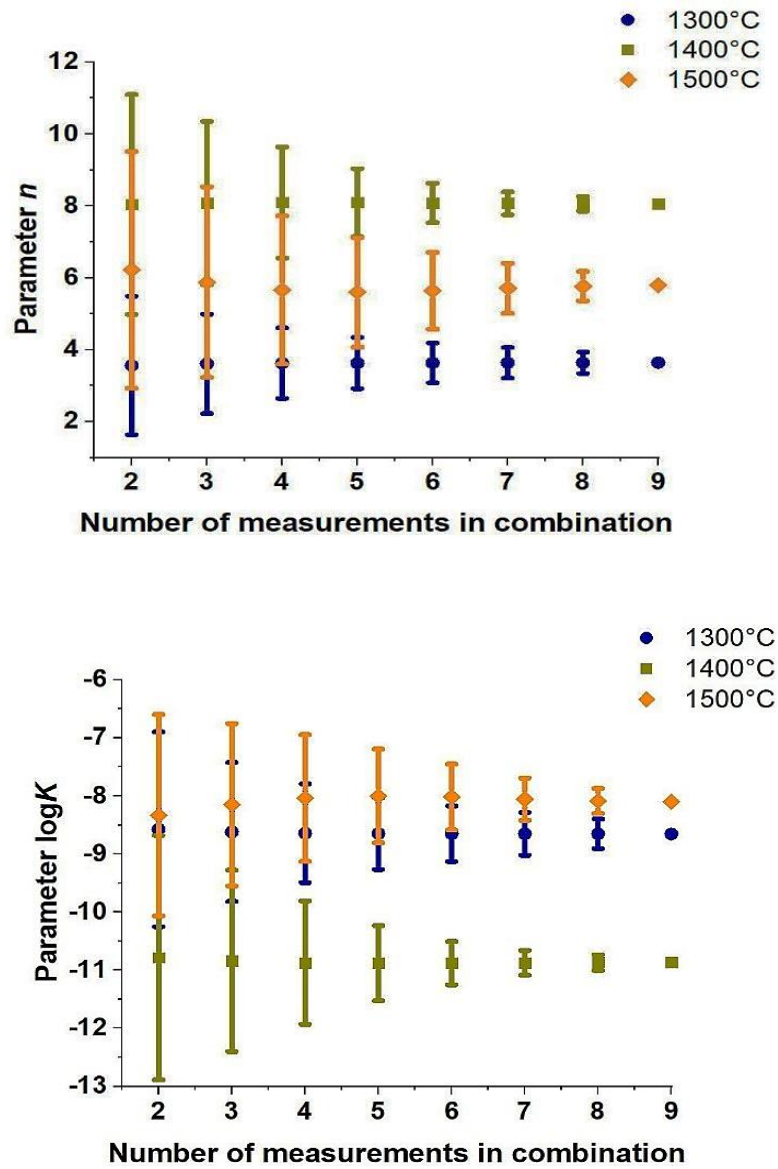
Fig. 24: Mean values and standard deviations for the parameters n, and $\log K$ (K [MPa^{-n} s^{-1}]) (second stage) for different numbers of measurements in the combinations for three temperatures (1300, 1400, 1500 °C).
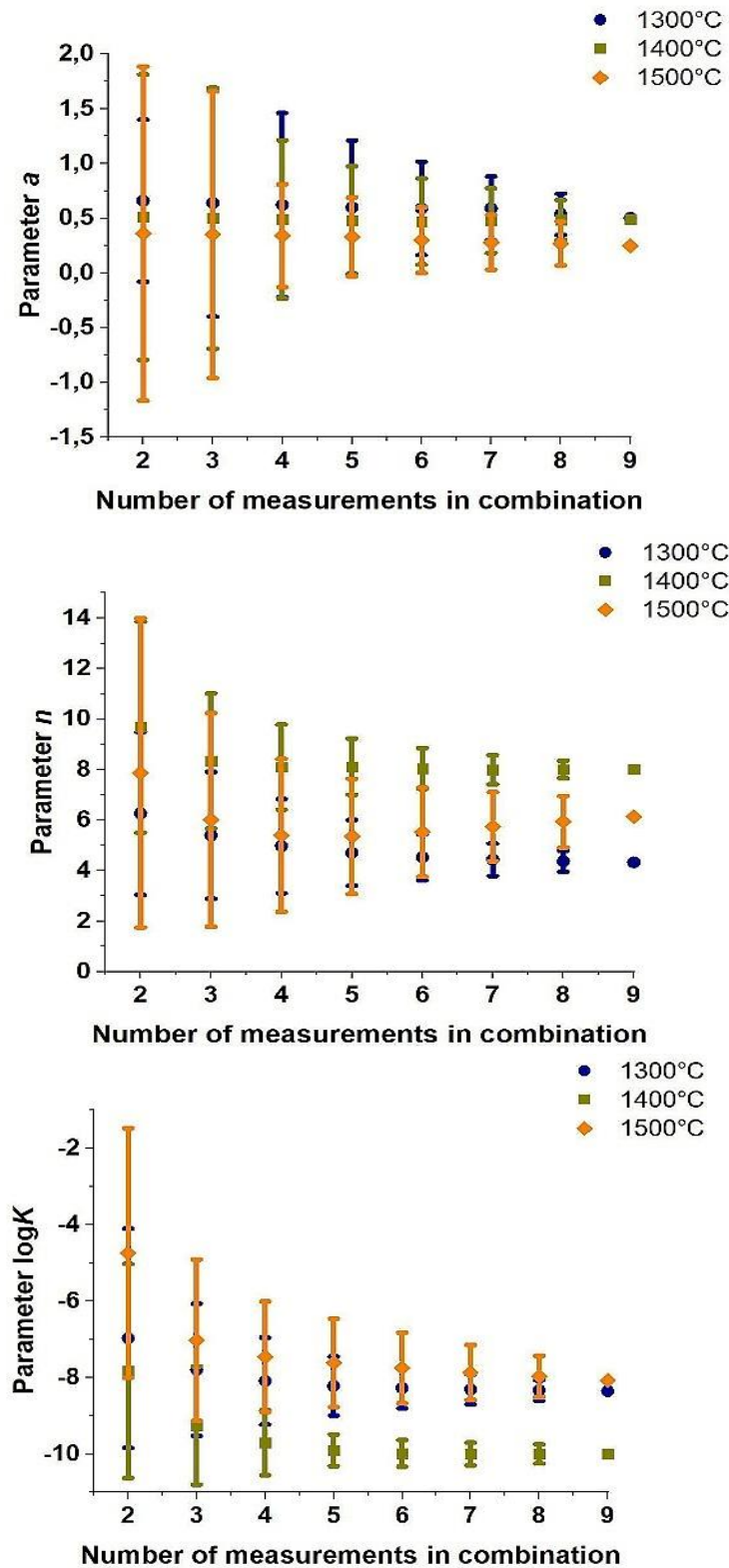
Fig. 25: Mean values and standard deviations for the parameters a, n, **and** $\log K$ (K **[MPa^{-n} s^{-1}]) (third stage) for different numbers of measurements in the combinations for three temperatures (1300, 1400, 1500 °C).**

Results indicated that the standard deviations of different datasets decreased with an increasing number of the measurements in combinations for all three stages. Besides, for the first stage, the mean value of n remained constant for three temperatures, while the mean values of a and $\log k$ depended on the temperature. A similar trend was observed for the second stage. For the third stage, the mean of a remained more or less constant for the three temperatures [113]; however, the mean of n and $\log k$ decreased. Furthermore, 99% confidence intervals were determined for the creep parameters for different load combinations using Eq. 36 [123,124].

$$|\mu - \bar{y}| \leq \frac{t_{\alpha/2,n-1}S}{\sqrt{n}}$$

(36

Here μ is the mean value for the whole population, $|\mu - \bar{y}|$ defines the difference between the mean value of the whole population and the mean value of the dataset ($\bar{y}$), n is the dataset population, α is the significance threshold, and S is dataset standard deviation. t is calculated using the t-distribution table based on the dataset's degree of freedom (n - 1) and the confidence interval percentage "100 (1 - α)" [124]. For the mean difference, the right side of Eq. 36 is the 100 (1- α) percent confidence interval.

The results demonstrated that the confidence intervals for a and n significantly decreased as the number of combined measurements for each creep stage increased from two to six, and they increased when the number of combined measurements exceeded six [113]. Fig. 26 shows the results obtained by a t-test, considering the 99% confidence interval for the first stage [123].
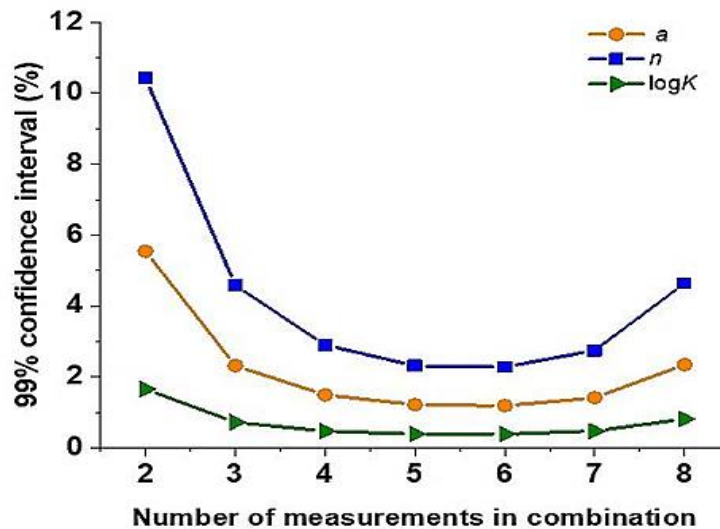
Fig. 26: 99% confidence interval expressed in percent of the respective mean value as a function of the number of used measurements.

The comparison of the results showed that the combination of six out of the nine measurements exhibited the lowest confidence interval. This means the result with a combination of six measurements offers the optimum significance. Although this study enables quantifying the

deviations between different creep parameters determined by different combinations, this is not possible for the evaluation of all nine curves. Table 7 shows the compressive creep parameters with the combination of nine and six measurements. There is a relatively small difference between the parameters that the combinations of six and nine measurements determined, with maximum deviations of $\log K$, a, and n of 4.46%, 8.57%, and 10.42%, respectively [113].

Table 7: Uniaxial compressive creep parameters with the combination of six (a) and nine (b) measurements for different temperatures and stages (K[MPa^{-n} s^{-1}]).

	Primary creep stage			Secondary creep stage	
T [°C]	$\log K^*$	a	n	$\log K$	n
1300	-8.31±0.65	-0.85±0.06	1.41±0.75	-8.64±0.48	3.63±0.55
1400	-10.75±0.41	-1.10±0.05	5.16±0.63	-10.87±0.37	8.08±0.54
1500	-10.20±0.37	-1.20±0.07	6.24±0.49	-8.01±0.56	5.63±1.06

Tertiary creep stage		
$\log K$	a	n
-8.27±0.53	0.66±0.42	4.53±0.91
-9.98±0.12	0.51±0.39	8.04±0.81
-7.74±0.92	0.32±0.86	5.52±1.76

(a)

	Primary creep stage			Secondary creep stage		Tertiary creep stage		
T [°C]	$\log K^*$	a	n	$\log K$	n	$\log K$	a	n
1300	-8.37	-0.87	1.43	-8.65	3.63	-8.35	0.50	4.33
1400	-10.76	-1.10	5.19	-10.86	8.05	-10.35	0.49	8.02
1500	-10.14	-1.18	6.19	-8.09	5.79	-8.07	0.35	6.14

(b)

The experimental curves for three temperatures for only one load and the first stage were plotted in Fig. 27. Predicted curves using the mean of combined six and nine curves represented a close fitting to the experimental one. This procedure was carried out for all other loads and stages. Considering the different possibilities for determining the creep parameters, the combination of

nine curves will be selected to evaluate the creep parameters applied for thermomechanical modelling.
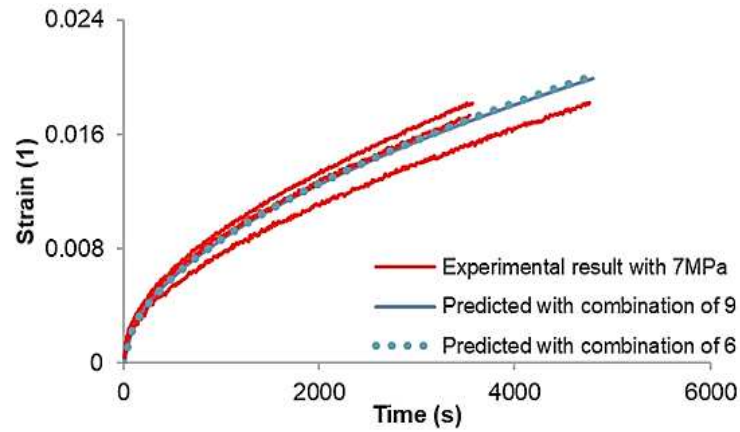
(a)
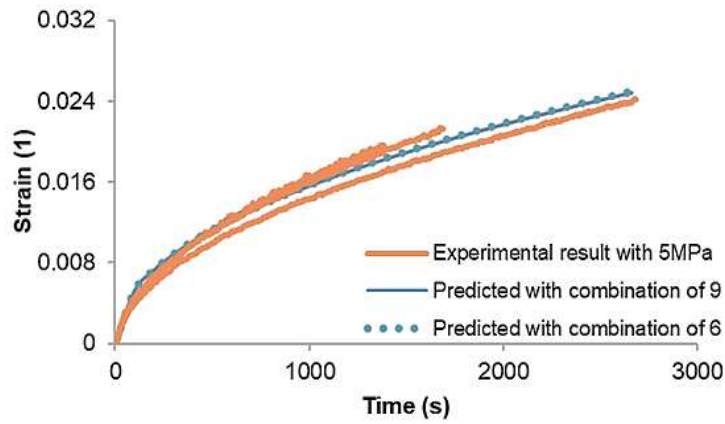
(b)
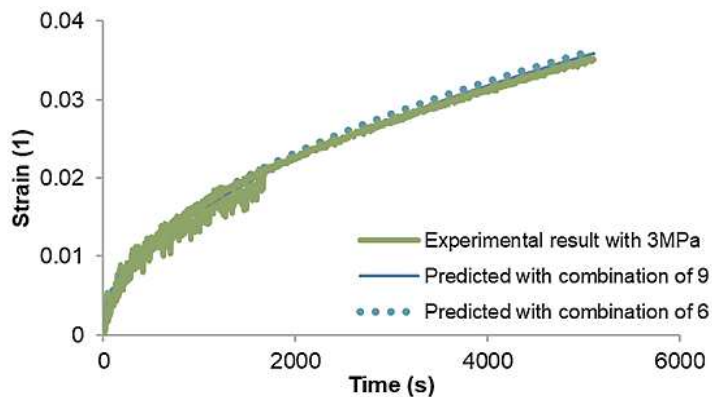
(C)

Fig. 27: Primary creep stage prediction for 1300 (a), 1400 (b) and 1500 °C (c) using the mean value of 6 and 9 curves combination.

Table 7 shows that for the first stage, the temperature-dependent function k and the strain component indicate a decrease with an increase in temperature. However, the stress component n indicates an increase with increasing temperature. Moreover, the creep parameters of the first stage for temperatures 1400 and 1500 °C were very similar. Therefore, it was decided to provide one series of parameters for these temperatures with the same a and n values but different k. For this purpose, 18 curves were selected (9 curves from each temperature) and the Norton-Bailey creep parameters were calculated (Table 8). With the help of determined creep parameters, all the experimental creep curves at both temperatures were fitted. Fig. 28 represents the fit of experimental curves for only one load and the first stage [113].

Table 8: Compressive creep parameters evaluated by combining eighteen measurements at 1400 and 1500 °C for the first stage.

Temperature °C	log$k$	a	n
1400	-11.17		
		-1.29	5.74
1500	-9.80		
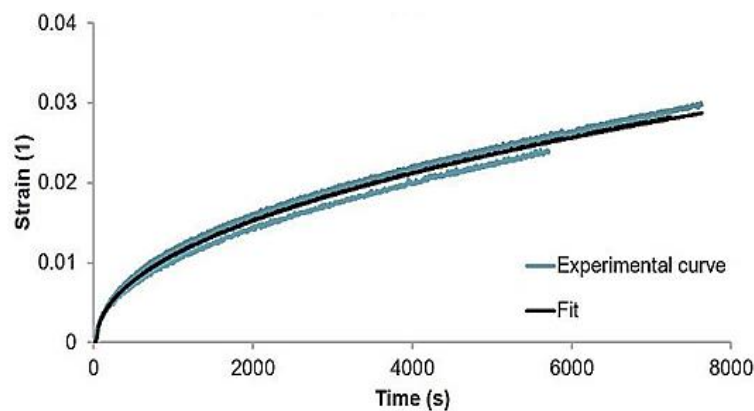
(a)
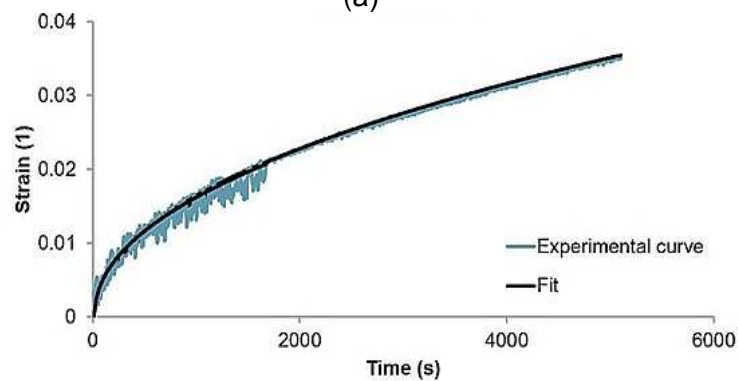
(b)

Fig. 28: Fit of experimental curves with the same a and n values and different k values at 1400 (a) and 1500 °C (b).

The residuals for both fits were calculated using Eq. 37, where m is the number of evaluation points (considering 1800 data points for each curve), while ε_p and ε_e are the predicted and experimental creep strains, respectively. The results (Table 9) show that one series of creep parameters determined from tests at 1400 and 1500 °C would not change the residual compared to the independent determination of creep parameters for each temperature [113,123].

$$\text{Fitting residual}= \frac{1}{m} \sqrt{\frac{\sum_{i=1}^{1800}\left(\varepsilon_p - \varepsilon_e\right)^2}{1800}}$$
(37

Table 9: Residuals of the fits for the first creep stage with the combinations of nine and eighteen measurements at 1400 and 1500 °C.

Residual of fitting	Combination of 9 measurements	Combination of 18 measurements
1400 °C	$2.31 \cdot 10^{-2}$	$2.53 \cdot 10^{-2}$
1500 °C	$2.12 \cdot 10^{-2}$	$2.34 \cdot 10^{-2}$

4 LOADING/UNLOADING COMPRESSIVE CREEP TESTING [125]

For l/u testing, the procedure is equivalent to the uniaxial compressive creep testing procedure explained in Chapter 3, but the SF castable samples were loaded with two different loads for defined periods in each test. After reaching the testing temperature of 1300 °C and waiting for 1 h for temperature homogenisation, 5 MPa load was applied with a maximum loading rate of 0.88 mm/min. In the different tests, the load was reduced to 0.1 MPa after 10, 30, 60, and 90 minutes. Each loading and subsequent unloading is called one cycle. Several evaluations were carried out for each cycle to compare the l/u effect. The result of test 1 is shown in Fig. 29 with a 5 MPa load for 10 minutes and unloading to 0.1 MPa with a holding time of 10 minutes at 0.1 MPa.
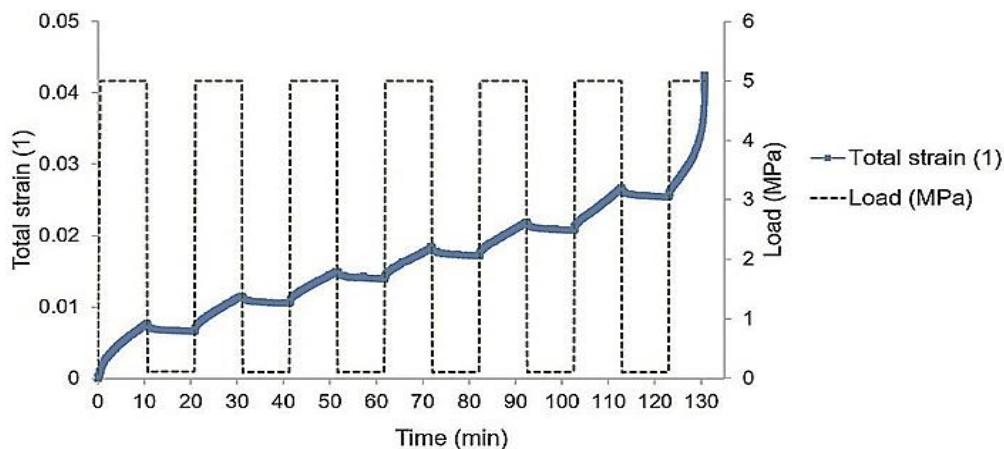
Fig. 29: Total strain for l/u test 1 with 5 MPa loading and unloading to 0.1 MPa, and 10 minutes l/u holding.

Six cycles were obtained until failure occurred. The last loading phase, i.e. the start of the seventh cycle was not considered for calculations due to the missing recovery phase. After more than 2h, a total creep strain of 0.044 was observed. For each cycle total strain (ε_t), creep strain (ε_{cr}), total creep strain recovery ($\varepsilon_{t,\,R}$), creep strain recovery ($\varepsilon_{cr,\,R}$), elastic recovery ratio (R_E) (which is the elastic strain (ε_{el}) divided by the total strain (ε_t) at the end of each cycle), total strain recovery ratio (R_t) and creep strain recovery ratio (R_{cr}) were measured and calculated [72,73]. Table 10 represents the results of the evaluations for test 1.

Table 10: Creep and recovery strains and recovery ratios calculated from test 1.

Cycle	$\varepsilon_t(10^{-3})$	$\varepsilon_{cr}(10^{-3})$	$\varepsilon_{t,R}(10^{-3})$	$\varepsilon_{cr,R}(10^{-3})$	R_E (%)	R_t(%)	R_{cr}(%)
1	7.66	7.59	1.07	1.01	0.93	13.96	13.30
2	4.97	4.90	1.01	0.97	1.43	20.32	19.79
3	4.39	4.31	0.99	0.94	1.62	22.55	21.80
4	4.44	4.37	1.21	1.14	1.60	27.25	26.08

5	4.79	4.72	1.22	1.15	1.48	25.46	24.36
6	6.01	5.94	1.25	1.18	1.18	20.79	19.86

It can be seen that the total strain per cycle shows a minimum in cycle 3. The trend is similar for the total strain recovery ($\varepsilon_{t, R}$) and the creep strain recovery ($\varepsilon_{cr, R}$). This behaviour is probably due to the transition from the first stage (cycles 1-3) to the second stage (cycles 3-5) and finally to the third stage (cycle 6). R_t, R_{cr}, reached a maximum during cycle 4 and R_E showed a maximum in cycle 3.

Test 2 (Fig. 30) was carried out with 30 minutes holding time. ε_t and ε_{cr} reached a minimum in cycle two (1-2 h), this is in the same time range as in test 1. Strain recovery ratios increase with the cycles in this case.
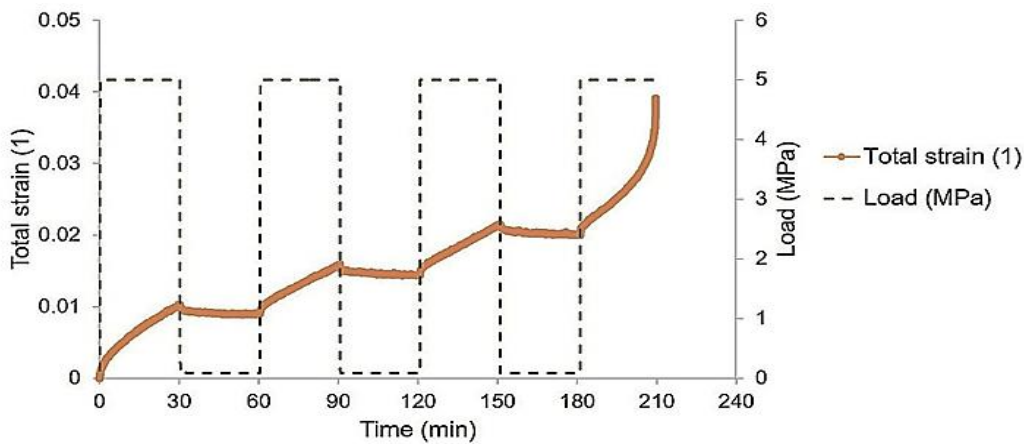
Fig. 30: Total strain for l/u test 2 with 5 MPa loading and unloading to 0.1 MPa, and 30 minutes l/u holding.

Table 11: Creep and recovery strains and recovery ratios calculated from test 2.

Cycle	$\varepsilon_t(10^{-3})$	$\varepsilon_{cr}(10^{-3})$	$\varepsilon_{t,R}(10^{-3})$	$\varepsilon_{cr,R}(10^{-3})$	$R_E(\%)$	$R_t(\%)$	$R_{cr}(\%)$
1	10.26	10.19	1.29	1.22	0.69	12.57	11.97
2	6.91	6.84	1.45	1.38	1.03	20.98	20.17
3	7.08	7.01	1.51	1.44	1.08	21.32	20.54

For tests 3 and 4, holding times were 60 and 90 minutes, respectively. Both samples fractured in the second cycle (Figs. 31,32). For both tests, changes in the creep stage were observed during the loading phases. Test 4 with 90 minutes of holding time represents the entire first and second creep stages and partially the third creep stage before fracture. In the second cycle, after changing the load from 0.1 to 5 MPa, predominantly the third creep stage is observed.
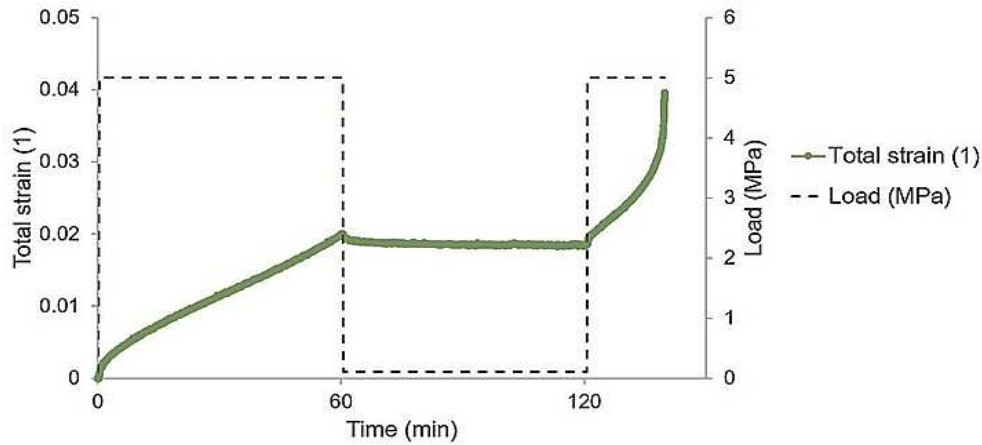
Fig. 31: Total strain for l/u test 3 with 5 MPa loading and unloading to 0.1 MPa, and 60 minutes l/u holding.

Table 12: Creep and recovery strains and recovery ratios calculated from test 3.

Cycle	$\varepsilon_t(10^{-3})$	$\varepsilon_{cr}(10^{-3})$	$\varepsilon_{t,R}(10^{-3})$	$\varepsilon_{cr,R}(10^{-3})$	$R_E(\%)$	$R_t(\%)$	$R_{cr}(\%)$
1	19.98	19.91	1.35	1.28	0.35	6.75	6.42
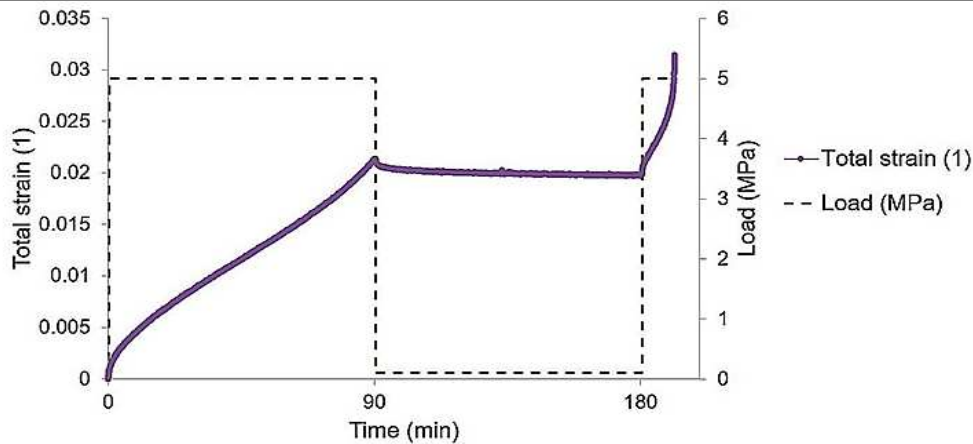
Fig. 32: Total strain for l/u test 4 with 5 MPa loading and unloading to 0.1 MPa, and 90 minutes l/u holding.

Table 13: Creep and recovery strains and recovery ratios calculated from test 4.

Cycle	$\varepsilon_t(10^{-3})$	$\varepsilon_{cr}(10^{-3})$	$\varepsilon_{t,R}(10^{-3})$	$\varepsilon_{cr,R}(10^{-3})$	$R_E(\%)$	$R_t(\%)$	$R_{cr}(\%)$
1	21.36	21.29	1.57	1.50	0.33	7.35	7.04

To clarify the influence of the holding time, the first cycles of tests 1 to 4 were further investigated (Fig. 33). Corresponding creep and recovery strain and recovery ratios are given in Table 14.
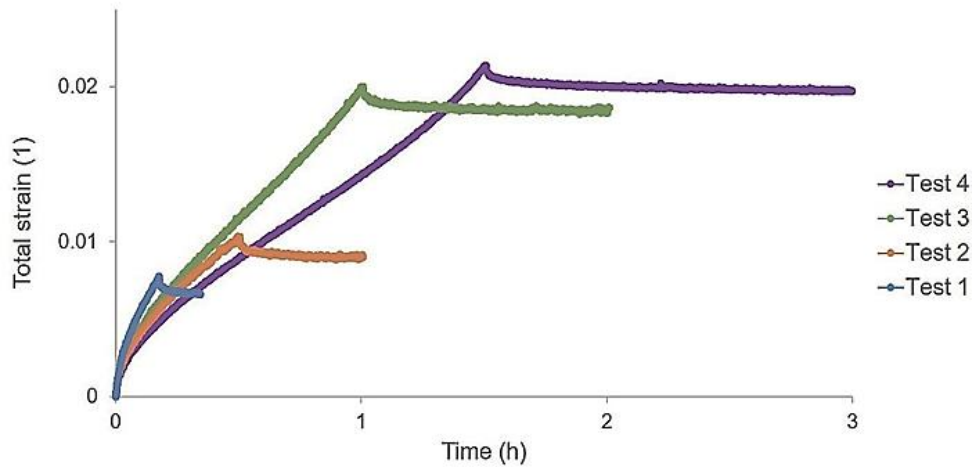
Fig. 33: The first cycle of four tests loaded to 5 MPa and unloaded to 0.1 MPa with different l/u holding times.

Table 14: Creep and recovery and recovery ratios calculated from tests 1- 4 for the first cycle.

	$\varepsilon_t(10^{-3})$	$\varepsilon_{cr}(10^{-3})$	$\varepsilon_{t,R}(10^{-3})$	$\varepsilon_{cr,R}(10^{-3})$	$R_E(\%)$	$R_t(\%)$	$R_{cr}(\%)$
Test 1	7.66	7.59	1.07	1.01	0.93	13.96	13.30
Test 2	10.26	10.19	1.29	1.22	0.69	12.57	11.97
Test 3	19.98	19.91	1.35	1.28	0.35	6.75	6.42
Test 4	21.36	21.29	1.57	1.50	0.33	7.35	7.04

Table 14 shows the effect of holding time on recovered strains ($\varepsilon_{t,R}$ and $\varepsilon_{cr,R}$). The total strain ε_t increased with an increase in holding times from 30 to 60 minutes (tests 2 and 3). Test 4, with the highest total strain during loading, represents the highest strain recovery. However, with longer holding times, the strain recovery ratios were found to decrease. The opposite tendency between tests 3 and 4 regarding R_{cr} is probably dedicated to material heterogeneity [113,123].

Under a constant load of 5 MPa, a standard compressive creep test was carried out at 1300 °C until the final fracture occurred. by comparing it with tests 1-4 (Fig. 34), It was observed that the total creep strain for all cases was quite similar and in the range of 0.34-0.42. In the current investigation, the compressive creep test showed the shortest and test 2 with 30 minutes holding time the longest total creep time. Overall, the exposure to 5 MPa was longer for the l/u tests than for the standard test. This is dedicated to the fact that higher creep strains with lower creep strain rates occur in the secondary creep stage compared to the test with monotonic loading.
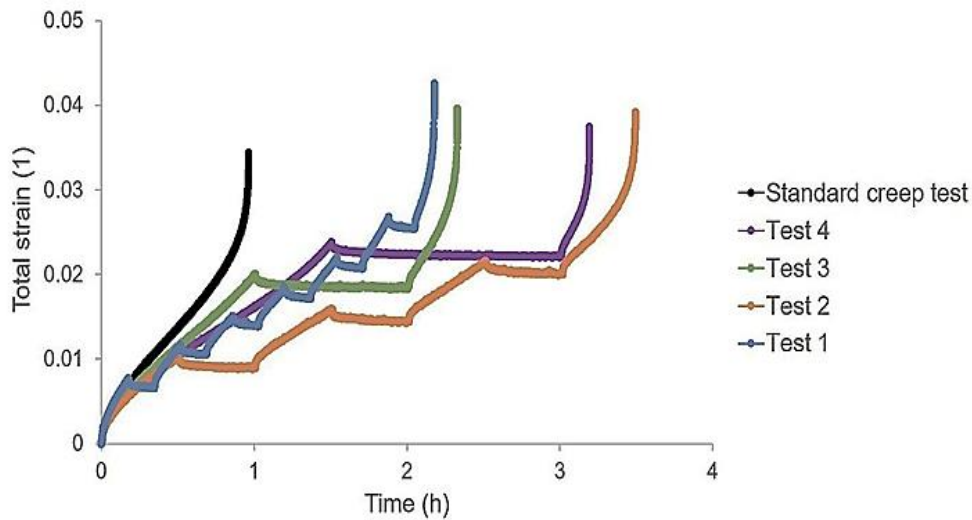
Fig. 34: Comparison of l/u creep tests with different holding times and the standard compressive creep test under a 5 MPa loading stress at 1300 °C.

Table 15: Total strain and test duration for Tests 1-4 and standard compressive creep test.

	ε_t (10^{-3})	Total loading time (h)
Standard creep test	34.12	0.92
Test 1	42.35	2.17
Test 2	39.25	2.33
Test 3	37.62	3.19
Test 4	38.34	3.49

The recovered strain reduces the total creep strain for the l/u creep tests at the end of the cycle. The l/u tests showed a longer overall loading time than sat 5 MPa (Fig. 34). In Fig. 35, only the strains from the 5 MPa loading periods are plotted. This means that recovery phases and recovered strains are excluded. A possible explanation for the higher total strain in comparison to the standard creep tests could be that recovery mechanisms increase the duration of the secondary creep stage in further 5 MPa loading periods.
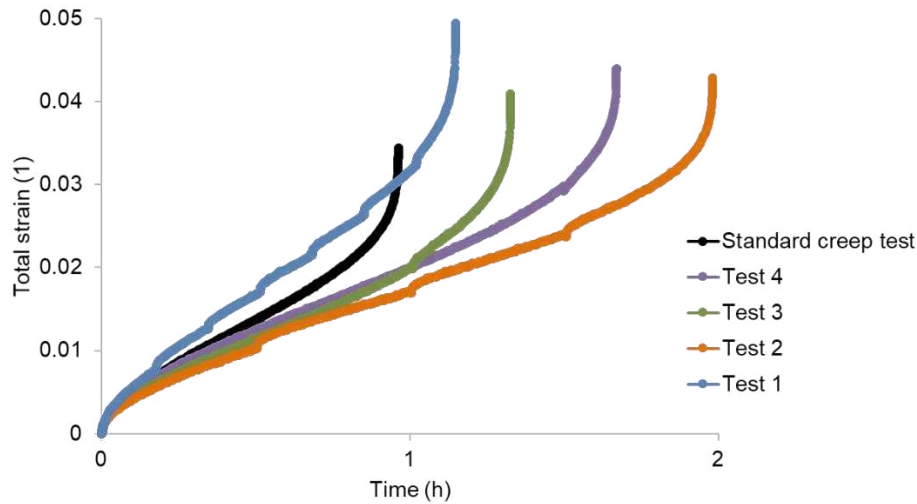
Fig. 35: l/u creep test strains during 5 MPa loading standard compressive creep test under 5 MPa at 1300 °C.

It is believed that as creep strain increases, internal stress and creep strain recovery increase as well. However, in tests 1 and 2, it was found that while creep strain was less in the second and third cycles than in the first, there was a greater creep strain recovery in the second and third cycles than in the first cycle. Test 5 was carried out to clarify the relationship between holding time, internal stress, and creep strain recovery with a holding time of 30 minutes and the recovery phase of its third cycle was continued for approximately 6 h (Fig. 36).
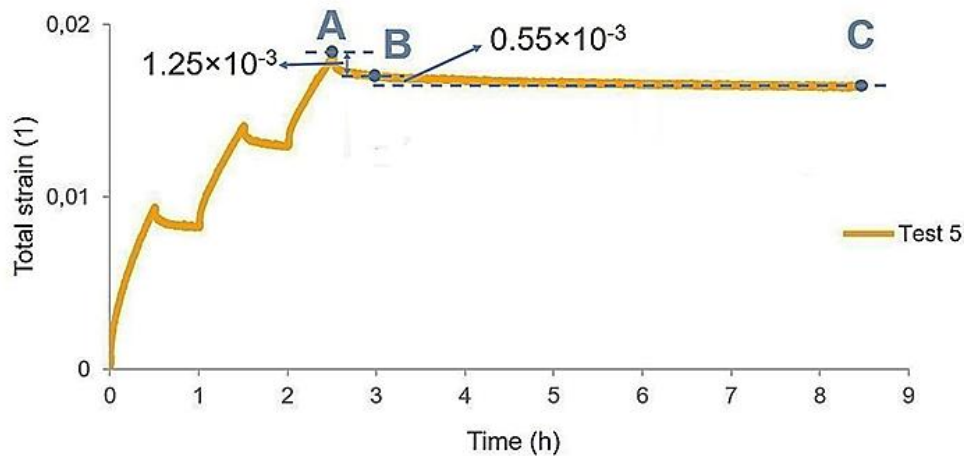
Fig. 36: Creep recovery behaviour (test 5) with 5 MPa loading stress and 0.1 MPa unloading stress, 30 minutes l/u holding time and 6 h holding time in the 3rd cycle.

Table 16: Creep and recovery strain and recovery ratios calculated from test 5.

Cycle	$\varepsilon_t(10^{-3})$	$\varepsilon_{cr}(10^{-3})$	$\varepsilon_{t,R}(10^{-3})$	$\varepsilon_{cr,R}(10^{-3})$	$R_E(\%)$	$R_t(\%)$	$R_{cr}(\%)$
1	9.40	9.33	1.15	1.12	0.75	12.23	12
2	5.93	5.85	1.19	1.15	1.2	20.06	19.65

3	5.24	5.16	1.25	1.18	1.36	23.85	22.86

Similar to test 2, creep strain recovery increases cycle by cycle (Table 16). From A to C, the total strain recovery was $1.8 \cdot 10^{-3}$. The recovered strain during the 30 minutes in the third cycle (from A to B) was $1.25 \cdot 10^{-3}$ and from B to C it was $0.55 \cdot 10^{-3}$. The mean strain rate in the first (2.5-3.5 h) and last (7.5-8.5 h) of the strain recovery was 0.14%/h and 0.02%/h, respectively. During the initial phase of strain recovery (from A to B), roughly 69% of the strain was recovered. It can be concluded that during the first cycles of tests 1 and 2 in the load reduction condition, residual internal stress caused incomplete strain recovery. Because of this, even though there was more creep strain in the first cycle, there was residual internal stress present in the second cycle, which caused a higher strain recovery. Test 6 (Fig. 37) was similar to test 5, with the exception that 2 MPa of unloading stress rather than 0.1 MPa was maintained. After the third loading cycle, this unloading stress was applied for roughly 7 h.
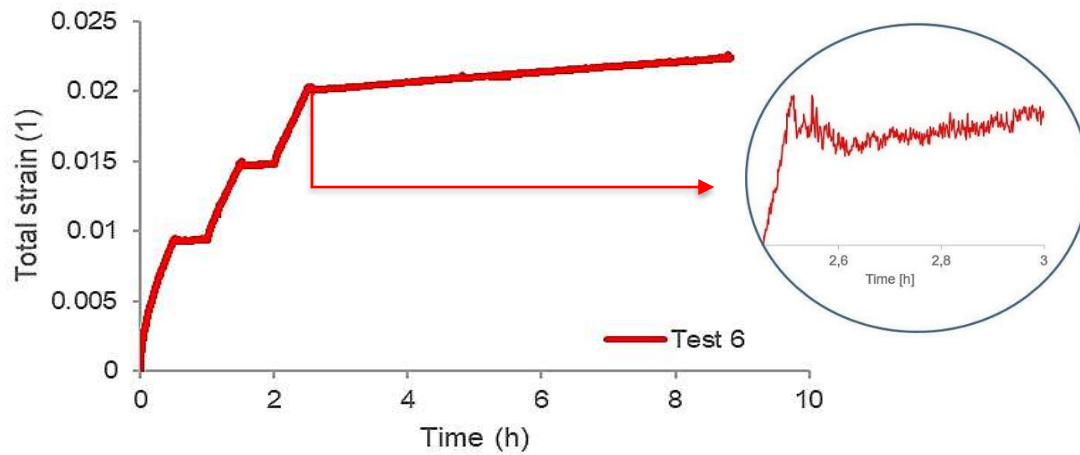
Fig. 37: Creep recovery behaviour (test 6) with 5 MPa load stress and 2 MPa stress, 30 minutes l/u holding time and 7 h final holding time in the 3rd cycle.

Unlike other tests, the creep strain recovery decreased cycle by cycle for test 6. Table 17 demonstrates the measurements and calculations. Additionally, during a short unloading phase, the internal stress reached 2 MPa. As shown in Fig. 37, the creep strain increased again after a recovery period of approximately 6 minutes during the third cycle.

Table 17: Creep and recovery strain and recovery ratios calculated from test 6.

Cycle	$\varepsilon_t(10^{-3})$	$\varepsilon_{cr}(10^{-3})$	$\varepsilon_{t,R}(10^{-3})$	$\varepsilon_{cr,R}(10^{-3})$	$R_E(\%)$	$R_t(\%)$	$R_{cr}(\%)$
1	9.48	9.4	0.28	0.26	0.75	2.95	2.76
2	5.68	5.61	0.25	0.23	1.25	4.4	4.09
3	5.51	5.44	0.22	0.21	1.29	3.99	3.86

After the load was lowered to 2 MPa, the generated internal stress was released during each cycle of test 6 (after 9, 11 and 6 minutes for the first, second and third cycles). It can be assumed that during the recovery phase of each cycle, the internal stress was slightly higher than the load on the sample (2 MPa); therefore, a few minutes after load reduction, the internal stress was smaller than the applied load, leading to the occurrence of further creep.

To compare the effects after load reduction, three l/u creep tests with identical holding times but different stress after stress reduction were performed (Fig. 38). For this purpose, test 7 with 30 minutes holding time at 5 MPa was performed. After half an hour the load was reduced to 4 MPa.
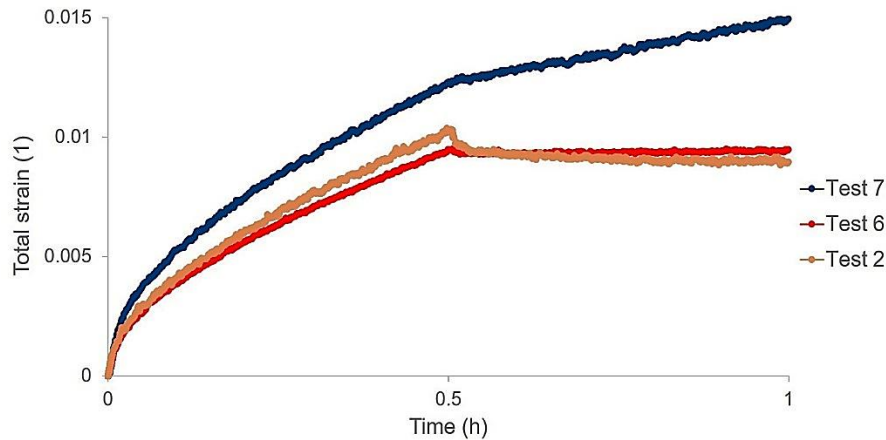
Fig. 38: The first cycle of tests numbers 2, 6, and 7 with 5 MPa load and l/u holding time (30 minutes) with different unloading stresses (0.1, 2, and 4 MPa).

Test 7 showed a higher total creep strain due to the scattering of the material properties, even though all tests had the same conditions for the first 30 minutes. Nevertheless, the impact of stress reduction on the strain recovery ratios could be investigated in this case. Table 18 presents the measurements and calculations for tests 2, 6, and 7.

Table 18: Creep and recovery strain as well as recovery ratios calculated from tests 2, 6, and 7.

	$\varepsilon_t(10^{-3})$	$\varepsilon_{cr}(10^{-3})$	$\varepsilon_{t,R}(10^{-3})$	$\varepsilon_{cr,R}(10^{-3})$	$R_E(\%)$	$R_t(\%)$	$R_{cr}(\%)$
Test 2	10.26	10.19	1.29	1.22	0.69	12.62	12.03
Test 6	9.48	9.4	0.28	0.26	0.75	2.95	2.76
Test 7	12.28	12.21	-	-	-	-	-

Test 2 showed that the magnitude of the internal stress was higher than the applied load on the sample (i.e., 0.1 MPa); hence, reduction in load from 5 to 0.1 MPa caused creep strain recovery [125]. For test 6, it was assumed that the internal stress would be slightly higher than the applied load on the specimen. (i.e., 2 MPa); hence, creep strain recovery was determined for 6 minutes. Note that, the strain rate in the final recovery phase did not change and remained constant over time for tests 2 and 6. The difference between the applied load on the sample and the internal stress causes secondary creep, as represented by test 7 [125], which demonstrated a strain that

increased with time when the applied load was decreased from 5 to 4 MPa. From this behaviour, it can be concluded that the magnitude of the internal stress was smaller than the unloading stress (i.e., 4 MPa), and hence, strain recovery did not occur. Based on the results, the following was concluded:

- If the applied load (and maintained) on the sample during the unloading phase is higher than the internal stress, then the creep strain increases monotonically with time [125].

- If the applied load on the sample equals the internal stress, then the elastic strain decreases because of the load reduction and the creep strain remains constant until the internal stress becomes smaller than the applied load [125].

- If the applied load on the sample is smaller than the internal stress, then the elastic strain decreases because of the load reduction and the creep strain also gradually decreases with time owing to strain recovery [125].

5 MODELING OF THE CREEP STRAIN RECOVERY

5.1 Burger's model

Burger's model takes into account both the elastic and viscous aspects of a material's response. It is employed to forecast the creep and recovery characteristics of materials exposed to loading conditions that vary with time [94]. In this study, Burger's parameters (E_M, E_K, η_M, η_K) were determined with an in-house developed MATLAB code. Lsqurvefit fit function [68] was applied to fit the curve and determine the parameters for Eq. 27. Starting values are given for Burger's model parameters and the applied stress, reduction stress, and time at the moment of unloading are defined. The parameter identification was performed for each l/u test individually. Below, an example of the one parameter set for an inverse evaluation is shown. As an example, initial values and loads, as well as t_1 (holding time) are given in Table 19:

Table 19: An example of initial parameters given for the determination of Burger's parameters (Test 1).

E_M	0.2
η_M	0.02
E_K	0.1
η_k	0.01
Stress during loading (MPa)	5
Stress during unloading (MPa)	0.1
t_1 (s)	600

Determined Burger's parameters for the first cycle of tests 1-4 can be seen in Table 20. For tests 1-3, the fit of the experimental curves was better than for the test 4. For test 4 with 90 minutes of holding time, the deviation between the fit and experimental curve is clearly due to the creep stage change from the second to the third stage.

Table 20: Burger's model parameters are identified with an inverse evaluation procedure.

Test	E_M(MPa)	η_M(MPa.s)	E_K(MPa)	η_M(MPa.s)
1	1.15E+05	6.80E+05	1.62E+02	2.11E+03
2	4,10E+04	1.21E+06	1.85E+02	2.17E+03
3	1.64E+05	1.10E+06	1.61E+02	2.66E+03
4	4.24E+04	1.40E+06	3.27E+02	17.96E+03

Figs. 39, 40 shows the fit of the tests 1-4 with the parameters given in Table 20. To fit the creep recovery behaviour using Burger's model, the unloading time must be known as input in the inverse evaluation MATLAB code. However, for refractories in service, the stress history is not clear, and this is a disadvantage for the application of this model for the simulation of refractory lining behaviour under the l/u condition.
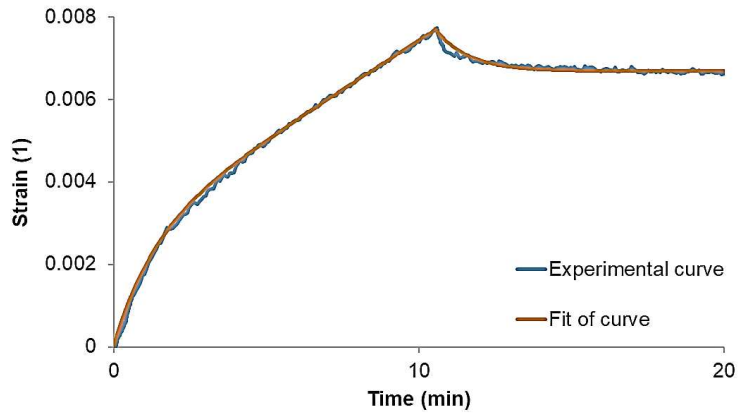
(1)
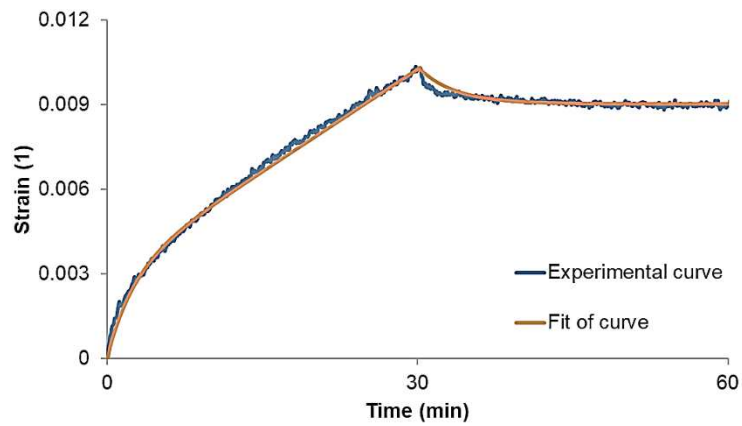
(2)

Fig. 39: Fit of experimental l/u tests 1 and 2 with different holding times using Burger's model for the first loading cycle.
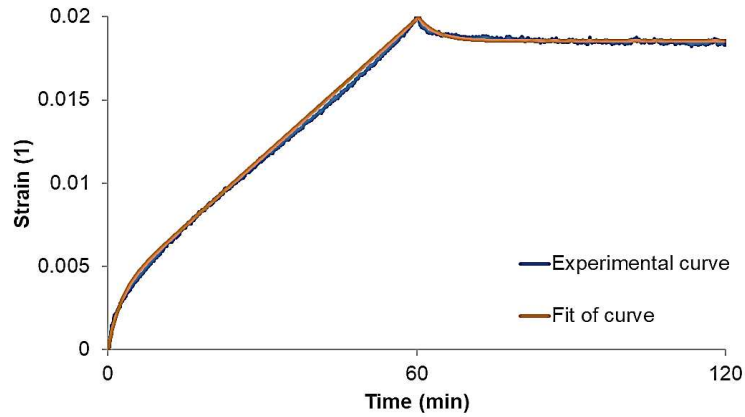
(3)
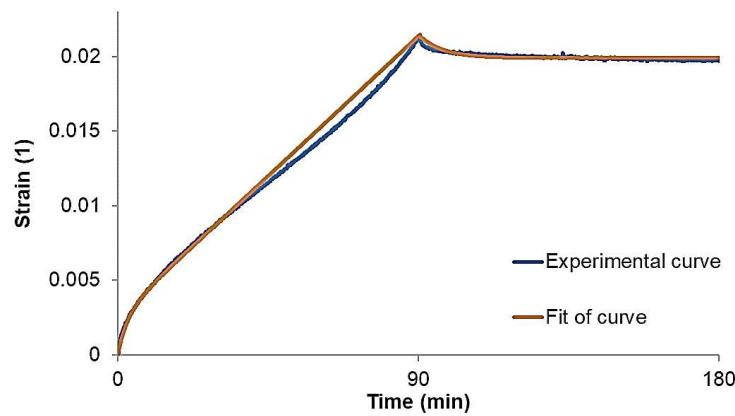
(4)

Fig. 40: Fit of experimental l/u tests 3 and 4 with different holding times using Burger's model for the first loading cycle.

5.2 Prony series

A further frequently applied possibility for the simulation of creep recovery behaviour is modelling viscoelastic behaviour with Prony series parameters, which is a set of Maxwell elements in series and adding a spring in parallel [98,99]. In the commercial FE code ABAQUS, viscoelastic material behaviour can be simulated by a Prony series expansion of the dimensionless relaxation modulus. Therefore, relaxation shear modulus (the Prony series parameters) must be determined. Shear relaxation modulus can be expressed as Prony series in ABAQUS (Eqs. 38-40) [109]:

$$G_{(t)} = G_\infty + \sum_{i=1}^{N} G_i e^{\frac{-t}{\tau_i}}$$

(38

G_∞ is the steady-state stiffness (represented by the parallel spring), G_i, τ_i are the time constants and represented by the stiffness of the Maxwell elements, and t is the time. These parameters define the material behaviour. For n=2:

$$G_{(t)} = G_\infty + G_1 . e^{\frac{-t}{\tau_1}} + G_2 . e^{\frac{-t}{\tau_2}}$$ (39

Finally, by solving the equations:

$$G_{(t)} = G_\infty + G_0 \left(g_1 \, e^{\frac{-t}{\tau_1}} + g_2 . e^{\frac{-t}{\tau_2}} \right)$$ (40

g_1, g_2, τ_1, τ_2 are the parameters applied in ABAQUS to represent the behaviour equivalent to Burger's model [97-100]. g_1 g_2 are dimensionless shear modulus and τ_1 τ_2 are the relaxation time (s). Burger's model parameters were determined using the open-source software DAKOTA [126]. For this purpose, a creep recovery simulation of tests 1-4 was carried out with ABAQUS on a simple 3D model (Fig. 41) (C3D8, 8-node linear brick). Boundary conditions were defined for uniaxial loads. Table 21 presents an illustrative instance of test 1, employing 10 minutes of holding time. The load applied ranged from 0 to 5 MPa within 35 seconds, after which it was maintained for 10 minutes. Subsequently, the load was reduced to 0.1 MPa, which also took 35 seconds.

Table 21: L/u condition for test 1 with 10 minutes holding time.

Time (s)	0	35	600	635	1200
Load (MPa)	0	5	5	0.1	0.1
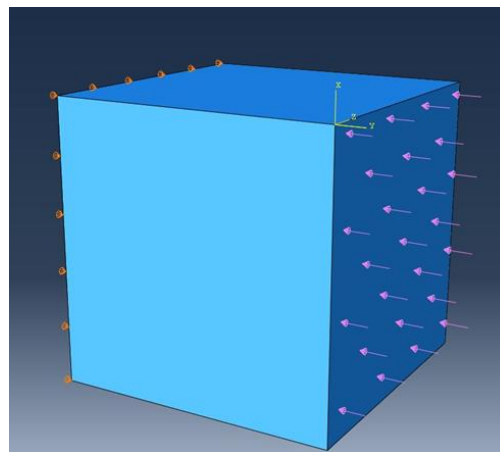
Fig. 41: Simulation model with boundary conditions.

For the input data, the result from the simulation (strain-time data) was used for the optimization in DAKOTA. The minimization algorithm NL2SOL was applied. Prony parameters were determined by minimizing the difference between the experimental and the simulated curves. The first cycle of each test (1-4) was assessed, and the extracted parameters were applied for simulations in ABAQUS (Figs. 42,43). The table below presents the determined Prony parameters (Table 22).

Table 22: Prony parameters determined with the inverse evaluation.

Test	g_1	g_2	τ_1 (s)	τ_2 (s)
1	0.0099	0.99	333	1.61
2	0.012	0.98	636	1.97
3	0.0099	0.99	722	2.62
4	0.0198	0.98	507	2.79
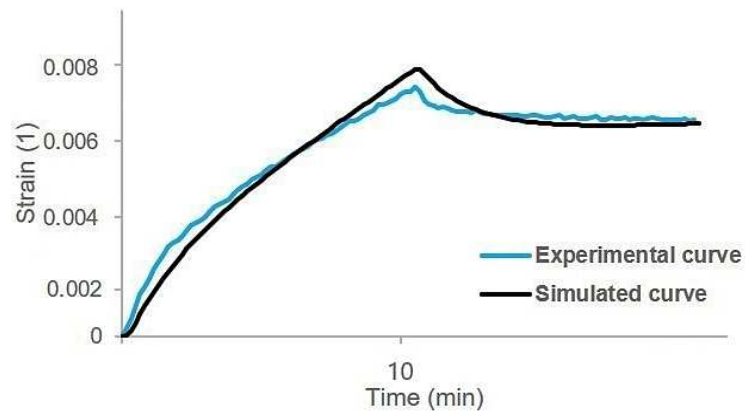
(1)
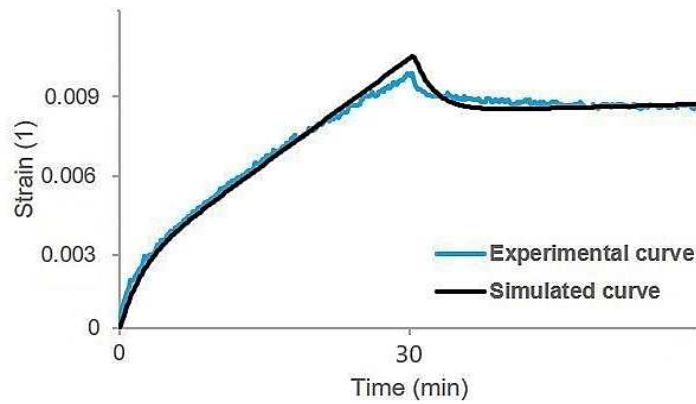
(2)

Fig. 42: Comparison of experimental and simulated curves for the loading conditions of tests 1 and 2.
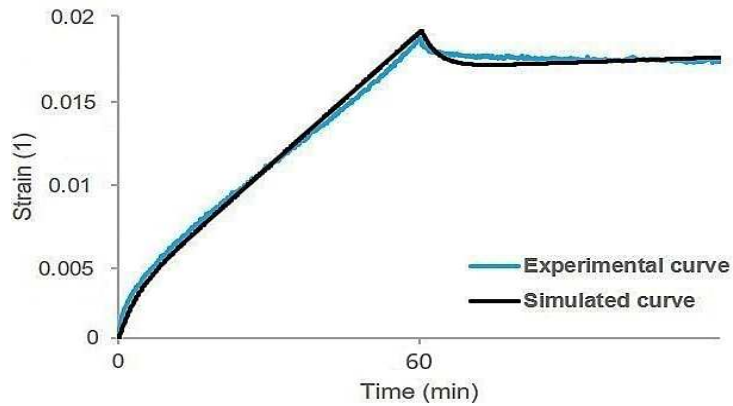
(3)
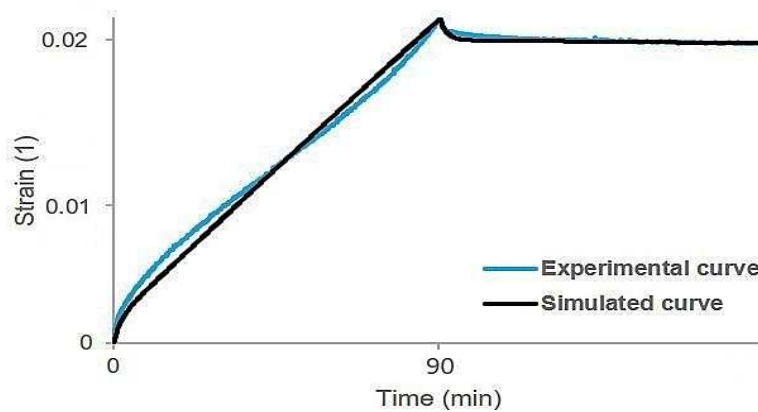
(4)

Fig. 43: Comparison of experimental and simulated curves for the loading conditions of tests 3 and 4.

Burger's model and Prony series showed an acceptable fit to the experimental curve. However, comparing the residuals (Table 23) of fits for Burger's model and Prony series using Eq. 37 with the same data points for each curve (1800 data points) (Figs. 39,40 and Figs. 42,43), represented that Burger's model was able to fit better than the simulation with Prony series parameters for tests 2 and 4.

Table 23: Residual of fits using Burge's model and Prony series (DAKOTA) for tests 1-4.

	Test 1	Test 2	Test 3	Test 4
Burger's model	1.89E-04	1.67E-05	1.52E-04	2.06E-04
Prony series	9.93E-05	5.93E-05	7.46E-05	6.58E-04

Fig. 44 presents the simulation results for tests 1 and 2 conditions with 10 and 30 minutes holding times. The fits are a result of inverse evaluations, only the first cycle was considered for parameter identification. Furthermore, simulations were carried out with parameters determined from the first two and three cycles. It is seen that the deviation between the experimental curves and the simulated ones increases with the cycles. Results indicated that using the Prony parameters for

the first cycle showed an acceptable fit for the first cycle of the experimental curve, however, for the following cycles the deviation increased. Simulations with parameters determined by two and three cycles showed a smaller deviation for the experimental curve in comparison to the simulation with the first cycle parameters.
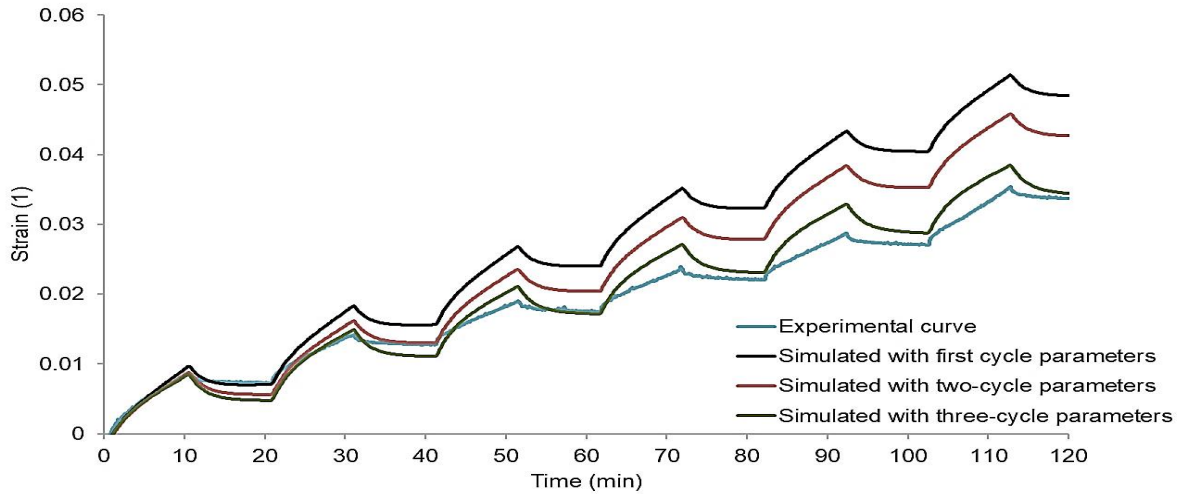
(1)
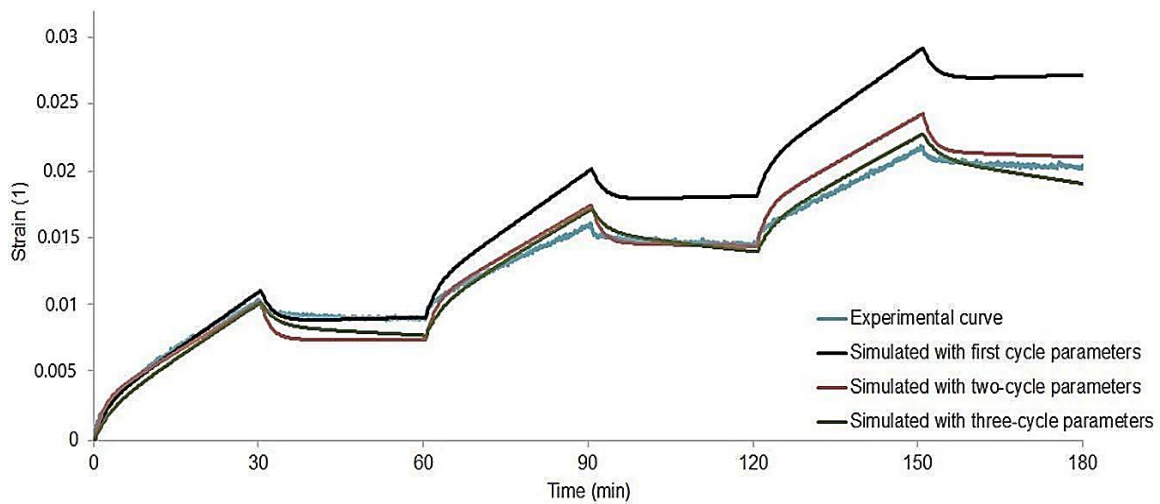
(2)

Fig. 44: Simulation results for tests 1 and 2 conditions with Prony series parameters determined from different cycles and comparison with the experimental curves.

Table 24: Prony series parameters determined with DAKOTA with different cycles as input data (test 1: 10 minutes).

Cycle	g_1	g_2	τ_1	τ_2
1	0.0099	0.99	333.76	1.61
2	0.0099	0.99	432.82	1.73
3	0.0098	0.99	478.68	1.47

Table 25: Prony series parameters determined with DAKOTA with different cycles as input data (test 2: 30 minutes).

Cycle	g_1	g_2	τ_1	τ_2
1	0.0129	0.98	636.82	1.97
2	0.0128	0.98	793.64	1.42
3	0.0129	0.98	518.99	2.86

Simulation with Burger's model and the Prony series showed different drawbacks. They can reasonably approximate the creep and recovery behaviour under given constant loads, but the load dependency is not covered by the models. Because of the permanently changing loads in refractory linings, these models cannot simulate the in-service behaviour.

5.3 Chaboche model

Finally, the Chaboche model was used to fit the experimental curves using Eq. 33. The material model parameters (Table 26) are determined for each temperature, using user expertise rather than optimization routines. The elastic material response is parameterized in the first step of loading, followed by the determination of approximate hardening parameters for the experimental tests. Cyclic viscoplastic effects are identified through a kink in the mechanical response of the unloading stage and are replicated by scaling kinematic hardening parameters (C_i and γ_i). Dynamic modules (M_i, m_i, K and n) are then implemented to track evolution over time [86,106,112].

Table 26: Parameters for the SF castable (for 1300 °C) identified with the UMAT subroutine.

E (MPa)	v	R_0 (MPa)	K (MPa)	N (MPa)	C_1 (MPa)	γ_1 (MPa)	M_1 (MPa)	m_1 (MPa)	C_2	γ_2	M_2	m_2
70000	0.2	0.2	40	4.6	1000	20	200	2	200	0.3	40	4.8

For the simulations, a single element model as described in section 5.2 was applied. Overall, 12 experimental l/u uniaxial compressive creep tests at 1300 °C were carried out for this purpose. Nine l/u tests were performed with a holding time of 30 minutes and different loads (Table 27). In three more tests, the holding times were 10, 60 and 90 minutes with a load of 5 MPa and complete unloading between the loading periods.

Table 27: Experimental l/u conditions for tests at 1300 °C with 30 minutes holding time.

Test	1	2	3	4	5	6	7	8	9
Load (MPa)	5	5	5	6	6	6	7	7	7
Unload (MPa)	0	1	1.5	0	1	1.5	0	1	1.5

One set of material parameters was used to simulate the compressive l/u creep of the SF castable. Below the results are shown in Figs. 45-47.
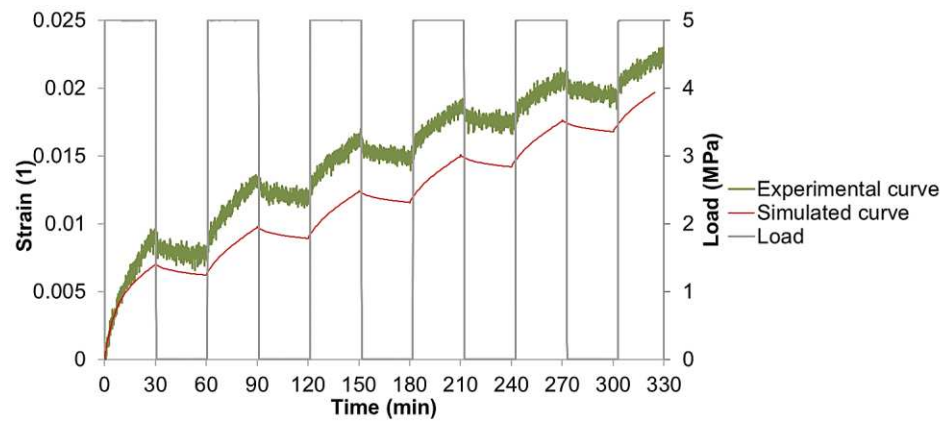
(1)
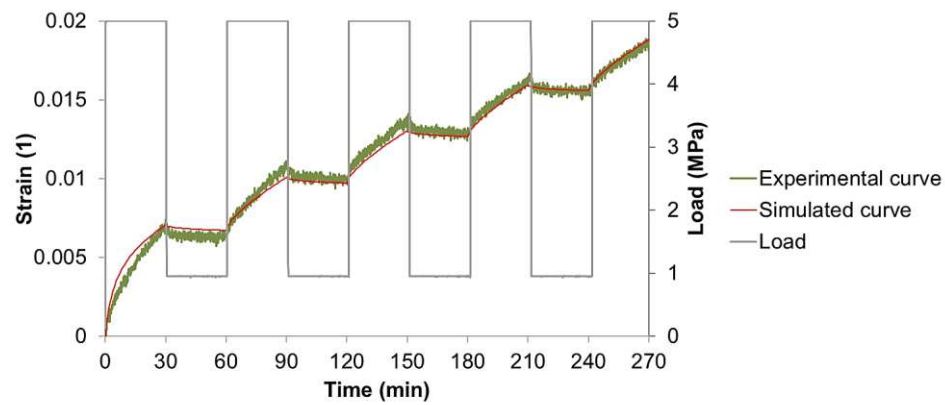
(2)
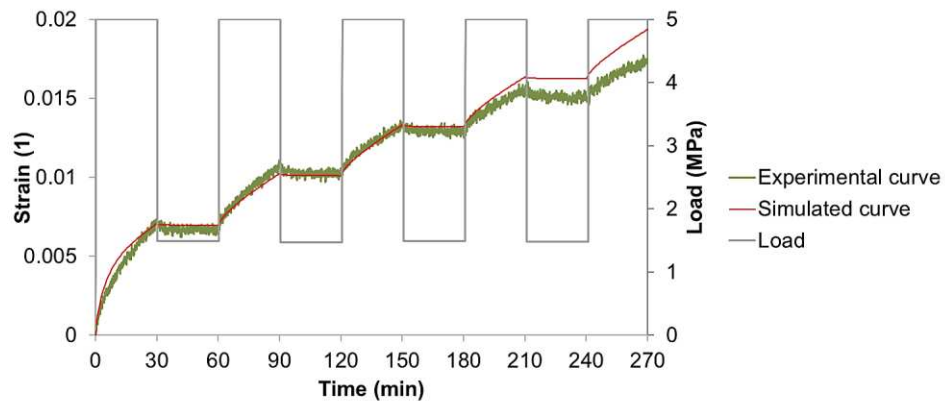
(3)

Fig. 45: Experimental curve fit with the Non-linear kinematic hardening model for tests 1-3 with 30 minutes holding time.
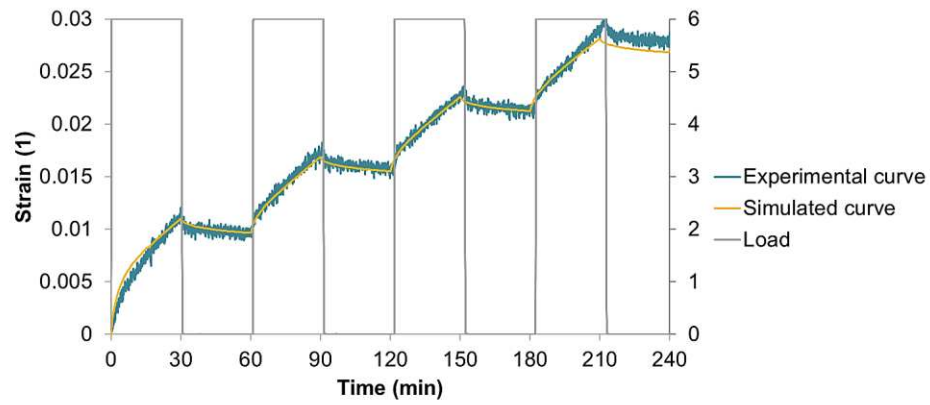
(4)
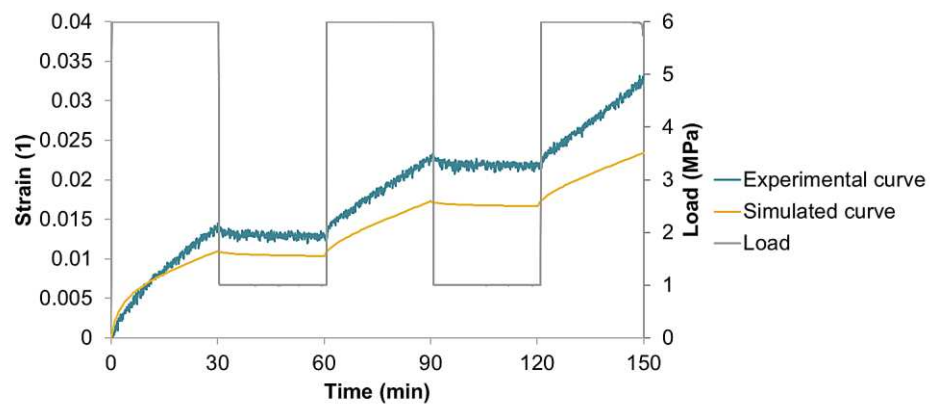
(5)
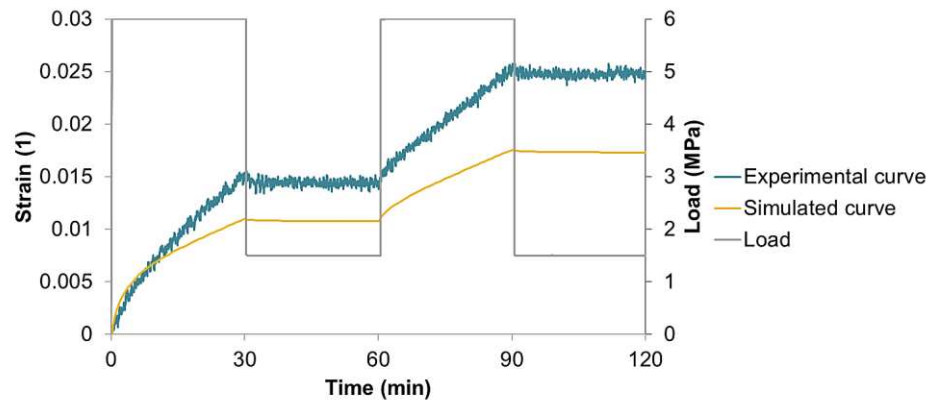
(6)

Fig. 46: Experimental curve fit with the Non-linear kinematic hardening model for tests 4-6 with 30 minutes holding time.
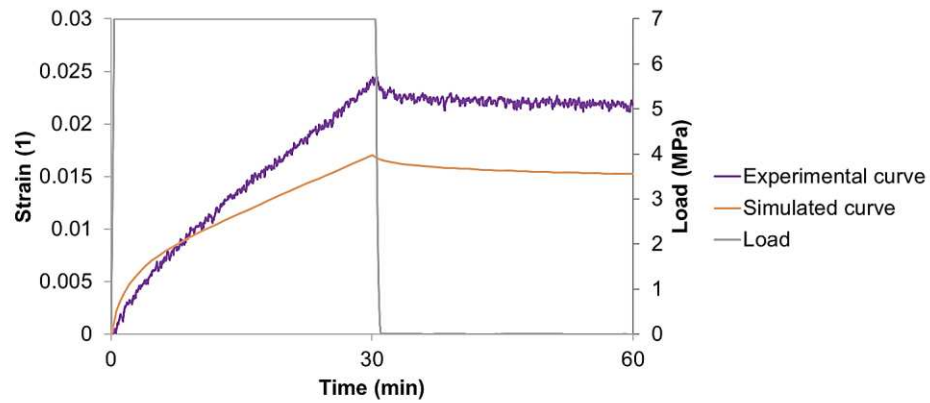
(7)
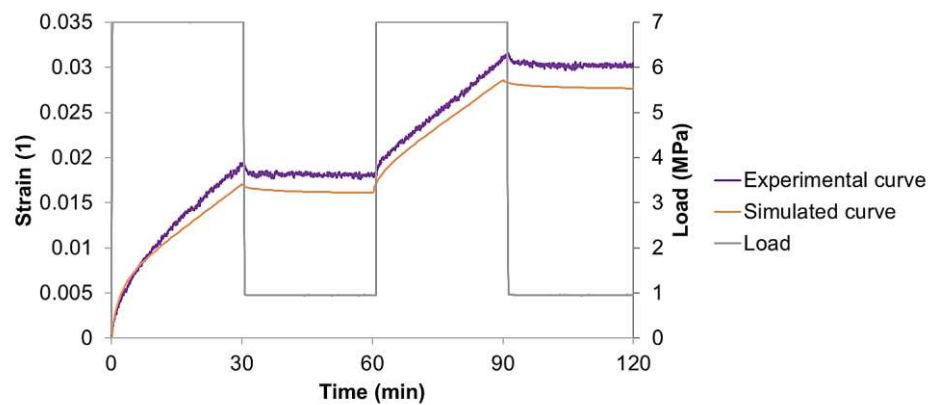
(8)
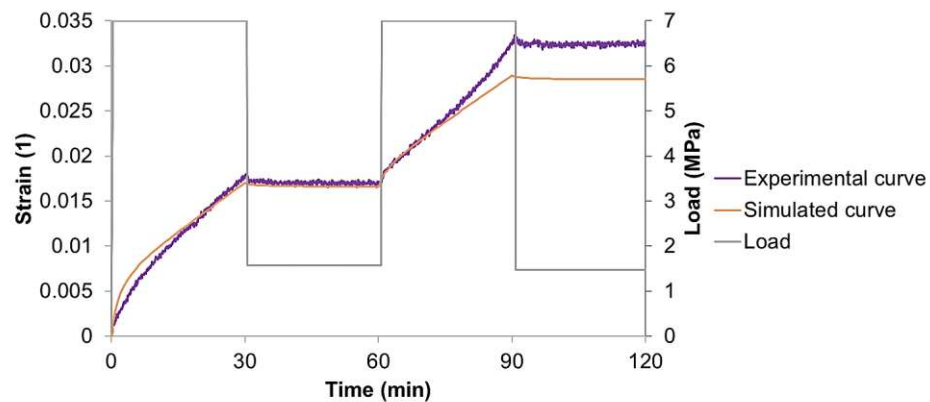
(9)

Fig. 47: Experimental curve fit with the Non-linear kinematic hardening model for tests 7-9 with 30 minutes holding time.

The residual of fitting of tests 1-9 was calculated according to Eq. 37, considering an equal amount of data points for each curve (1800 data points). According to Figs. 45-47, the residual of fitting for the first cycle of tests 2 and 3 is much smaller than for test 1. For test 1, these residual increases from cycle to cycle. Tests 4 and 7 represented the lowest and biggest residual of fitting, respectively. Table 28 shows the residuals for the first cycle of tests 1-9.

Table 28: Residual of fit for the first cycle of tests 1-9.

Test 1	Test 2	Test 3	Test 4	Test 5	Test 6	Test 7	Test 8	Test 9
6.89E-04	2.67E-04	2.12E-04	1.06E-05	3.35E-04	3.87E-04	9.86E-03	3.12E-04	2.73E-04

Material parameters according to Table 26 were applied to fit the experimental l/u tests at 1300 °C with different holding times for the creep and recovery periods. Four tests were selected with 10, 30, 60 and 90 minutes of holding time for the simulation. Results (Figs. 48, 49) illustrated partially unsatisfied fitting of experimental curves. The reasons are not clear at this state of research, and more experiments are necessary. However, in addition to finding local minima in the inverse evaluation process, material inhomogeneity and possibly the partial inadequacy of the material model play a role.
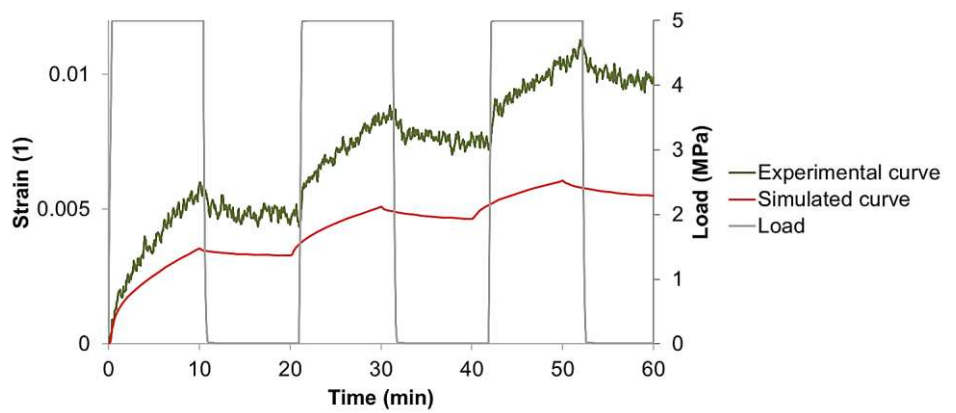
(a)
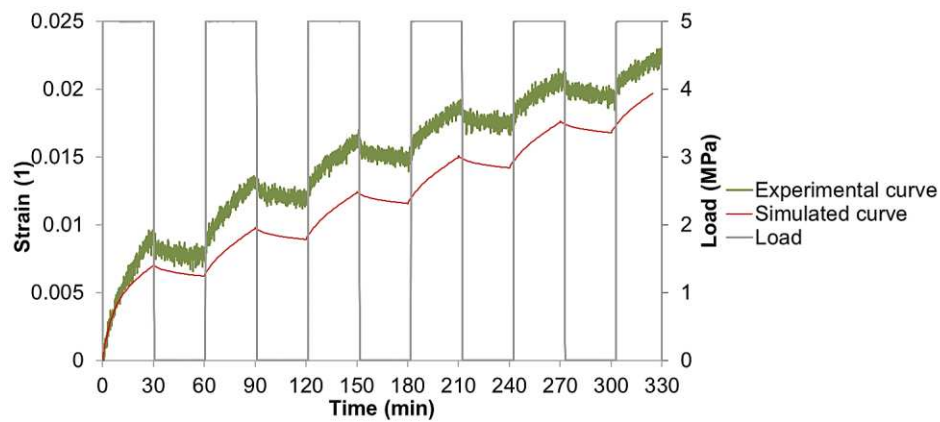
(b)

Fig. 48: Experimental curve fit with the Non-linear kinematic hardening model for tests loaded to 5 MPa and unloaded to 0 MPa for 10 (a) and 30 minutes (b) holding time.
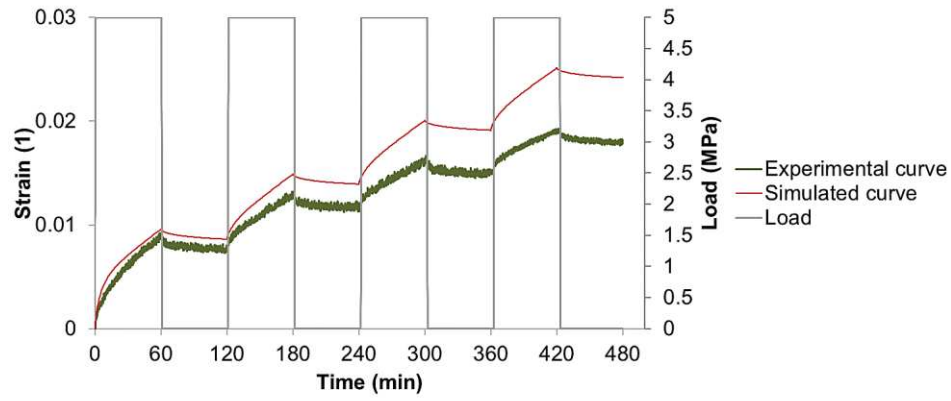
(a)
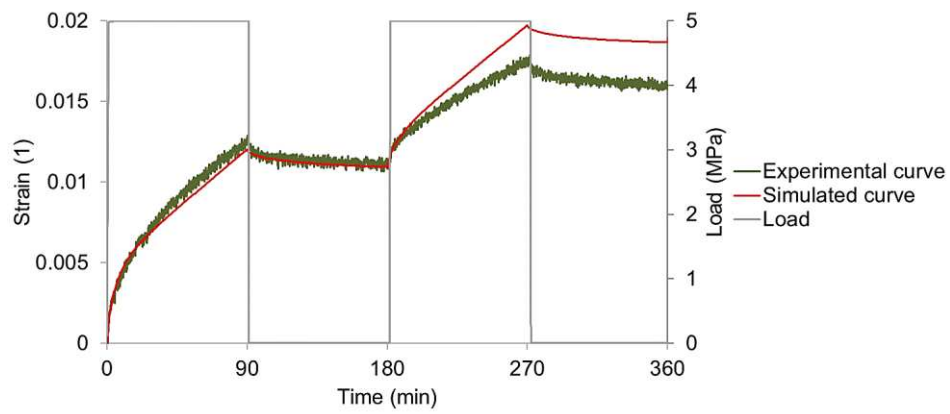
(b)

Fig. 49: Experimental curve fit with the Non-linear kinematic hardening model for tests loaded to 5 MPa and unloaded to 0 MPa for 60 (a) and 90 minutes (b) holding time.

5.4 Comparison of Chaboche Non-linear kinematic hardening model with a Norton-Bailey creep model

Here it is discussed how far the Chaboche model can fit the l/u experimental curves. As the Norton-Bailey model is frequently applied for the simulation of the creep behaviour it is reasonable to check if it is possible to fit the Chaboche curves with Norton-Bailey for monotonic loading. For this purpose, using the Chaboche model and the parameters in Table 26, four curves (Fig. 50) were simulated under constant uniaxial load with ABAQUS.
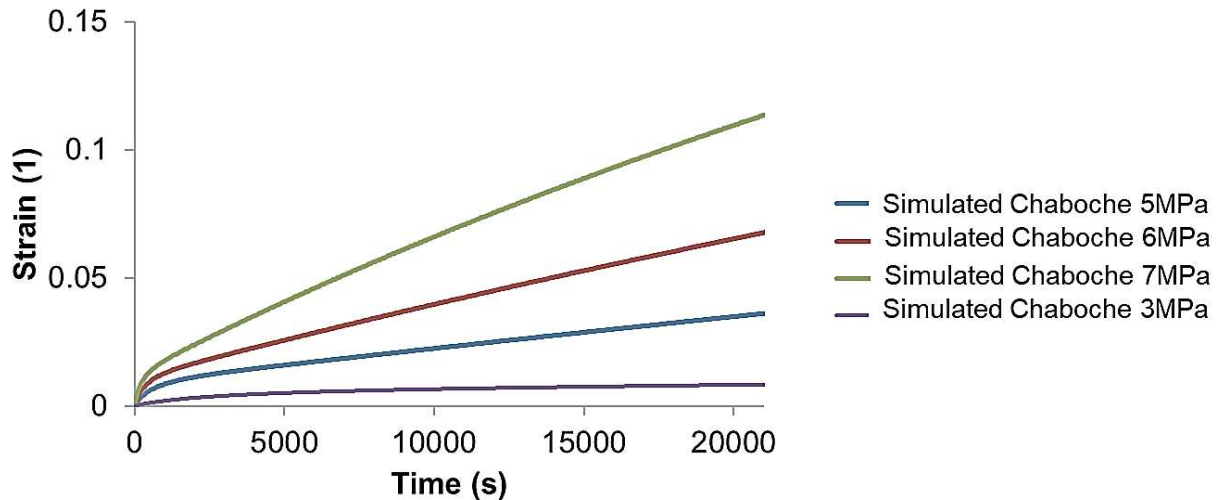
Fig. 50: Results from the Chaboche model under constant uniaxial load.

With an automatic creep stage separation method [71], simulated curves from Fig. 50 were divided into primary and secondary creep stages. The period for the first and second stages is shown in Table 29. Afterwards, the first and second stages were fit with the Norton-Bailey model (Fig. 51, 52) to determine the creep parameters.

Table 29: Time period for the first and second stages for the curves simulated with the Chaboche model.

	Stage 1 (s)	Stage 2 (s)
3MPa	0-10800	10800-15000
5MPa	0-5000	5000-9000
6MPa	0-4500	4500-8100
7MPa	0-2500	2500-6500
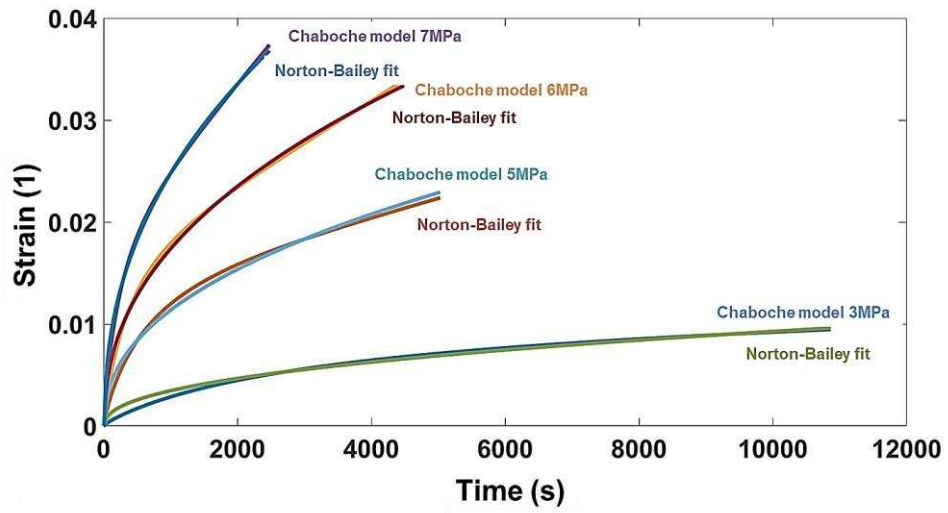
(a)
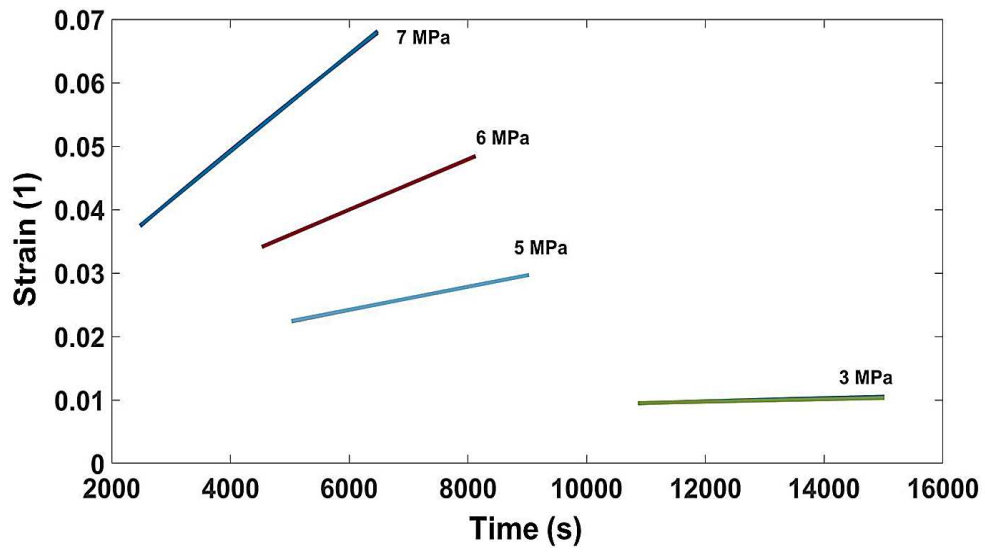
(b)

Fig. 51: Fit of the Chaboche curves with the Norton-Bailey creep model for the first (a) and second (b) creep stages.
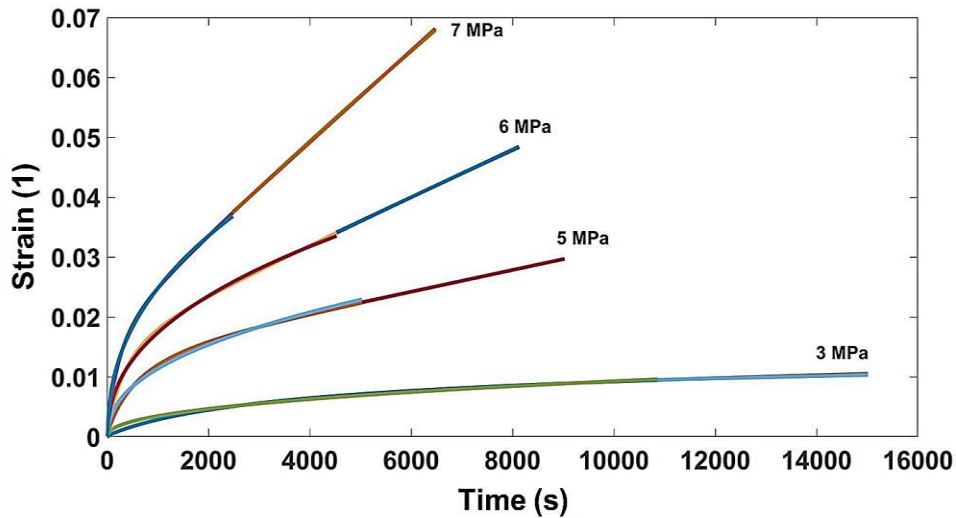
Fig. 52: Fit of the Chaboche curves by the Norton-Bailey creep model for the first and second stages in one plot.

In Fig. 51(a), the first stage was fit, and the residual between the simulated curves was small (Table 30). For the second stage (Fig. 51-b), the fit and the original curve were congruent. Fig. 52 shows the fit of the curves simulated with the Chaboche and Norton-Bailey models for both stages. Below, Norton-Bailey creep parameters, as determined with an inverse evaluation, are shown for the creep stages (Table 31).

Table 30: Residual of fitting the Norton-Bailey creep curve with the Chaboce model for the first stage and different loads.

	3 MPa	5 MPa	6 MPa	7 MPa
Residual of fitting	1.32E-05	1.86E-05	2.12E-05	1.73E-05

Table 31: Norton-Bailey creep parameters for the creep curves plotted by the Chaboche model.

Primary creep stage			Secondary creep stage	
$\log K$	a	n	$\log K$	n
-11.63	-1.30	5.41	-8.75	4.31

After promising results from comparing the Norton-Bailey and Chaboche models, experimental creep curves were fit with the Chaboche model. The first stage of the creep curves was fit by the Chaboche model using one series of parameters for each temperature. The figures below (Figs. 53-55) represent the results.
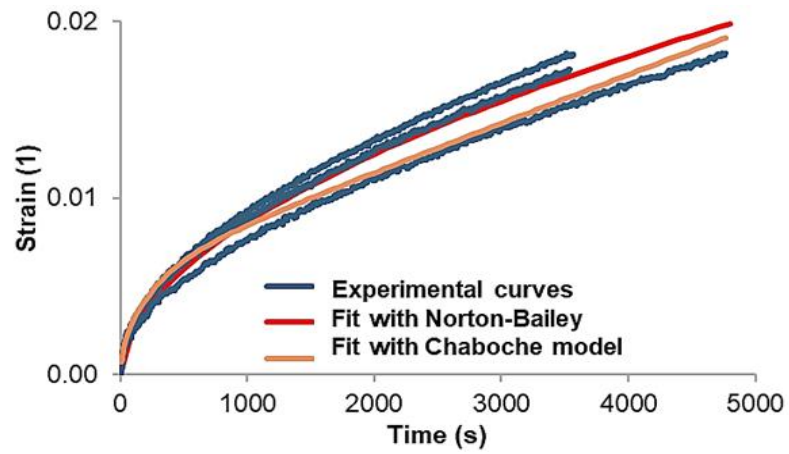
(a)
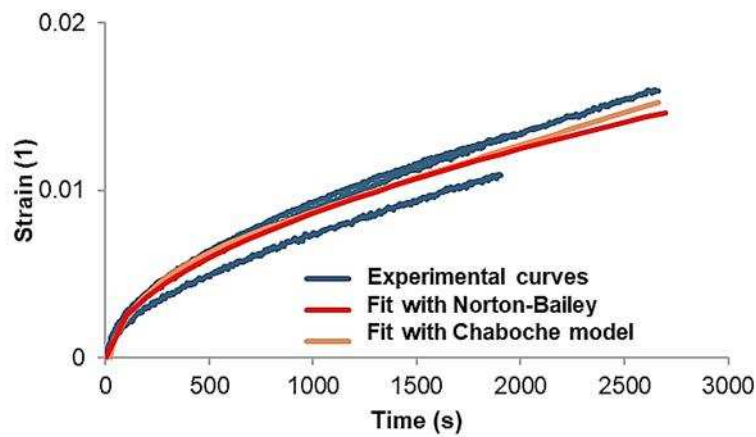
(b)
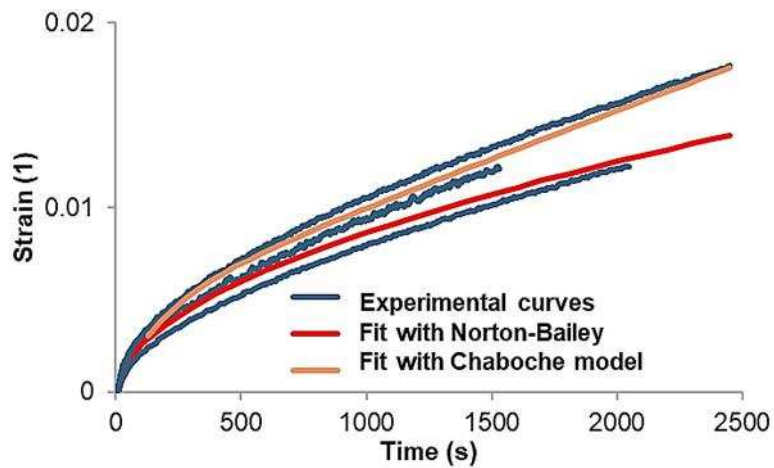
(c)

Fig. 53: Fit of the experimental creep curves (1300 °C) by Norton-Bailey and Chaboche model a:7 MPa, b:7.5 MPa, c: 8 MPa.
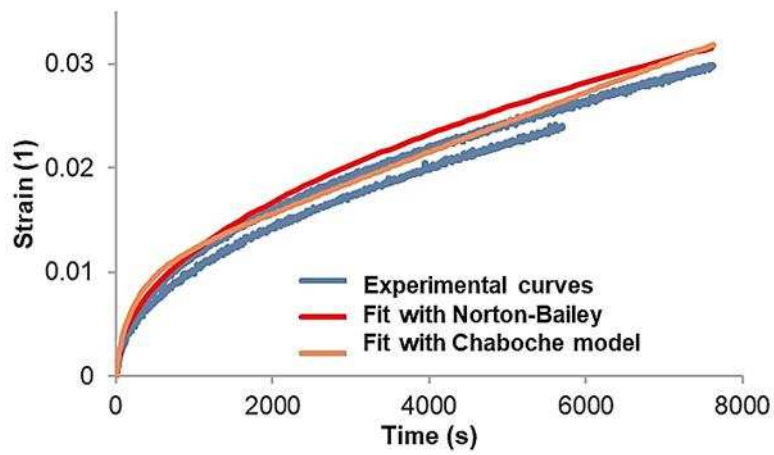
(a)
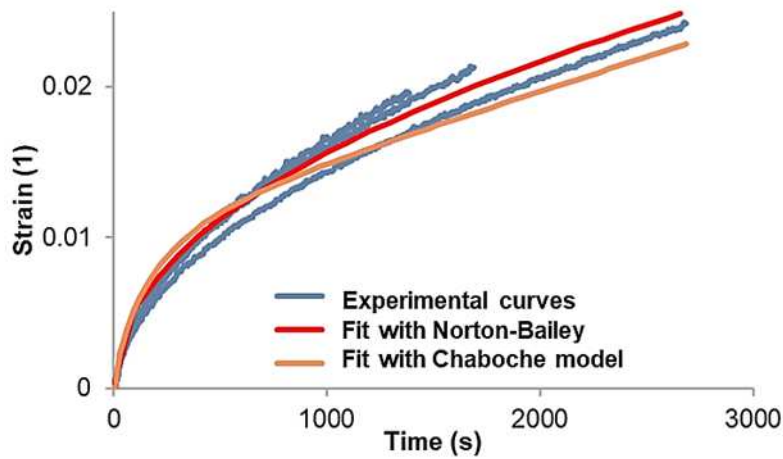
(b)
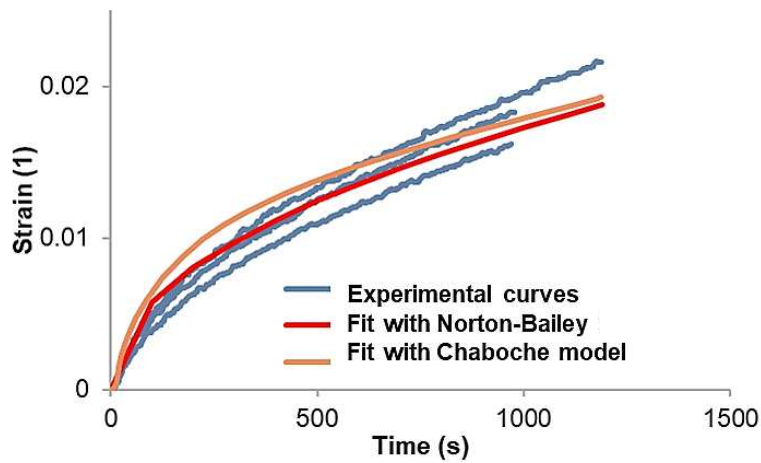
(c)

Fig. 54: Fit of the experimental creep curves (1400 °C) by Norton-Bailey and Chaboche model a:4.5 MPa, b:5 MPa, c: 5.5 MPa.
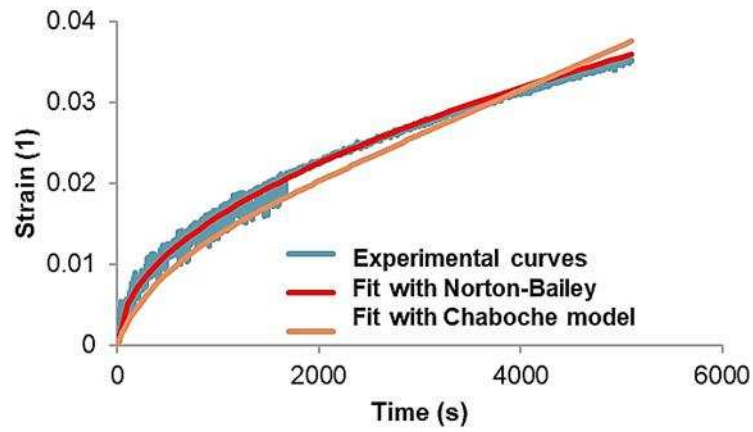
(a)
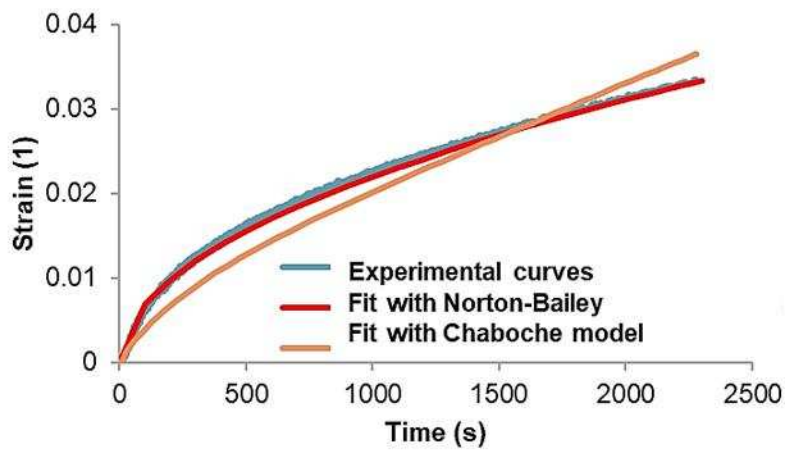
(b)
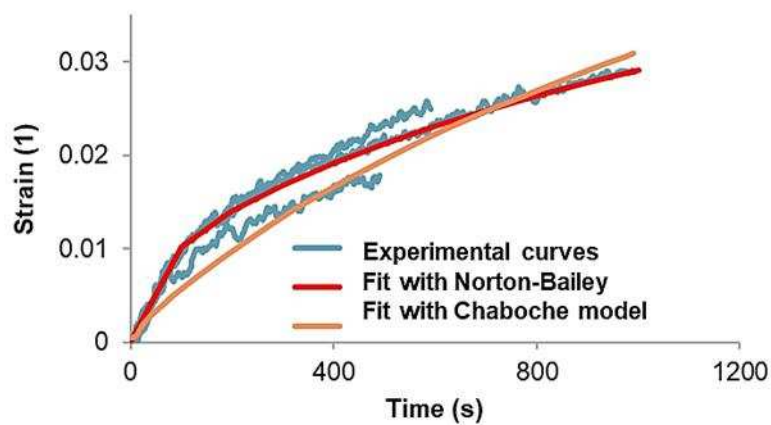
(c)

Fig. 55: Fit of the experimental creep curves (1500 °C) by Norton-Bailey and Chaboche model a:3 MPa, b:3.5 MPa, c: 3.75 MPa.

Fig. 53 shows the fit of the experimental creep curves for 1300 °C for three different loads and the first stage. For both models, only one series of parameters was applied. The residuals for fits with the Chaboche and the Norton-Bailey model are close to each other (using Eq. 37 with considering the same amount of data points). For 8 MPa, the Chaboche curve showed a more significant deviation from the Norton-Bailey curve than for the other tests. Table 32 shows the average fit residual for different models at three temperatures. At 1400 °C, the Norton-Bailey model represented a better fit as the Chaboche model (Fig. 54). At 1500 °C (Fig. 55), the result determined by Norton-Bailey showed better fitting than the Chaboche model according to the residuals (Table 32).

Table 32: Average fit residuals with Norton-Bailey and Chaboche models for different temperatures.

	1300 °C	1400 °C	1500 °C
Norton-Bailey 9-combination	2.32E-04	1.75E-04	2.82E-04
Chaboche model	2.85E-04	2.31E-04	4.85E-02

Table 33 shows the Chaboche model parameters utilized for fitting the experimental creep curves for the first stage. The results indicated that for different temperatures, mainly viscoelastic parameters (k, n), second kinematic hardening parameters (C_2, γ_2) and second static recovery parameters (M_2, m_2) are the main influencing factors.

Table 33: Chaboche model parameters for the fit of experimental creep curves (1300 °C: a, 1400 °C: b and 1500 °C: c).

E	v	R_0	K	n	C_1	γ_1	M_1	m_1	C_2	γ_2	M_2	m_2
70000	0.2	0.2	42	5.2	1000	20	200	2	400	0.5	40	4.8

(a)

E	v	R_0	K	n	C_1	γ_1	M_1	m_1	C_2	γ_2	M_2	m_2
70000	0.2	0.2	32	3.9	1000	20	200	2	230	0.3	36	4.9

(b)

E	v	R_0	K	n	C_1	γ_1	M_1	m_1	C_2	γ_2	M_2	m_2
70000	0.2	0.2	35	3.5	1000	20	200	2	310	0.1	46	3.8

(c)

6 SUMMARY

This research aimed to characterise and simulate the compressive creep behaviour of refractory castables under constant loads and l/u conditions. The goal was achieved by conducting creep tests and further material characterisation (e.g. RFDA, XRD, SEM), as well as analysis of the results. Finally, an extended nonlinear kinematic hardening model was applied to simulate the creep recovery of the SF castable. The main conclusions of this study are:

- In the SF castable spinel and CA_6 are forming at a temperature above 1000 °C during the sintering process and cause a volume expansion. This expansion leads to microcrack formation and reduces the mechanical strength. At a temperature above 1250 °C, liquid phase formation due to the presence of SiO_2 counterbalances the expansion and increases the creep strain rate; this helps to decrease the thermo-mechanical stresses. Due to the formation of a liquid phase, the creep resistance of the material decreases.

- The creep behaviour of the SF castable was investigated under uniaxial compressive loads. As expected, creep strain rates increase with temperature. Besides, the material inhomogeneities exhibited a higher impact on the second and third stages. Norton-Bailey creep parameters were successfully inversely evaluated for all three stages.

- The evaluation of the creep parameters from different combinations of measurements enabled to obtain statistical information about the creep parameters. The results obtained by considering the 99% confidence interval showed that the combination of six out of nine measurements provided the closest mean value to that of the combination of all measurements [113].

- Under l/u conditions, recovery ratios – but not the recovered strains - decreased with increasing holding time. Moreover, the recovery ratios increased with lower stress in the unloading period. It is concluded that during the creep of the castable internal stress was generated. Creep strain recovery is directly influenced by the difference between the internal stress and the load on the sample. Additionally, it was observed that the internal stress in each cycle depends on creep strain and the residual internal stress from the previous cycle. If the internal stress is not completely consumed for strain recovery in one cycle, the residual adds to the internal stress of the following cycle [125].

- A four-element Burger's model was employed to model the creep and recovery of the SF castable under l/u conditions. In order to simulate the creep recovery behaviour in ABAQUS, the Prony series were determined using an inverse evaluation with DAKOTA. Results indicated that The Prony parameters determined by DAKOTA showed a reasonable fit as the parameters of the Burger model. However, using these parameters gave a satisfactory fit only for the first cycle of each test. However, fitting several experimental curves with different loading histories was impossible.

- A Non-linear kinematic hardening model (Chaboche) was applied for FE-simulation. This model enabled the fitting of different l/u experimental curves at the same temperature with one series of parameters. Some deviations between the experimental and simulated curves were observed for the 7 MPa tests. It is assumed that an important cause is the heterogeneity of the material. The Chaboche model showed a good agreement with the measurements; however, a large number of the parameters and the determination is a disadvantage. In further investigations, the Chaboche model was used to fit the first stage of experimental creep curves under different loads and temperatures. Results proved that the model can fit the Norton-Bailey model if the correct parameters for each temperature were identified. Therefore, the Chaboche model can be a comprehensive model for simulating the creep under monotonic and l/u conditions.

The findings show the importance of correctly representing load history for thermomechanical lining simulations. This puts the focus on further research on suitable material models associated with procedures for testing and parameter determination.

7 OUTLOOK

Extensive testing of different materials at different loads and temperatures is required to provide an overview of how the strain recovery affects the service behaviour. A Chaboche model was used to fit the first stage of the creep tests under different constant loads. It is assumed that this model can represent an acceptable fit for the second stage. Modification and development of this model might be a future research item.

Compressive creep of refractories has been commonly investigated; however, in many industrial applications, refractories are facing complex loading conditions including multiaxial stress states. Creep rates differ significantly in dependence of the stress state.

Due to the heterogeneous nature of the refractories, it is essential to carry out a statistical study on the Norton-Bailey creep parameters for all three stages. These results might be helpful for other mechanical characterization of refractory castables and are necessary for future creep investigations.

8 REFERENCES

[1]   C. Schacht, "Refractories Handbook", CRC Press, (2004).

[2]   DIN EN 1402-1, Unshaped refractory products - Part 1: Introduction and classification, (2004).

[3]   M. Schnabel, A. Buhr, R. Exenberger, and C. Rampitsch, "Spinel: In situ versus Preformed-Clearing the Myth" Refractories, Worldforum 2 (2010).

[4]   T. A. Bier, C. Parr, C. Revais, M. Vialle, and L. Aluminates, "Spinel forming castables: Physical and chemical mechanisms during drying", Refractory application November 2000, pp. 3-4.

[5]   A. P. D. Luz, M. A. L. Braulio, V. C. Pandolfelli, "Refractory Castable Engineering," (2015).

[6]   M. A. L. Braulio, M. Rigaud, A. Buhr, C. Parr, and V. C. Pandolfelli, "Spinel-containing alumina-based refractory castables," Ceramics International, vol. 37, no. 6, pp. 1705-1724, (2011). doi: 10.1016/j.ceramint.2011.03.049.

[7]   B. Nagi, O. Matsumoto, T. Isobe, Y. Nishiumi, "Wear mechanism of castable for steel ladle by slag", Taikabutsu Overseas, 12(1992), pp.15-20.

[8]   G.W. Kriechbaum, V Gnauck, G. Routschka, "The Influence of SiO_2 and Spinel on the Hot Properties of High-Alumina Low-Cement Castables". 37th International Colloquium on Refractories, Aachen (1994).

[9]   E. Y. Sako, M. A. L. Braulio, P. O. Brant, and V. C. Pandolfelli, "The impact of pre-formed and in situ spinel formation on the physical properties of cement-bonded high alumina refractory castables," Ceramics International, vol. 36, no. 7, pp. 2079-2085, Sep. 2010, doi: 10.1016/j.ceramint.2010.04.005.

[10]   E. Y. Sako, M. A. L. Braulio, D. H. Milanez, P. O. Brant, and V. C. Pandolfelli, "Microsilica role in the CA_6 formation in cement-bonded spinel refractory castables," Journal of Materials Processing Technology, vol. 209, no. 15–16, pp. 5552-5557, Aug. 2009, doi: 10.1016/j.jmatprotec.2009.05.013.

[11]   M.A.L. Braulio, D.H. Milanez, E.Y. Sako, L.R.M. Bittencourt, V.C. Pandolfelli, "Expansion behavior of cement-bonded alumina–magnesia refractory castables", Journal of American Ceramic Society Bulletin 86 (12) (2007), pp.9201-9209.

[12]   F. Simonin, C. Olagnon, S. Maximilien, G. Fantozzi, "Thermomechanical behaviour of high alumina refractory castables with synthetic spinel addition", Journal of American Ceramic Society 83 (2000), pp. 2481-2490.

[13]   E. Y. Sako, M. A. L. Braulio, E. Zinngrebe, S. R. van der Laan, and V. C. Pandolfelli, "In-depth microstructural evolution analyses of cement-bonded spinel refractory castables: Novel insights regarding spinel and CA_6 formation," Journal of the American Ceramic Society, vol. 95, no. 5, pp. 1732-1740, May 2012, doi: 10.1111/j.1551-2916.2012.05161.

[14]   KG. Ahari, WE. Lee, S. Habesch. "Spinel formation in cement-free castable bond system". Proc. 44th Intl. Coll. On Refractories, Refractories in steelmaking, Aachen. Germany, (2001): pp.160-163.

REFERENCES

[15]   M. Fuhrer, A. Hey, and W. E. Lee, "Microstructural Evolution in Self-forming Spinel/Calcium Aluminate-Bonded Castable Refractories," Journal of the European Ceramic Society, Vol. 18, (1998), pp. 813-820.

[16]   M. A. L. Braulio, G. Morbioli, D. H. Milanez, and V. C. Pandolfelli, "Calcium aluminate cement source evaluation for Al_2O_3-MgO refractory castables," Ceramics International, vol. 37, no. 1, pp. 215–221, Jan. 2011, doi: 10.1016/j.ceramint.2010.09.027.

[17]   M. A. L. Braulio, P. O. C. Brant, L. R. M. Bittencourt, and V. C. Pandolfelli, "Microsilica or MgO grain size: Which one mostly affects the in situ spinel refractory castable expansion," Ceramics International, vol. 35, no. 8, pp. 3327-3334, Dec. 2009, doi: 10.1016/j.ceramint.2009.05.031.

[18]   M. A. L. Braulio, L. R. M. Bittencourt, J. Poirier, V. C. Pandolfelli, "Microsilica effects on cement bonded alumina-magnesia refractory castables. " Journal of the Technical Association of Refractories, Japan, 28, pp. 180-184, (2008).

[19]   M. A. L. Braulio, D. H. Milanez, E. Y. Sako, L. R. M. Bittencourt and V. C. Pandolfelli, "The Effect of Calcium Aluminate Cement on the in Situ Spinel Expansion", UNITECR 07, Proceedings, (2007), pp. 540-543.

[20]   J. M. Auvray, C. Gault, and M. Huger, "Evolution of elastic properties and microstructural changes versus temperature in bonding phases of alumina and alumina-magnesia refractory castables," Journal of the European Ceramic Society, vol. 27, no. 12, pp. 3489–3496, 2007, doi: 10.1016/j.jeurceramsoc.2007.01.016.

[21]   B. Nagai, O. Matsumoto, T. Isobe, "Development of high-alumina castable for steel ladles (findings on spinel formation in alumina-magnesite castable)". Taik. overs. (1990), Vol. 10(1), pp. 23-28.

[22]   P. Nandi, A. Grag, BD, Chattoraj. "Effect of Silica and Temperature on Spinel-Based High-Alumina Castables". American Ceramic Society Bulletin 31, (2000): pp. 65-69.

[23]   M. Tawara, K. Fuji, T. Taniguchi, M. Hagiwara, T. Kibayashi, M. Tanaka, "Application of alumina-magnesia castable in high temperature steel ladles", Taik. Overs. Vol.16 (2), (1996), pp. 17–19.

[24]   A. Banerjee, S. Das, S. Misra, S. Mukhopadhyay, "Structural analysis on spinel ($MgAl_2O_4$) for application in spinel-bonded castables", Ceramics International 35 (1), (2009), pp. 381–390.

[25]   H. Sarpoolaky, K. G. Ahari, and W. E. Lee, "Influence of in situ phase formation on microstructural evolution and properties of castable refractories." Ceramics International, V.28, (2002), pp. 487-493, https://doi.org/10.1016/S0272-8842(01)00121-3

[26]   A. Buhr, B. Baier, J. M. Aroni, R. W. McConnell, "Raw Material Concepts for SiO_2 free High Strength Castables in the Temperature Range up to 1200 °C", Conference of Metallurgists (2004) Hamilton, Ontario, Canada, pp. 151-157.

[27]   M. Nanba, T. Kaneshige, Y. Hamazaki, H. Nishio, I. Ebisawa. "Thermal characteristics of castable for teeming ladle"; Taik. Overs, Vol. 16. (1996), pp. 129-134.

[28]   J. Pelleg. "Mechanical properties of ceramics", Vol. 213, (2014).

[29]   J. Rösler, H. Harders and M. Bäcker, "Mechanical behaviour of engineering materials", (2007).

[30]   S. Jonsson, "Mechanical Properties of Metals and Dislocation Theory from an Engineer´s Perspective". Royal Institute of Technology, Material Science and Engineering, (2008).

[31]   V. Lee Burdick, "Compressive creep of high alumina refractories," Master's thesis 5162, (1967).

[32]   WR. Cannon, "Langdon TG. Creep of ceramics, part 1: mechanical characteristics", Journal of Materials Science, (1983); 18, pp.1-50.

[33]   C. Herring, "Diffusional viscosity of a polycrystalline solid". Journal of Applied Physics, (1950); 21, pp. 437-445.

[34]   RL. Coble, "Model for boundary diffusion-controlled creep in polycrystalline materials". Journal of Applied Physics, (1963); 34, pp.1679-1682.

[35]   TG. Langdon, "Grain boundary sliding as a deformation mechanism during creep". Philosophical Magazine, (1970); 22(178), pp. 689-700.

[36]   J. Weertman," Steady-state creep of crystals", Journal of Applied Physics, (1957); 28, pp. 1185-1187.

[37]   VS. Bakunov, "High-temperature creep of refractory ceramics: kinetics and the effect of experimental conditions". Refractories, (1994); 35(6), pp. 177-183,

[38]   DS. Wilkinson. "Creep mechanisms in multiphase ceramic materials". Journal of the American Ceramic Society. (1998) Feb;81(2), pp. 275-99.

[39]   A. Hynes, R. Doremus, "Theories of Creep in Ceramics". Critical Reviews in Solid State and Materials Sciences, (1996), 21:2, 129-187, DOI: 10.1080/10408439608241255.

[40]   G.D. Kim, "Creep of refractory concretes.", Retrospective Theses and Dissertations. 7773, (1984).

[41]   VS. Bakunov, "High temperature creep of refractory ceramics", Refractories, (1994); 35(11), pp. 353-359, https://doi.org/10.1007/BF02227223

[42]   JF. Clements, J. Vyse, "Creep measurements on some high alumina refractories", Transactions and Journal of the British Ceramic Society, (1966); 65, pp. 59-65.

[43]   VL. Burdick, DE. Day, "Creep of high-alumina refractories", Ceramic Bulletin, (1969); 48(12), pp. 1109-1113.

[44]   CO. Hulse, JA. Pask, "Analysis of deformation of a fireclay refractory". Journal of the American Ceramic Society, (1966); 49(6), pp. 312-318.

[45]   DJ. Bray, JR. Smyth TD, McGee, "Creep of 90% Al_2O_3 refractory concrete". Ceramic Bulletin, (1980); 59(7), pp. 706-710

[46]   DJ. Bray, JR. Smyth, TD. McGee, G. Kim, "Effect of cement content on the creep of a 90% Al_2O_3 refractory concrete". Ceramic Bulletin, (1984); 63(2), pp. 287-289.

REFERENCES

[47] DJ. Bray, JR. Smyth, TD. McGee, "Thermal/strain history effects on creep of refractory concrete". Journal of the American Ceramic Society, (1982); 65(6), pp. 275-79.

[48] LA. Diaz, R. Torrecillas, "Phase development and high temperature deformation in high alumina refractory castables with dolomite additions". Journal of the European Ceramic Society, (2007); 27, pp. 67-72.

[49] LA. Diaz, R. Torrecillas, "Hot bending strength and creep behaviour at 1000- 1400°C of high alumina refractory castables with spinel, periclase and dolomite additions". Journal of the European Ceramic Society, (2009); 29, pp. 53-58.

[50] JT. Boyle, J. Spence, "Stress analysis for creep". Camelot Press, London, (1983).

[51] R.K. Penny, D.L. Marriott, "Design for creep". Chapman & Hall, London, UK, (1995).

[52] WN. Findley, JS. Lai, K. Onaran, "Creep and relaxation of nonlinear viscoelastic materials". Vol. 18, (1976), Dover Publications, INC., New York.

[53] H. Yao, F. Xuan, Z. Wang, S. Tu. "A review of creep analysis and design under multi-axial stress states". Nuclear Engineering and Design, (2007); 237, pp. 1969- 1986.

[54] FH. Norton. "The creep of steel at high temperatures", McGraw-Hill, London, (1929).

[55] RW. Bailey, "The utilization of creep test data in engineering design". Proceedings of the Institution of Mechanical Engineers, (1935); 131, pp. 131-149.

[56] JE. Dorn, "Some fundamental experiments on high temperature creep". Journal of the Mechanics and Physics of Solids, (1955); 3(2), pp. 85-116.

[57] I. Matsumura, Y. Hazashi, Y. Hiyama, A. Ijiri, "Refractoriness under load and hot creep measurements", Taik. Overs. (1990); 2(2), pp. 36-42.

[58] EN 993-9, "Methods of test for dense shaped refractory products". Determination of creep in compression, (1973).

[59] Y. Chien, T. Lee, H. Pan, Y. Ko, "Effect of Cr_2O_3 on creep resistance of high alumina bauxite refractories". American Ceramic Society Bulletin, (1984); 63(7), pp. 915-918.

[60] USh. Shayakhmetov, VS. Bakunov, IM. Valeev, VR. Bikbulatov, "Measuring the high-temperature strain and creep in nonfired refractories", Refractories and Industrial Ceramics, 2006; 47(2): 128-131.

[61] JG. Hemrick, AA. Wereszczak, "Non-classical creep behaviour of Fusion-Cast alumina refractories". Refractories Applications Transactions, (2009); 4(1), pp 2- 8.

[62] S. Jin, D. Gruber, H. Harmuth, and R. Rössler, "Thermomechanical failure modelling and investigation into lining optimization for a Ruhrstahl Heraeus snorkel," Engineering Failure Analysis, vol. 62, pp. 254–262, (2016), doi: 10.1016/j.engfailanal.2016.01.014.

[63] S. Jin, "Investigation of compressive refractory creep", Doctoral thesis at the chair of ceramics, (2015).

REFERENCES

[64] S. Jin, H. Harmuth, and D. Gruber, "Compressive creep testing of refractories at elevated loads-Device, material law and evaluation techniques," Journal of the European Ceramic Society, vol. 34, no. 15, pp. 4037–4042, (2014), doi: 10.1016/j.jeurceramsoc.2014.05.034.

[65] S. Schachner, S. Jin, D. Gruber, and H. Harmuth, "A method to characterize asymmetrical three-stage creep of ordinary refractory ceramics and its application for numerical modelling," Journal of the European Ceramic Society, vol. 39, no. 14, pp. 4384–4393, Nov. 2019, doi: 10.1016/j.jeurceramsoc.2019.06.010.

[66] F. D. Javanroodi and K. M. Nikbin, "The fracture mechanics concept of creep and creep/fatigue crack growth in life assessment", IUST International Journal of Engineering Science 17 (3-4), pp.1-7, (2006).

[67] G. Roebben, B. Bollen, A. Brebels, J. Van Humbeeck, O. Van der Biest, "Impulse excitation apparatus to measure resonant frequencies, elastic moduli, and internal friction at room and high temperature". Reviews of Scientific Instruments, (1997); 68(12), pp. 4511-4515.

[68] D.W. Marquardt, "An algorithm for least-squares estimation of nonlinear parameters", Journal of the Society for Industrial and Applied Mathematics. Vol. 11 (1963), pp. 431-441, https://doi.org/10.1137/0111030

[69] Matlab Release 2019a; The Math Works, Inc., Natick, Massachusetts, United States, (2019).

[70] S. Schachner, S. Jin, D. Gruber, and H. Harmuth, "Three stage creep behavior of MgO containing ordinary refractories in tension and compression," Ceramics International, vol. 45, no. 7, pp. 9483–9490, May 2019, doi: 10.1016/j.ceramint.2018.09.124.

[71] S. Schachner, "Creep behaviour of refractories under various loading conditions", Doctoral thesis at the chair of ceramics, (2020).

[72] X. Wu and J. W. Holmes, "Tensile Creep and Creep-Strain Recovery Behavior of Silicon Carbide Fiber/Calcium Aluminosilicate Matrix Ceramic Composites.", Journal of American Ceramic Society, 76, pp. 2695-700, (1993).

[73] J. W. Holmes, Y. H. Park, and J. W. Jonesc, "Tensile Creep and Creep-Recovery Behavior of SiC-Fiber-Si3N4-Matrix Composite", Journal of American Ceramic Society, 76, pp. 1281-92, (1993).

[74] Z.Y. Deng, J.L. Shi, Y.F. Zhang, T.R. Lai, and J.K. Guo, "Creep and Creep-Recovery Behavior in Silicon-Carbide-Particle-Reinforced Alumina." Journal of American Ceramic Society, 82, pp. 944-52, (1999).

[75] E. Norman Dowling, "Mechanical Behaviour of Material, Engineering Methods for Deformation", Fracture, and Fatigue (2013), pp. 20-28, 190, 841.

[76] Y. L. Yang, Z. Shi, Y. Li, Q. Rong, and R. Said, "Experimental studies and constitutive modelling of anelastic creep recovery during creep age forming", in Procedia Engineering, (2017), vol. 207, pp. 275–280. doi: 10.1016/j.proeng.2017.10.774.

[77] W. H. Li, H. Du, G. Chen, and S. H. Yeo, "Experimental investigation of creep and recovery behaviors of magnetorheological fluids", Materials Science and Engineering Vol. A333, (2002), pp. 368-376.

[78]   R. Furushima, Y. Matsuo, T. Shiota, and K. Yasuda, "Damage evaluation of refractories under cyclic loading-unloading processes using ultrasonic method," Journal of Materials Science, vol. 42, no. 20, pp. 8652–8661, (2007), doi: 10.1007/s10853-007-1828-y.

[79]   Z. L. Zhan and J. Tong, "A study of cyclic plasticity and viscoplasticity in a new nickel-based superalloy using unified constitutive equations. Part II: Simulation of cyclic stress relaxation," Mechanics of Materials, vol. 39, no. 1, pp. 73–80, (2007), doi: 10.1016/j.mechmat.2006.01.006.

[80]   A. al Mamun, R. J. Moat, and P. J. Bouchard, "Origin and effect of back stress on cyclic creep deformation of 316h stainless steel", Proceedings of the ASME (2015) Pressure Vessels and Piping Conference PVP2015.

[81]   J. K. Mahato, P. S. De, A. Sarkar, A. Kundu, and P. C. Chakraborti, "Effect of prestrain and stress rate on bauschinger effect of monotonically and cyclically deformed OFHC copper," in Procedia Engineering, (2014), vol. 74, pp. 368–375. doi: 10.1016/j.proeng.2014.06.281.

[82]   C. Gaudin and X. Feaugas, "Cyclic creep process in AISI 316L stainless steel in terms of dislocation patterns and internal stresses," Acta Materialia, vol. 52, no. 10, pp. 3097–3110, (2004), doi: 10.1016/j.actamat.2004.03.011.

[83]   Z. L. Zhan and J. Tong, "A study of cyclic plasticity and viscoplasticity in a new nickel-based superalloy using unified constitutive equations. Part I: Evaluation and determination of material parameters," Mechanics of Materials, vol. 39, no. 1, pp. 64-72, (2007), doi: 10.1016/j.mechmat.2006.01.005.

[84]   K. Jakus, S. Nair. "High temperature mechanical behaviour of ceramic composites"; (1995), pp. 193-260.

[85]   M. Yang, Y. Pan, F. Yuan, Y. Zhu, and X. Wu, "Back stress strengthening and strain hardening in gradient structure," Materials Research Letters, vol. 4, no. 3, pp. 145–151, Mar. 2016, doi: 10.1080/21663831.2016.1153004.

[86]   J. Lemaitre, J-L Chaboche, "Mechanics of solid materials", Cambridge University Press (1990), Chapter 6.

[87]   C. Norman Ahlquist, W. D. Nix, "A technique for measuring mean internal stress during high temperature creep". Scripta Metallurgica 3, 679 (1969).

[88]   H. Sehitoglu, "Changes in state variables at elevated temperatures", Journal of Engineering Materials and Technology 111, 192 (1989).

[89]   R. W. Neu, D. T. Scott, M. W. Woodmansee, "Measurement and modelling of back stress at intermediate to high homologous temperatures", International Journal of Plasticity 16 (2000) 283-301.

[90]   F. Bai, Xi. Yang, G. Zeng, "Creep and recovery behavior characterization of asphalt mixture in compression," Construction and Building Materials, 54 (2014) 504-511.

[91]   L. F.G. Setz, A. C. Silva, S.C. Santos, S. R.H. Mello-Castanho, M. R. Morelli, "A viscoelastic approach from α-Al_2O_3 suspension with high solids content," Journal of the European Ceramic Society, 33 (2013), pp. 3211-3219.

[92]   A. Fazal, K. Fancey, "Viscoelastically generated prestress from ultra-high molecular weight polyethylene fibres," Journal of Material Science (2013) 48, pp. 5559-5570.

[93]   JL. Chaboche, D. Nouailhas, "A unified constitutive model for cyclic viscoplasticity and its applications to various stainless steels", Journal of Engineering Materials and Technology, Vol. 111, (1989).

[94]   T. G. Mezger, "The Rheology Handbook ": 4th Edition. Vincentz Network, (2014).

[95]   GC. Papanicolaou, SP. Zaoutsos, "Viscoelastic constitutive modelling of creep and stress relaxation in polymers and polymer matrix composites". Creep and fatigue in polymer matrix composites (2011), pp. 3-47, https://doi.org/10.1533/9780857090430.1.3.

[96]   R. Zaouali, S. Msahli, and S. Faouzi, "A Nonlinear Viscoelastic Model for Describing Fabric Wrinkle Recovery Behavior", International journal of Applied Research on Textile," (2014), Vol. 2, pp. 22-32.

[97]   Y. Liu and Z. You, "Determining burger's model parameters of asphalt materials using creep-recovery testing data," in Proceedings of the Symposium on Pavement Mechanics and Materials at the Inaugural International Conference of the Engineering Mechanics Institute - Pavements and Materials (2008), vol. 334, pp. 26–36. doi: 10.1061/41008(334)3.

[98]   X. Zhang, X. Gu, J. Lv, Z. Zhu, X. Zou, "Numerical analysis of rheological behaviors of basalt fiber reinforced asphalt mortar using ABAQUS," Construction and Building Materials 157 (2017), pp. 392-401.

[99]   M. Bharadwaj, S. Claramunt, and S. Srinivasan, "Modeling Creep Relaxation of Polytetrafluorethylene Gaskets for Finite Element Analysis," International Journal of Materials, Mechanics and Manufacturing, vol. 5, no. 2, pp. 123–126, (2017), doi: 10.18178/ijmmm.2017.5.2.302.

[100]   P. Mackiewicz and A. Szydło, "Viscoelastic parameters of asphalt mixtures identified in static and dynamic tests," Materials, vol. 12, no. 13, (2019), doi: 10.3390/ma12132084.

[101]   W. R. Broughton, "Creep testing of adhesive joints analysis of creep rupture data", Technical Report No. 14, (1999).

[102]   F. Zhi-Jun, Z. Jia-Ming, and H.-S. Yuan, "A Constitutive Model for Mudstone Shear Creep." EJGE, Vol. 19, (2014), pp. 259- 271.

[103]   M. I. Faraz, N. A. M. Besseling, A. v. Korobko, and S. J. Picken, "Characterization and modelling of the creep behavior of a thermoset nanocomposite," Polymer Composites, vol. 36, no. 2, pp. 322–329, (2015), doi: 10.1002/pc.22946.

[104]   JL. Chaboche, "Constitutive equations for cyclic plasticity and cyclic viscoplasticity". International journal of plasticity, (1989) 1;5, pp. 247-302.

[105]   JL. Chaboche, "Time-independent constitutive theories for cyclic plasticity". International Journal of Plasticity, (1986) 1;2, pp. 149-88.

[106]   JL. Chaboche, "A review of some plasticity and viscoplasticity constitutive theories," International Journal of Plasticity, vol. 24, no. 10, pp. 1642–1693, (2008), doi: 10.1016/j.ijplas.2008.03.009.

[107] J. Tong, Z. L. Zhan, and B. Vermeulen, "Modelling of cyclic plasticity and viscoplasticity of a nickel-based alloy using Chaboche constitutive equations," International Journal of Fatigue, vol. 26, no. 8, pp. 829–837, (2004), doi: 10.1016/j.ijfatigue.2004.01.002.

[108] M. C. Araujo, "Non-linear kinematic hardening model for multiaxial cyclic plasticity" (2002). LSU Master's Theses. 1650.

[109] Dassault systems, ABAQUS (2018) 'ABAQUS Documentation' (2018).

[110] U. Sarajärvi, O. Cronvall," A procedure to generate input data of cyclic softening and hardening for FEM analysis from constant strain amplitude fatigue tests in LCF regime", IASBN 978/87/7892/213/3, NKS-150, (2007).

[111] Writing User Subroutine with ABAQUS, Lecture 6, (2019).

[112] M. Krobath, R. Krobath, Ch. Bernhard, W. Ecker, "Elasto-viscoplastic material model of a directly-cast low-carbon steel at high temperatures" Materials (2020), 13, 2281; doi:10.3390/ma13102281.

[113] B. Akbari, D. Gruber, S. Jin, and H. Harmuth, "Investigation of three-stage compressive creep of a spinel forming refractory castable containing 8% MgO," Ceramics International, vol. 48, no. 3, pp. 3287–3292, (2022), doi: 10.1016/j.ceramint.2021.10.103

[114] EN ISO 1927-6:2012 - "Monolithic (unshaped) refractory products - Part 6: Measurement of physical properties.

[115] A. Buhr, "Refractories for Steel Secondary Metallurgy", CN-Refractories, Vol. 6, (1994).

[116] Y.C. Ko and J. T. Lay, "Thermal Expansion Characteristics of Alumina-Magnesia and Alumina-Spinel Castables in the Temperature Range 800°-1650°C." Journal of American Ceramic Society, 83 (2000), pp. 2872-74.

[117] N. Kazemi, "Reasons for crack propagation and strength loss in refractory castables based on changes in their chemical compositions and micromorphologies with heating: special focus on the large blocks," Journal of Asian Ceramic Societies, vol. 7, no. 2. Taylor and Francis Ltd., pp. 109–126, Apr. 03, 2019. doi: 10.1080/21870764.2019.1597957.

[118] CH. Chen-Feng and KO. Yung-Chao, "Effect of CaO Content on the Hot Strength of Alumina–Spinel Castables in the Temperature Range of 1000° to 1500°C", Journal of American Ceramic Society, 81 (1998) 2957–2960.

[119] Y. C. Ko and C. F. Chan, "Effect of Spinel Content on Hot Strength of Alumina-spinel Castables in the Temperature Range 1000±1500°C", Journal of the European Ceramic Society 19 (1999).

[120] W. Węglewski, K. Bochenek, M. Basista, T. Schubert, U. Jehring, J.Litniewski, S. Mackiewicz, "Comparative assessment of Young's modulus measurements of metal-ceramic composites using mechanical and non destructive tests and micro-CT based computational modelling", Computational Materials Science. 77 (2013), pp.19–30. https://doi.org/10.1016/j.commatsci.2013.04.007.

[121] ASTM C1259- 08, "Standard test method for Dynamic Young's modulus, Shear modulus, and Poisson's ratio for advanced ceramics by impulse excitation of vibration" (2008).

[122] E. Nonnet, N. Lequeux, and P. Boch, "Elastic Properties of High Alumina Cement Castables from Room Temperature to 1600 C." Journal of European Ceramic Society, Vol. 19, (1999), pp. 1575-1583.

[123] S. Samadi, S. Jin, D. Gruber, H. Harmuth, and S. Schachner, "Statistical study of compressive creep parameters of an alumina spinel refractory," Ceramics International, vol. 46, no. 10, pp. 14662–14668, (2020), doi: 10.1016/j.ceramint.2020.02.267.

[124] D.C. Montgomery, "Design and analysis of experiments", John wiley & sons, (2017).

[125] B. Akbari, D. Gruber, S. Jin, and H. Harmuth, "Creep strain recover of an in-situ spinel-forming refractory castable under loading/unloading compressive creep condition," Ceramics International, vol. 49, Issue 15, pp. 25225–25231, (2023), https://doi.org/10.1016/j.ceramint.2023.05.055.

[126] DAKOTA, User's Manual, Version 5.2, unlimited release, (2011).

9 LIST OF FIGURES

10   LIST OF TABLES